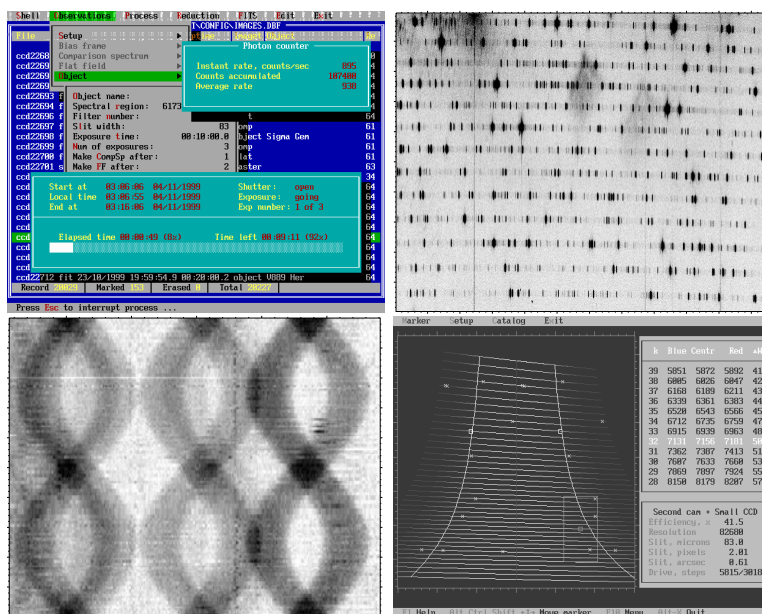


High resolution SOFIN CCD échelle spectroscopy

Ilya V. Ilyin



Oulu 2000

Astronomy Division
Department of Physical Sciences
University of Oulu
Finland

High resolution SOFIN CCD échelle spectroscopy

Ilya V. Ilyin

ACADEMIC DISSERTATION

To be presented, with the permission of the Faculty of Science of the University of Oulu, for public criticism in the Auditorium GO101 on September 1st, 2000, at 12 o'clock noon.

The figures on the front page are:

The console screen of the observation menu of 4A at the top left. A ThAr comparison SOFIN échelle spectrum image in the 5030 & 4924 spectral region at the top right. The selection of the spectral settings with the focal plane map of the SOFIN spectrograph at the bottom right. The phased image of spectral lines around 6430Å of the detached RS CVn binary ER Vul.

ISBN 951-42-5724-3
Oulu 2000
University Press

Preface

This work concerns observations with the SOFIN spectrograph and the data reduction of échelle spectra. The work began in 1991 when the spectrograph was for the first time installed at the Nordic Optical Telescope. In that period, the author was involved in developing the control software for the spectrograph and the CCDs, so that now the observations are almost completely remotely controlled by computer. Later, the development of the data reduction package has started which was motivated by the absence of other suitable software packages at that time, and, also, by the specific requirements to the data reduction of the SOFIN spectra. The aim of the thesis is the development of observing techniques and of optimal reduction methods, and their implementation. The use of these methods in the observation and reduction has resulted in a large number of high-quality and, in some respect, unique, échelle spectra within different astrophysical programmes and in many scientific papers. A selection from these has formed the astrophysical results of the thesis. Thus, the thesis merges three different aspects of scientific work: the instrument, the data reduction including error analysis, and the application to various astrophysical targets.

The thesis work has the following structure.

Chapter 1 gives the description of the spectrograph and scientific objectives of the observing programmes. Then, the estimation and measurement of the efficiency of the spectrograph follows. In the next sections, the model of the spectrograph is described, which is incorporated in a software tool used during observations for the proper settings of the instrument. In the last section, the stability issues of the spectrograph are discussed based upon a number of tests.

In Chapter 2, the measurements of the spectrograph instrumental profile is given which is followed by the discussion of several important issues concerning the resolving power of the instrument.

Chapter 3 concerns the CCDs. This part was specially developed to solve the initial problems and improve the performance of the SOFIN Astromed-CCD cameras. The following aspects are illustrated: the noise sources, the flat-fielding problem, and the measurable characteristics of the CCD performance. The measurement

and integration of the CCD intensity transfer function is given. In the following sections, the method of the CCD optimization is highlighted.

In Chapter 4, an overview of the data reduction package is given. The limitations on the volume of this thesis do not allow to give the whole description of all the specific algorithms developed for the data reduction. As an example, the cross-correlation method and its accuracy are discussed because it is essential for the accurate radial velocity measurements of the stellar spectra, which is demonstrated in the first papers of the thesis.

Deconvolution of stellar spectra and recovery of broadening functions are an important issue in modern methods of data analysis. A number of astrophysical aspects, the model, and the implementation of the algorithm are given in Chapter 5. The method used is based on the truncated generalized least-squares and operates with the principal components of the solution. The limitations of the method are discussed motivating the regularized principal solution extension. An example of the deconvolution of the SOFIN solar spectrum is given and discussed in brief.

The most recent, not yet published aspect of the author's work is given in Chapter 6 and concerns the mercury line profile variability of the binary star α And. The description of the analysis is given and some results are discussed.

In the Appendix, a user's guide for the reduction of SOFIN échelle spectra is given, which illustrates various aspects of the process and effects which are taken into account to achieve the maximal photometric and position quality of the spectra.

The second part of the thesis consists of selected papers based on SOFIN observations where the author's work was essential. In the preface to the second part, a short description of the author's contributions is given which is followed by the list of all papers where the author was involved.

A part of the author's dissertation work which is not included into the present thesis because of its size concerns the numerical methods of data analysis. In a separate manuscript, the following topics are described: propagation of random errors; the generalized least-squares: the linear, non-linear, and constrained cases; test of the linear hypothesis; the orthogonal polynomial series and their transformations to power series and Chebyshev forms; the smoothing splines; and the solution to the Keplerian orbit problem and the binary system parameters. These ready-to-program algorithms were derived by the author on the basis of a number of treatises on numerical analysis and implemented into the data reduction package. The most important aspect of these derivations is the proper error analysis of the parameters and the model, which plays a key role in the reduction process of the spectra where the intensities and their errors are transformed at each stage (including at some stages the wavelength errors). The description of the deconvolution of stellar spectra (Chapter 5) is a part of this handbook and uses the same style and notations.

Acknowledgements

This work was carried out as a part of the scientific project “Late type stars and interstellar matter: activity, magnetism, and turbulence” led by Prof. I.Tuominen and funded by the Academy of Finland. The work has begun in the Observatory of the University of Helsinki in 1991, and was then continued at the University of Oulu in 1996.

I express my gratitude, firstly, to Prof. I.Tuominen for giving me the possibility to join his project and for his long term support in many aspects of various kinds.

I thank very much the pre-referees of my dissertation for their careful reading, their kind suggestions for the further improvement of the text, and for the evaluation of the work in their statements. The manuscript was examined by Dr. Jaan Pelt, Tartu Observatory, Estonia, and Prof. Gösta Gahm, Stockholm Observatory, Sweden.

I want to thank Prof. Craig Mackay (Institute of Astronomy, Cambridge, England) for his stimulating discussions concerning the CCDs; the engineers at ORM, La Palma, Chris MacCovach (ING), Thomas Erm and Graham Cox (NOT), for their kind assistance to me with the CCD work, and Dr. Slavek Rucinski (Toronto, Canada) for the discussions which have stimulated my work on deconvolution of spectra.

Many thanks to my collaborators and co-workers Svetlana Berdyugina, Peter Petrov, and Nikolai Piskunov. My special thanks to Rudolf Duemmler for his close participation in many parts of my work in terms of critical assessments, detailed discussions, and for his essential help to improve the style of the manuscript.

At last, I sincerely thank my family Svetlana, Ellen, and Julia (and our dog Timon) for their invaluable support, patience and understanding.

Contents

1	The échelle spectrograph SOFIN	11
1.1	Introduction	11
1.2	Scientific applications	12
1.3	Design of the spectrograph	13
1.4	Efficiency of the spectrograph	19
1.4.1	The direct measurement of the efficiency	21
1.4.2	The expected efficiency	25
1.5	Model of the spectrograph	25
1.5.1	Spectral mosaic	26
1.5.2	The échelle efficiency	28
1.5.3	The resolving power	29
1.5.4	The optimal slit width	30
1.5.5	The pointing model of the spectrograph	31
1.6	Stability of the spectrograph	32
1.6.1	Line broadening due to flexure	34
1.6.2	Statical stability of the spectrograph	39
2	The instrumental profile	43
2.1	The instrumental profile	43
2.1.1	Obtaining the instrumental profile	43
2.1.2	The measurement of the resolving power	46
2.1.3	The natural width of the HeNe laser 6328 Å line	47
2.1.4	The features	49

2.1.5	Comparison with the solar spectrum	52
2.1.6	The real resolving power	53
2.1.7	Discussion	56
3	Optimization of CCD performance	59
3.1	Introduction	59
3.2	Noise of the ideal CCD	59
3.3	Correction for the high frequency spatial noise	62
3.4	Charge transfer efficiency	64
3.5	The intensity transfer function of the CCD	65
3.5.1	The CCD gain function	67
3.5.2	Integration of the transfer equation	68
3.6	The mask method	70
4	Processing astronomical spectra	75
4.1	The 4A software package	75
4.2	Reduction of CCD échelle spectra: an overview	76
4.3	The cross-correlation offset determination	79
4.3.1	The cross-correlation method	79
4.3.2	The accuracy for Gaussian profiles	81
4.4	Rebinning into radial velocity scale	82
5	Deconvolution of stellar spectra	85
5.1	Introduction	85
5.2	Formulation of the problem	87
5.3	The sampling matrix	87
5.4	Deconvolution of the PSF	89
5.5	Deconvolution of the spectrum	90
5.6	The principal components regression	91
5.7	Selection of the principal components	95
5.7.1	The F -test	95
5.7.2	Goodness of the fit	96
5.7.3	Analysis of variance	96

5.8	The constrained principal components solution	97
5.9	Linear regularization methods	98
5.10	The standard formulation	98
5.11	Regularized principal components solution	100
5.11.1	Regularization of the principal components	102
5.11.2	Regularization of the original parameters	103
5.11.3	Regularization of the fitting function	103
5.12	Regularized differential solution	104
5.13	Astronomical example	106
6	Line profile variations of α And	111
6.1	Introduction	111
6.2	Observations and data reduction	111
6.3	Radial velocity measurements	112
6.4	The period of the line profile variations	113
6.5	Variability of other spectral lines	116
A	User's guide for the data reduction	121
A.1	Introduction	121
A.2	The essential steps of the data reduction	121
A.3	Removal of the CCD bias	122
A.4	Flat field correction	124
A.5	Scattered light removal	125
A.6	Definition of spectral orders	127
A.7	Optimal extraction of spectra	128
A.8	Correcting the shape of the spectra	129
A.9	Wavelength calibration	130
A.9.1	The wavelength solution of the comparison spectrum	132
A.9.2	The telluric wavelength solution	135
A.10	The wavelength transformations	138
A.11	Continuum normalization	141
A.12	Cross-correlation of spectra	143
A.13	Decomposition of line profiles	144

References	147
II Publications	151
B Publications based on SOFIN observations	153
B.1 T Tau stars	154
B.2 RS CVn stars	155
B.3 Other stars and topics	156
Paper I & II	158
Paper III	158
Paper IV	158
Paper V	158
Paper VI	159
Paper VII	159
Paper VIII	159
Paper IX	159
Paper X	159
Paper XI	159

Chapter 1

The échelle spectrograph SOFIN

1.1 Introduction

The high resolution échelle spectrograph SOFIN was designed and manufactured at the Crimean Astrophysical Observatory in collaboration with the Observatory of Helsinki University and installed at the Cassegrain focus of the 2.56 m Nordic Optical Telescope, La Palma, Canary Islands. The observations with the instrument started in June 1991 (Tuominen 1992). The spectrograph is a unique instrument in its class and is one of the few very high resolution spectrographs in the northern hemisphere. The spectrograph was designed to allow stellar spectroscopy with three different spectral resolutions $R = \lambda/\Delta\lambda = 30\,000$, $80\,000$, and $170\,000$, depending on the brightness of the star and the scientific goals. The resolution is altered by changing one of the three different optical cameras whilst all other optical elements of the spectrograph remain unchanged. The spectrograph is equipped with a cross-dispersion prism to separate spectral orders so that many different wavelengths are recorded in a single CCD exposure. The higher the spectral resolution the smaller the part of the spectral range which can be covered by the CCD. The change of the spectral setting is done by turning the échelle grating and the cross-dispersion prism.

The spectrograph is completely remotely controlled from the host computer, except for a few minor functions. Such a design provides a high operational efficiency during the observations. The spectrograph control software is currently running under MS-DOS and is a menu-driven program with a range of services to assist the observations (Ilyin 1996). It includes a database of observations where the data records are stored, which can be retrieved and displayed later, a quick-look facility

for an express analysis of the data obtained, the databases of observed objects and spectral regions to hold all information specific for the particular observation and the setup of the spectrograph. The data reduction facility is the second large part of the software developed for the spectrograph. The key points of the data reduction package are the simplicity and the high efficiency which in conjunction with the user-friendly interface provides an easy way to operate with the enormous amount and complex nature of the data.

1.2 Scientific applications

The long focus optical camera provides the highest spectral resolving power $R = 180\,000$ and is used to resolve the fine structures of spectral lines and for accurate measurements of their positions. For instance, the interstellar Na I D 5890 \AA is formed on the line of sight to some background stellar object and reflects the motions of interstellar clouds. The higher the resolution, the more components can be resolved, i.e. the smaller velocity differences between different clouds can be detected. Another astrophysical aspect is to use the high resolution camera to measure the isotopic shift and hyperfine structure of the spectral lines of chemically peculiar Ap stars and of cool stars (e.g. Wahlgren et al. 1999). In the case of the Ap stars, the isotopic ratio gives an estimate of the diffusion rate of the isotopes from the enriched regions of their origin to the upper atmosphere. The very important Li I 6707 \AA line is a key element for studying the history of the universe, nucleosynthesis, stellar interiors, and stellar evolution. These measurements require the accurate observation of the position and intensity of fully resolved spectral lines with the subsequent accurate analysis and comparison with a synthetic spectrum. The high resolution camera allows to increase the accuracy of radial velocity measurements, since the error of the spectral line position determination decreases as the resolution grows. This also gives the possibility to investigate the instability and variations of the radial velocities of F, G, and K-type stars, which in the past were supposed to be very stable and were used as radial velocity standards. For some stars, these variations, seen as tiny Doppler shifts of the spectral line positions, are thought to be due to a low mass companion, like a brown dwarf or a large Jupiter-like planet, perturbing the position of the main star along the line of sight, although the variations may be caused as well by non-radial pulsations of a single star. To decide which explanation is correct for a particular star, accurate observations at the highest resolution are needed, allowing to study the line profile shapes in detail.

The second optical camera provides half of the resolving power of the previous one and corresponds to about $80\,000$ near the échelle blaze angle. Reducing the resolution two times doubles the amount of light per resolution element, as well as allows for a doubling of the entrance slit width which reduces the light losses, and, therefore, fainter objects can be observed. The second optical camera is widely

used for Doppler imaging of late type stars. These exhibit small bumps in a spectral line which drifts over the profile as the star rotates. The solution of the inverse problem, using models of stellar atmospheres, yields the geometrical distribution of the spots and a temperature map of the stellar surface (e.g. Bergyugina 1998). The medium resolution optical camera is used for the direct measurements of the stellar magnetic field with the Stokesmeter installed in front of the spectrograph entrance slit. The Stokesmeter divides the stellar light into two beams with opposite circular polarization. In the presence of a stellar magnetic field the spectral lines in these two beams are shifted with respect to each other and the stronger the field, the larger the offset. Measurements of the Zeeman splitting of a number of spectral lines gives the effective magnetic field of the star as a function of its rotational phase. Solving the inverse problem, using models of stellar atmospheres and taking into account the effect of Zeeman splitting, gives the distribution of the magnetic field strength over the stellar surface. Another aspect of the second camera applications is the observations of the non-radial pulsations of Ap stars on the short time scale of their variability with simultaneous recording of many spectral features in one exposure. Lines of certain chemical elements exhibit small variations of their radial velocities which can be attributed to the surface inhomogeneities. On the other hand, the amplitude of the oscillations derived from broad band photometry strongly decays from the blue to the red which is attributed to the wavelength dependence of limb-darkening and the steepness of the temperature gradient with respect to the optical thickness.

The low resolution camera provides a spectral resolution around 30 000 which is typical for most other stellar spectrographs. Since there is virtually no light loss on the wide entrance slit and the spectral resolution is low, the camera is used for observations of objects as faint as 15^m with a 2.5 m telescope. The camera allows to record in one exposure half of the whole optical spectrum ranging from the blue spectral orders at 3500 Å to the red at 11000 Å. Such curious objects as T Tauri and FU Orionis stars (e.g. Petrov et al. 1999), chromospherically active late type binary systems, red dwarfs, and cataclysmic variables are observable with the camera with most of the hydrogen lines, ultraviolet Ca II H & K, the infrared Ca II triplet seen in the same échelle image which offers the possibility to analyze spectral lines originating in different layers of the star and the surrounding environment.

1.3 Design of the spectrograph

The optical design of the SOFIN spectrograph is similar to that of the échelle spectrograph for the CTIO 4m Blanco Telescope. The complete spectrograph design is described in four papers: the optics (Pronik 1995), the mechanics (Lagutin 1995), the electronics (Bukach & Zlotnikov 1995), and the software (Ilyin 1995, including results of the first observations).

The spectrograph is mounted on the Cassegrain rotating adapter of the alt-azimuth

Nordic Optical Telescope (NOT). The diameters of the main and secondary mirror of the telescope are 2560 and 510 mm. The effective focal length is 28160 mm, which makes the scale in the focal plane $137 \mu\text{m}/1''$.

The schematics of the optics is given in Fig. 1.1 and the layout of the main components are shown in Figs. 1.2 and 1.3. All components of the spectrograph are assembled in a rigid welded construction which has the dimension of $1800 \times 800 \times 800 \text{ mm}^3$; the total weight without the CCD dewars is 240 kg. The components of the spectrograph are described in the following.

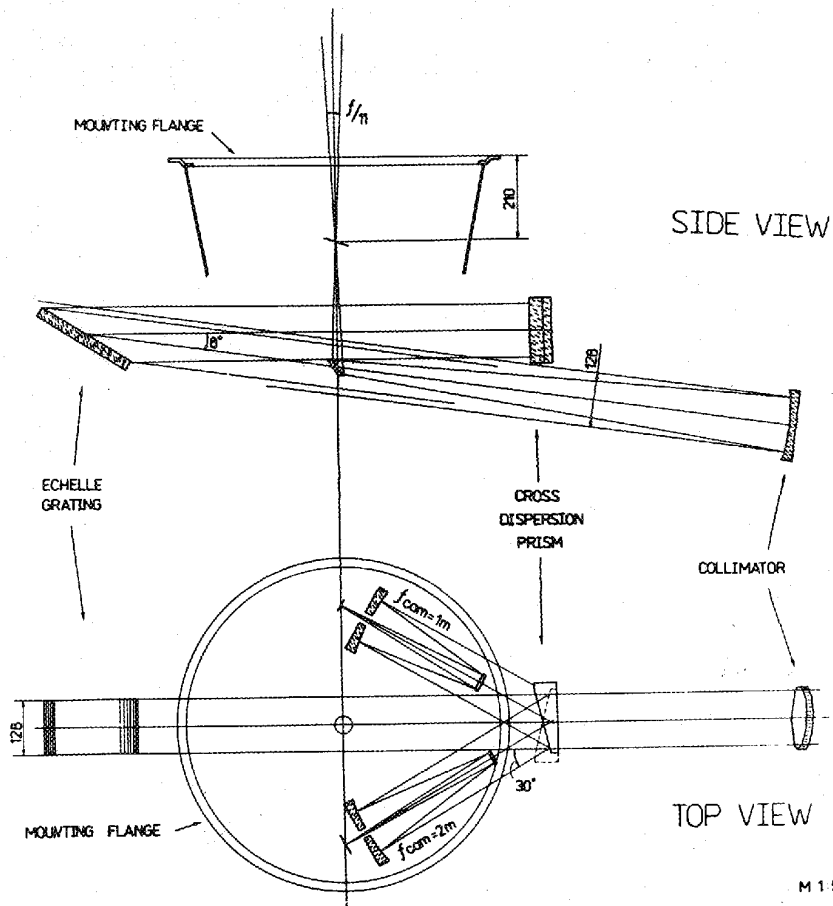
The entrance slit (1) in Fig. 1.3 is situated at the distance 210 mm below the attachment flange. The mirrored slit plane is tilted with respect to the optical axis by $13^\circ 5'$ in order to be viewed by the intensified TV guiding camera. The slit width is remotely controlled and depends on the spectral resolution being used, whilst the width of the decker can be changed manually and defines the height of spectral orders and the interorder spacing.

The filter and shutter unit (2) in Fig. 1.3 is mounted below the entrance slit in one assembly unit. A hollow cylinder with two radial slots attached to the axis of a stepping motor constitutes the shutter. The turret with the filter wheel attached to a stepping motor contains eight holdings for filters which have 16 mm in diameter and 6 mm in thickness (the effective focal length of the collimator depends on the filter thickness). The filters reduce the amount of scattered light diffused on the spectrograph optical frames and surfaces, and are selected according to the spectral region being used. The bandpasses are given in the following table together with their numbers and positions on the turret. Some of the filters are composed of two pieces to keep the thickness constant: a metal ring spacer between the pieces eliminates possible optical interference on their surfaces.

0	0	Closed		
1	7	Open		
2	6	3000 - 25000	Neutral	double
3	5	8500 - 25000	Infrared	double
4	4	7000 - 25000	Red	single
5	3	6000 - 25000	Orange	single
6	2	3500 - 6000	Blue	double
7	1	3500 - 7500	Transparent	double

The beam switcher (3) in Fig. 1.3 is used to render the light from the two calibration sources to the slit. It consists of a pentaprism attached to the stepping motor axis via a rotating arm. In the position shown with the solid line, the slit is unobscured for the light from the telescope, the position shown with the dashed line gives the light from the flat field lamp.

The calibration sources include a tungsten flat field lamp (5) in Fig. 1.3, and a ThAr hollow cathode spectral lamp (6) manufactured by S. & J. Juniper & Co., UK. The pupils of the lamps are collimated at $f/11$.



M 15

Figure 1.1: The optical layout of the SOFIN spectrograph. The converging $f/11$ beam focussed onto the slit is redirected by the flat mirror to the collimator. The collimated beam illuminates the échelle grating which renders the light dispersed in wavelength to the cross-dispersion prism to separate the spectral orders in the direction perpendicular to the dispersion. The two flipped positions of the cross-dispersion prism are shown by the solid and dashed lines. Depending on the position, the beam is directed to one of the optical cameras mounted in the spectrograph. The échelle image is formed on the CCD attached to the optical camera.

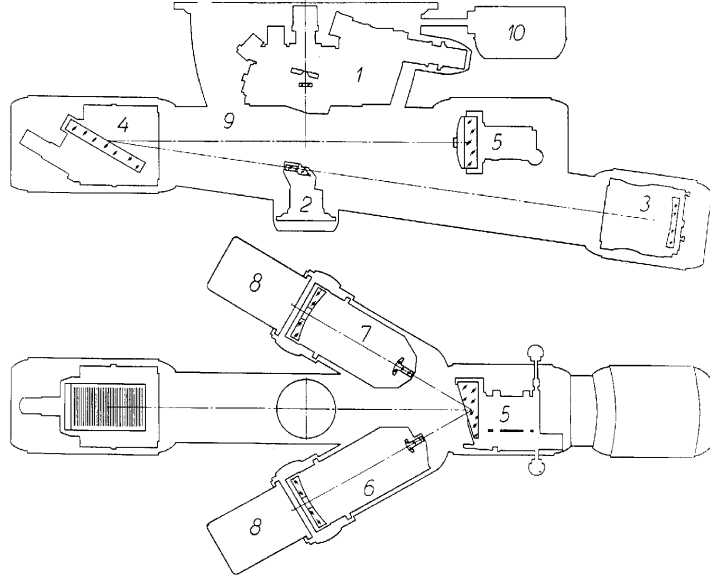


Figure 1.2: The mechanical layout of the SOFIN spectrograph: the upper unit (1) is shown in details in Fig. 1.3, flat mirror (2) with the adjustment mechanism, collimator (3), échelle grating (4), cross-dispersion prism (5) with the handle to flip the prism, two optical cameras (6 and 7) installed, CCD cameras (8), assembly frame (9), and power supply with the stepping motor amplifiers (10).

The intensified CCD TV guiding camera (4) in Fig. 1.3 is used for setting, focussing, and guiding the stellar image on the slit. The field of view on the TV screen is $70''$. With the maximum intensification a star as faint as 16^m can be seen. For bright objects a gray filter with an attenuation of 100 is put in front of the TV camera. The shutter, gray filter, and open diaphragm are installed on a remotely controlled linear shaft.

The analyzer of circular polarization (Stokesmeter) (8) in Fig. 1.3 is mounted on a platform above the slit and can be positioned onto the optical axis when used for spectropolarimetry. The design of the Stokesmeter is described by Plachinda & Tarasova (1999) and is similar to that of Donati & Semel (1990). It consists of an achromatic (4000–6800 Å) turnable quarter-wave plate, a beam splitter, made of a plate of Iceland spar, and a fixed achromatic quarter-wave plate on exit which converts the linearly polarized light into circularly polarized light to avoid linear polarized light attenuation on the échelle grating. The angle of the turnable quarter-wave plate on the entrance is controlled by a stepping motor; four exposures with the plate subsequently turned by 22.5° allows to measure all four Stokes

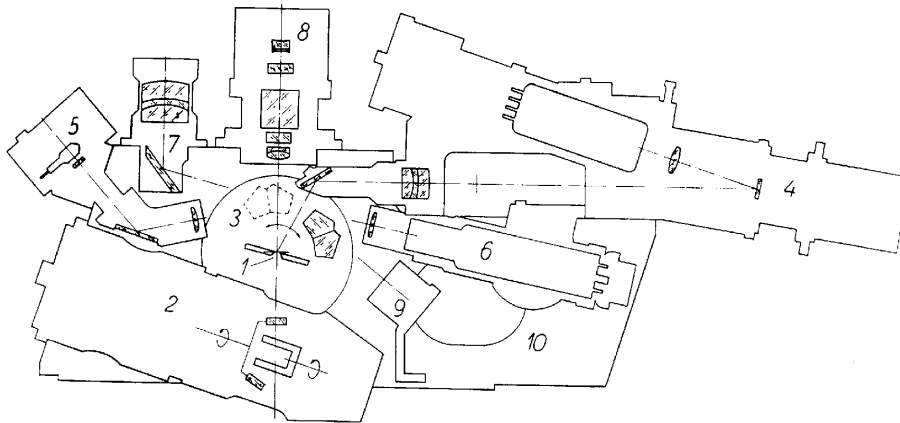


Figure 1.3: The mechanical layout of the upper unit: slit (1), filter turret and the shutter (2), pentaprism rotator (3), intensified guiding TV camera (4), flat field lamp (5), comparison spectrum ThAr lamp (6), an auxiliary viewing pupil (7), Zeeman analyzer (8), stray light absorber (9), and the assembly unit (10).

parameters. The image separation is $3''$ on the slit.

The *diagonal flat mirror* (2) in Fig. 1.2 is located 300 mm below the entrance slit and turns the optical axis by 98° . The projected diameter is 32 mm.

The *parabolic collimator mirror* (3) in Fig. 1.2 has a diameter of 128 mm and a focal length of 1396 mm. The effective focal length of the collimator coupled with the filters is 1400 mm. The mirror has been aligned once during assembly and any temperature changes of its focal length are compensated by the focussing of the optical cameras.

The *photon counter* (not shown but located between 2 and 3 in Fig. 1.2) is used to estimate the amount of light passed through the slit of the spectrograph and consists of a small prism installed in the collimated beam and a photomultiplier. The photon count rate and accumulated sum during the object exposure are displayed in real-time in order to suggest the exposure time in case of observing in modest weather conditions.

The *R2 échelle* (4) in Fig. 1.2 (Milton Roy Co., USA), has a grooved area of $128 \times 256 \text{ mm}^2$ and is ruled with $79 \text{ grooves mm}^{-1}$. The blaze angle is $63^\circ 435$ (arctan 2). The incident and diffracted beams are separated by a fixed angle of 8° and the angles are coplanar with the échelle normal. The échelle tilt mechanism changes the angle of incidence by turning the frame around ball-edged pivots within

$\pm 3^\circ$ by driving the tangent arm attached to the axis of the remotely controlled stepping motor. The motor step size is about one pixel on the CCD for the long camera. The working spectral orders are 20–65 (11 300 – 3500 Å).

The double-pass cross-dispersion prism (5) in Fig. 1.2 is made of BK7 glass and mounted 800 mm apart from the échelle. The prism apex angle is $17^\circ 02' 12''$ which makes the interorder spacing 75% of the order height at 5650 Å in the central 40th order. The positioning mechanism of the prism is similar to that of the échelle and allows to change the spectral setting in the cross-dispersion direction. The motor step size is about one pixel on the CCD for the long camera. The prism assembly is mounted on a mechanism which allows to turn the prism around the optical axis to redirect the refracted beam to one of the two optical cameras installed simultaneously in the spectrograph.

Three optical cameras provide three different spectral resolutions; two of them (6 and 7 in Fig. 1.2) can be installed in the optical ports at the same time and the resolution is altered by flipping the cross-dispersion prism. The short and long cameras are interchangeable, the medium camera is mounted permanently.

1. The long optical camera is a Cassegrain mirror system with an effective focal length of 2079 mm and provides a resolving power ranging from 150 000 to 185 000 which depends on the échelle deflection angle. The entrance slit width projected on two CCD pixels is $38 \mu\text{m}$ ($0''.28$ on the sky) at the blaze angle. The light loss on the slit with a seeing of $1''$ is 75%. The length of the spectral orders is about 20 Å around 5500 Å which corresponds to a pixel size of about 1000 m s^{-1} in radial velocities. About 15 adjacent spectral orders can be covered in one CCD image. The vignetting in the image centre is about 7% and almost homogeneous along the image.
2. The medium optical camera is a Ritchey-Chrétien mirror system with an effective focal length of 1000 mm with a spectral resolution ranging from 70 000 to 86 000. The entrance slit width projected on two CCD pixels is $82 \mu\text{m}$ ($0''.6$) at the blaze angle. The light loss on the slit is about 50% if the seeing is $1''$. The length of the spectral orders is about 40 Å around 5500 Å. The CCD format allows to record 12 such orders in one exposure. The pixel size corresponds to about 1900 m s^{-1} in radial velocities. The vignetting in the image centre is about 16% and increases towards the edges (68%).
3. The short optical camera is a meniscus system (two menisci and two mirrors) has an effective focal length of 348 mm and provides a spectral resolution from 25 000 to 30 000 with the entrance slit width of $236 \mu\text{m}$ ($1''.73$) projected on two CCD pixels. There is virtually no light loss on the slit since it is wider than the average seeing. The light loss occurs mostly on the slit decker which is reduced for the camera as compared to the others for better order separation in cross-dispersion. The spectral format of the camera allows to record all spectral orders in one image from 20 to 67 with the length of one

order being around 120 \AA at 5500 \AA . Two such exposures are necessary to get the complete overlap and full wavelength coverage of all spectral orders. The pixel size corresponds to 5700 m s^{-1} in radial velocities. The vignetting of the camera is 22% in the image centre and 92% at the edges is due to the large secondary mirror.

The parameters of the first two optical cameras are given in the following table (units are mm); the optical diagram of the third camera is given in the original paper of Pronik (1995):

N_{cam}	f_{cam}	R_1	R_2	e_1^2	e_2^2	D_1	D_2	d_1	d_2
1	2079	-852.05	-216.36	1	2.2957	160	40	-340	420.05
2	1000	-937.50	-635.30	1.247	12.2233	160	60	-300	356.00

where f_{cam} is the focal length, R is the radius of the mirror curvature, e^2 is the eccentricity, D is the diameter of the mirror, d_1 is the distance between the mirrors, and d_2 is the distance between the focal plane and the secondary mirror.

Each camera is equipped with a focussing mechanism which is a turnable threaded ring to offset the image formed on the CCD along the optical axis whilst the positions of the optical elements of the camera remain unchanged. The CCD camera is attached to the optical camera via a bayonet adapter which preserves the CCD adjustment after re-installation of the optical and CCD cameras. The bayonet connectors are equipped with adjustment screws to align the CCD pixels with respect to the cross-dispersion direction.

Two similar Astromed-3200 CCD cameras (8) in Fig.1.2 make use of two UV-coated EEV CCDs: P88100 (1152×298 pixels) and P88200 (1152×770 pixels) which are housed in liquid nitrogen cooled dewars and operated at a temperature of 150 K. The pixel size is $22.5 \times 22.5 \mu\text{m}^2$. The dewar window is made of Spectrosil B fused silica, 50 mm in diameter and 2 mm in thickness. The first one, the larger format CCD camera, is used with the long and short cameras, the second one, the smaller format CCD, is used with the medium resolution camera.

1.4 Efficiency of the spectrograph

The overall efficiency of the system including telescope and spectrograph is defined as the fraction of the photons entering the main mirror which is detected by the CCD.

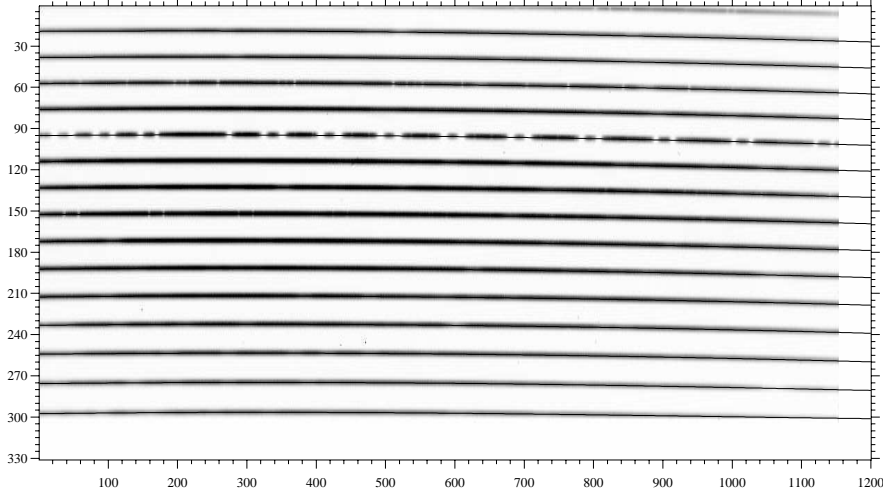


Figure 1.4: An échelle image of the RS CVn star IM Peg obtained with the medium camera; $R = 80\,000$ in the 6173 & 6563 Å spectral region. The spectral orders located during data reduction are shown. The wavelengths of the spectral orders increase from bottom to top. The O_2 atmospheric bands at 7600 Å are clearly seen in the 5th order from the top.

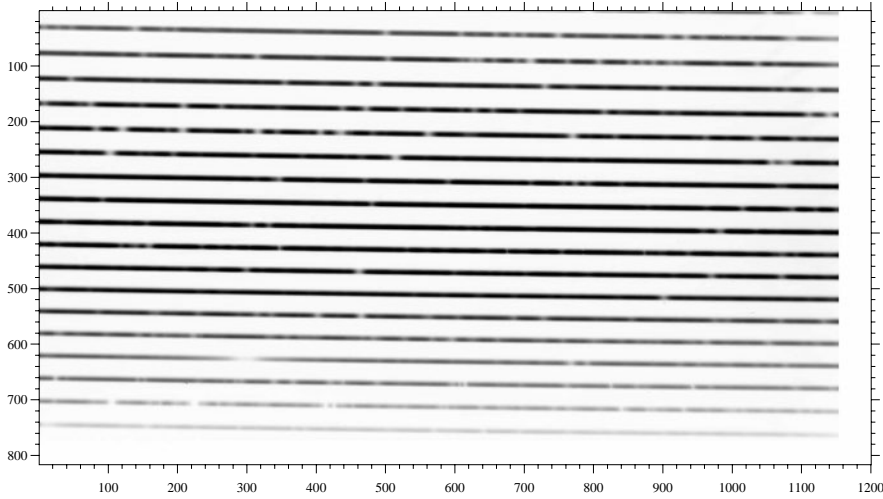


Figure 1.5: A raw échelle image of α Tau obtained with the long optical camera; $R = 160\,000$ in the 6427 & 7516 Å spectral region. The wavelengths of the spectral orders increase from top to bottom.

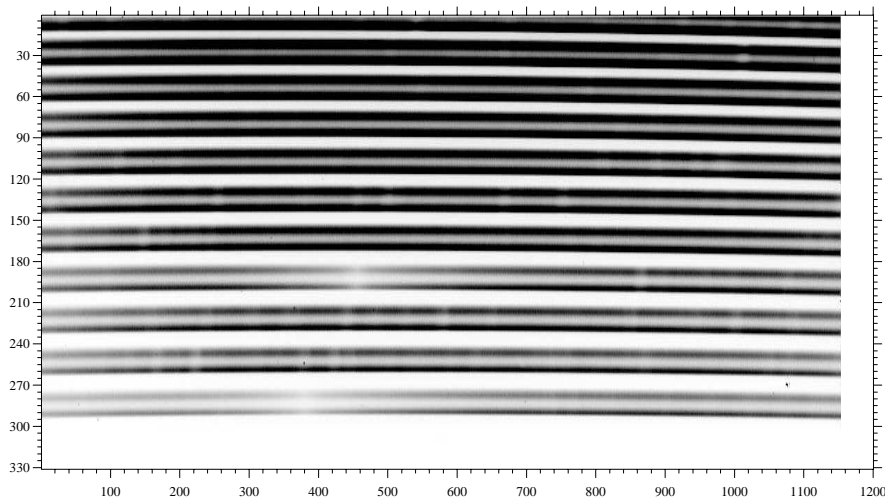


Figure 1.6: A raw échelle image of the magnetic Ap star α^2 CVn recorded with the Zeeman analyzer with the medium optical camera $R = 80\,000$ around 4500 \AA . The doubled spectral orders are the left and right polarized beams.

1.4.1 The direct measurement of the efficiency

Measurements of the spectrograph efficiency are usually done by observing stars with known energy distributions at different wavelengths, e.g. the set of bright secondary standard stars for flux calibration given in Taylor (1984) and Hamuy et al. (1992). Instead of the standard method, we used the programme observations of two G-type stars obtained during different observing runs at a range of zenith distances and meteorological conditions to estimate the efficiency in the red.

The central CCD order was used where the vignetting effect is minimal. The width of the cross-dispersion profile was used as the estimate of the seeing condition during the exposure. Assuming that the seeing profile is a Gaussian, the relative transmittance of the slit is given by

$$T = \operatorname{erf} \left(\frac{w \sqrt{\ln 2}}{\text{FWHM}} \right), \quad (1.1)$$

where the seeing profile width is given by FWHM, and w is the slit width. The transmittance is plotted as a function of the width ratio in Fig. 1.9. The measured signal-to-noise ratio (SNR) at the selected order, corrected for the slit effect, and reduced to the same exposure time was plotted in logarithmic units with respect to the airmass of the observations. The upper envelope of the points was used for linear extrapolation to the zenith.

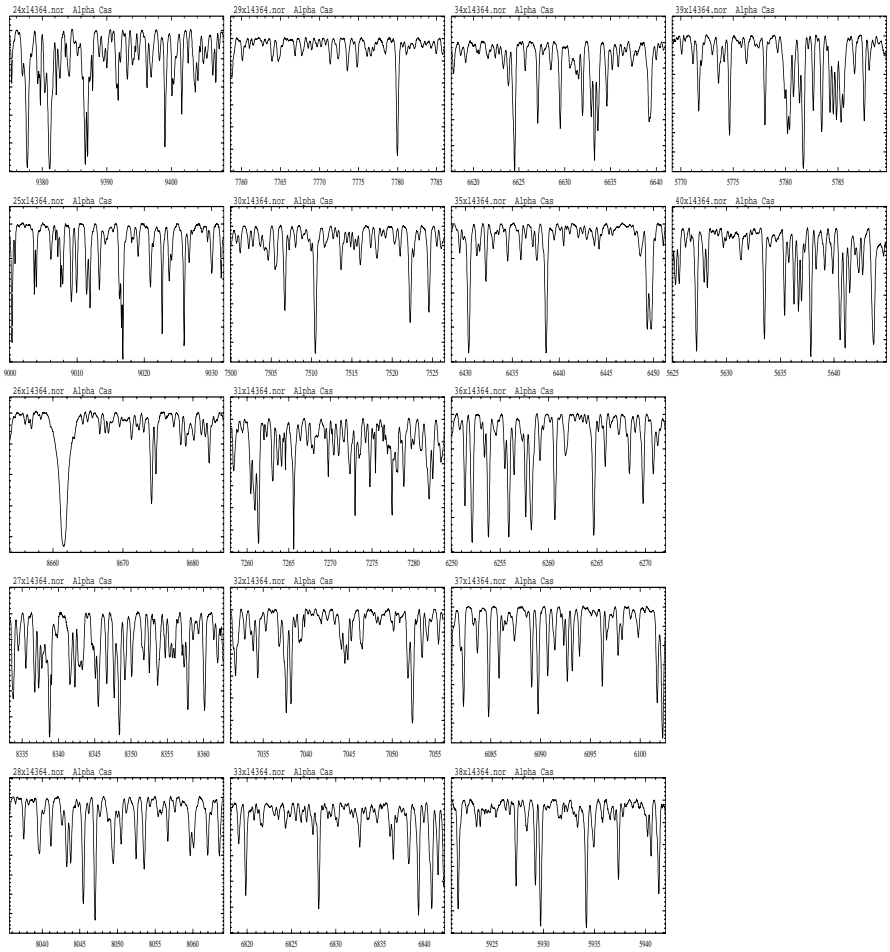


Figure 1.7: The reduced spectra of α Cas ($V=2.20$, K0 IIIa) with resolution $R = 160\,000$ in the 6427 & 7516 Å spectral region.

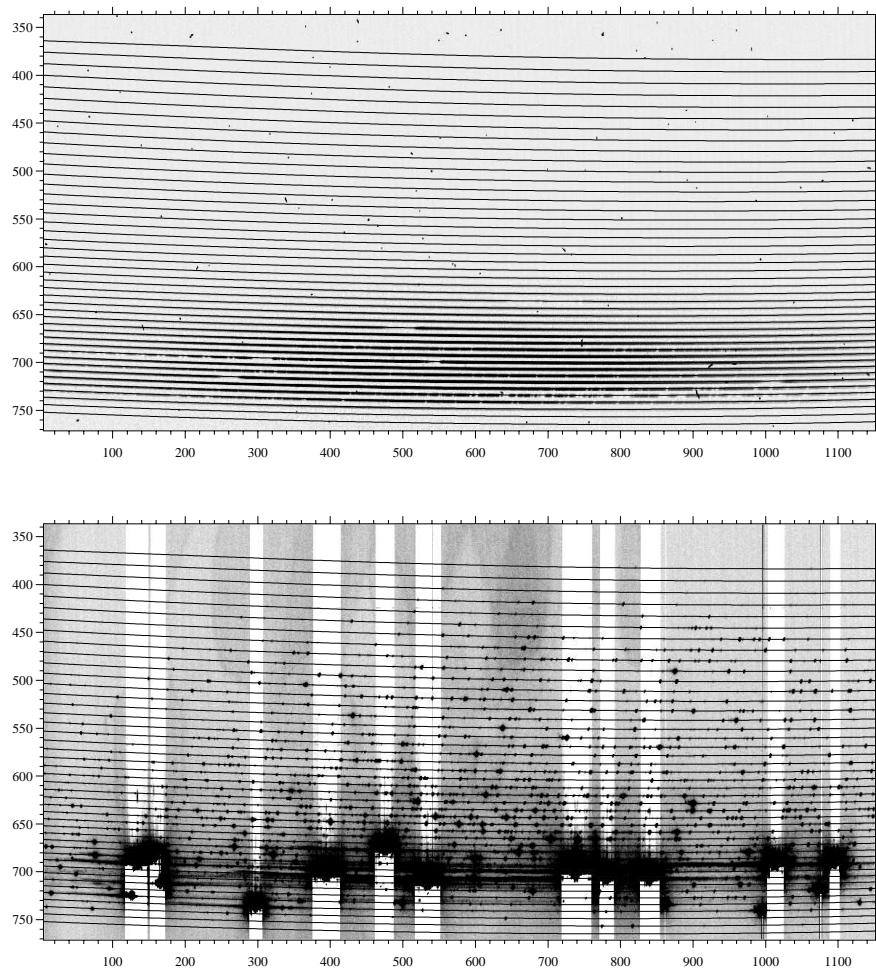


Figure 1.8: Echelle images taken with the low resolution $R = 30\,000$ optical camera. The horizontal curves indicate the position of the spectral orders found during data reduction. *Top:* preprocessed image with the scattered light surface subtracted prior to the weighted extraction of the spectral orders of the 20 min exposure of the FU Ori star V1057 Cyg ($V=10$) which gave a signal-to-noise ratio around 100 in the continuum at $H\alpha$. *Bottom:* The corresponding ThAr comparison spectrum image taken in the same spectral region. The bright Thorium lines in the red are overexposed to allow a large number of fainter lines to be seen and used for the calibration. The saturated lines produce vertical white “tails” areas, i.e. of depressed bias level.

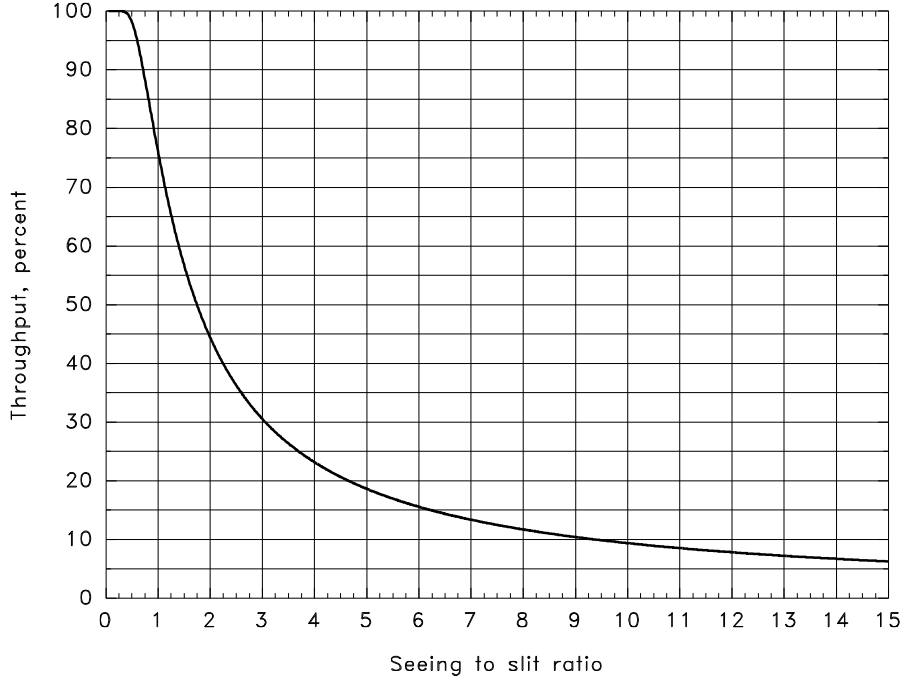


Figure 1.9: Throughput of the slit illuminated by a Gaussian seeing image. The horizontal axis is the ratio of the FWHM of the Gaussian seeing profile and the slit width.

58 observations of 31 Aql ($V=5.20$, G7IV) were made with the long camera with the slit width $37 \mu\text{m}$ ($0''.27$) which gives the resolution $R = 160\,000$ ($\Delta\lambda=0.020 \text{ \AA}$ per pixel) in the central order 35 at 6440 \AA . Extrapolation to the zenith estimates SNR to be 470 in 10 min of exposure time without the light loss on the slit. The flux outside of the Earth atmosphere expected for the star is $1100 \text{ photons cm}^{-2} \text{ s}^{-1} \text{ \AA}^{-1}$ (interpolated from Allen 1976, p. 207). The monochromatic Earth atmosphere extinction at 6440 \AA is 0.057 per airmass (the extinction coefficients for the La Palma Observatory were provided by the Carlsberg Meridian Telescope). For the given diameters of the telescope mirrors (256 and 51 cm respectively), the expected SNR of the star at zenith is 2260. Hence, the efficiency for the long camera is estimated to be 4.3%.

92 observations of HD 199178 ($V=7.24$ G2III) were made with the medium camera with the slit width $81 \mu\text{m}$ ($0''.60$) which provides the resolution $R = 76\,000$ ($\Delta\lambda=0.042 \text{ \AA}$ per pixel) in the central order 32 at 7000 \AA . Extrapolation to the zenith estimates SNR to be 300 in 10 min of exposure time without the light losses on the slit. The extra-atmosphere flux for the star is about $970 \text{ photons cm}^{-2} \text{ s}^{-1} \text{ \AA}^{-1}$.

The atmospheric extinction at 7000 Å is 0.033 per airmass, hence the expected SNR of the star at zenith is 1220 which gives the efficiency for the medium camera of about 6%.

1.4.2 The expected efficiency

The efficiency can also be estimated by calculating the transmissions of all optical surfaces of the spectrograph. The results of these detailed calculations are given in Tab. 1.1. The telescope reflectance is given by direct measurements after the cleaning of the mirrors. The reflectance on a surface at normal incidence is calculated according to the Fresnel formula:

$$r = \left(\frac{n - 1}{n + 1} \right)^2, \quad (1.2)$$

where the refractive index n is 1.51 at 7000 Å for BK7 glass. The internal transmittance of BK7 is 0.99988 per mm (Optics Guide, Melles Griot Co. 1988). The échelle reflectance was provided by its specification. The reflectance of all SOFIN mirrored surfaces aluminized in 1990 is estimated to be 0.8.

The overall efficiency of the spectrograph and CCD is 6.8%. By including the telescope, the efficiency is reduced to 4%, which is in good agreement with the direct measurements.

For comparison, the coudé échelle spectrometer at the 2.7 m telescope of the McDonald Observatory has an estimated efficiency of the spectrograph of 16%, mainly because of the silver coated surfaces (97.5% reflectance), and the higher CCD efficiency (77%).

A similar design échelle spectrograph at the 4 m telescope of CTIO has an efficiency ranging from 4–8% depending on the optical system setup.

1.5 Model of the spectrograph

Present day CCDs which are used in the spectrograph are too small to cover the whole spectral range of the échelle image. Hence, the observations are carried out in selected settings of the échelle and prism angles with limited spectral coverage. It is a matter of importance to have an appropriate means to select the configuration of spectral lines (Fig. 1.10) and the pointing model of the spectrograph which transforms the coordinates of the spectral setting into the instrumental units of échelle and prism.

Table 1.1: The transmission table of the optical elements of the SOFIN spectrograph. The total transmission coefficients for each subsection are given in the rightmost column.

Telescope main mirror	reflection	0.786	
secondary mirror	reflection	0.782	0.60
Filter	surface	0.96	
	single pass, 3 mm	0.99963	
	surface	0.96	0.92
Compensating glass	surface	0.96	
	single pass, 3 mm	0.99963	
	surface	0.96	0.92
Diagonal mirror	reflection	0.8	
Collimator	reflection	0.8	
Echelle	reflection	0.67	
	vignetting	0.87	0.37
Cross-dispersion prism	surface	0.96	
	first pass, 39 mm	0.9953	
	reflection	0.8	
	second pass, 39 mm	0.9953	
	surface	0.96	0.73
Camera main mirror	reflection	0.8	
secondary mirror	reflection	0.8	0.64
CCD window	surface	0.96	
	single pass, 3 mm	0.99963	
	surface	0.96	0.92
UV-coated EEV CCD	QE at 7000 Å		0.50

1.5.1 Spectral mosaic

The échelle grating equation is

$$\sin \alpha + \sin \beta = N k \lambda \quad (1.3)$$

with

$$\alpha = \theta + \gamma + \epsilon \quad \text{and} \quad \beta = \theta - \gamma + \epsilon + \delta, \quad (1.4)$$

where α and β are the angles of incidence and diffraction, γ is the fixed angle of 4° (2γ is the angular separation of collimator and prism), θ is the blaze angle, ϵ is the échelle deflection angle with respect to the blaze, δ is the field angle varying around

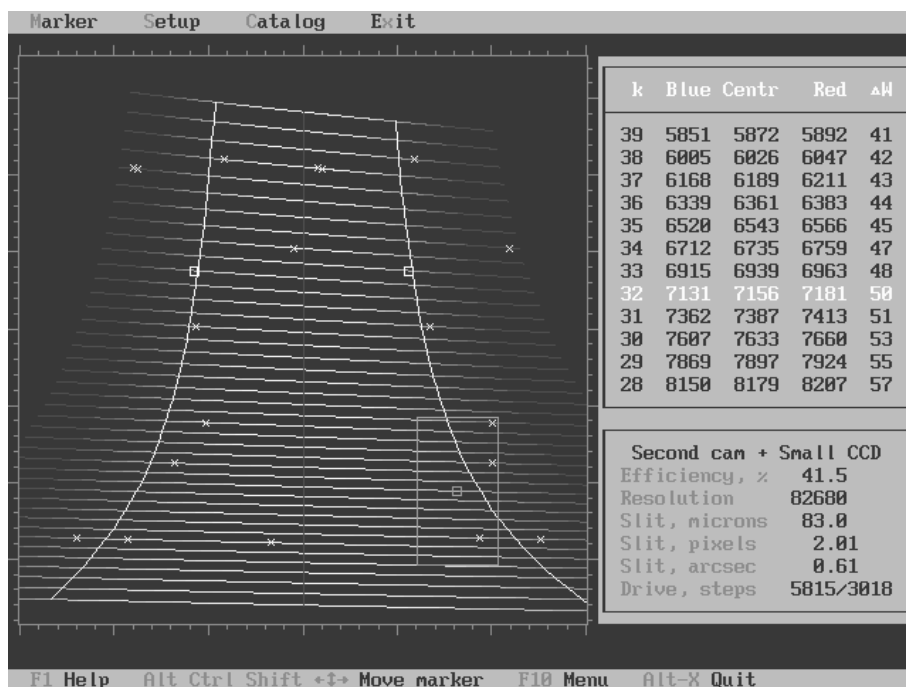


Figure 1.10: The model of the focal plane of the spectrograph as seen on the computer screen: the red orders are at the bottom and the blue orders are at the top. The blaze axis is at the centre, the two white curves at 41% of the échelle efficiency indicate the interval of the full wavelength overlap. The CCD box and the wavelength coverage correspond to the medium optical camera in 6173 & 6563 Å spectral region. The positions of some hydrogen and Ca lines are marked with crosses and boxes.

the image centre in dispersion direction, N is the number of grooves per mm, k is the spectral order number, and λ is the wavelength. The incidence and diffraction angles are in the same plane for this spectrograph (various configurations of échelle spectrographs were extensively discussed in Schroeder & Hilliard 1980).

The cross-dispersion prism equation describes the fact that the monochromatic ray crosses the surface two times at different angles and becomes internally reflected on the rear mirrored surface:

$$\arcsin\left(\frac{\sin \alpha_p}{n}\right) + \arcsin\left(\frac{\sin \beta_p}{n}\right) = 2\theta_p, \quad (1.5)$$

where α_p and β_p are the angles of incidence and refraction, θ_p is the prism apex angle. The refraction angle is given by the following sum:

$$\beta_p = \alpha_p + \gamma_p + \delta_p, \quad (1.6)$$

where $\gamma_p = 30^\circ$ is the fixed angular separation between the échelle and the optical camera, and δ_p is the field angle varying around the image centre in cross-dispersion direction.

The refractive index n of BK7 is approximated by

$$n^2 = A_1 + A_2\lambda^2 + A_3\lambda^{-2} + A_4\lambda^{-4} + A_5\lambda^{-6} + A_6\lambda^{-8} \quad (1.7)$$

with the wavelength λ given in μm , and the polynomial coefficients (Pronik 1995)

$$\begin{aligned} A_1 &= 2.2699804 & A_2 &= -9.8250605 \times 10^{-3} \\ A_3 &= 1.10172030 \times 10^{-2} & A_4 &= 7.6606834 \times 10^{-5} \\ A_5 &= 1.16169520 \times 10^{-5} & A_6 &= 5.81309000 \times 10^{-7}. \end{aligned}$$

The image formed in the focal plane is calculated in the coordinate system (ϵ, β_p) of the échelle deflection and the prism refraction angles as a function of ϵ and order number k :

$$\alpha_p(\lambda) = \alpha_p(\lambda(\epsilon, k)) \quad (1.8)$$

in the image centre with the field angles $\delta = \delta_p = 0$. A box in the focal plane which reflects the CCD format is calculated in the angular units according to the scaling factor of the selected optical camera. The CCD box can be positioned to the different angles of échelle ϵ and prism β_p . The corresponding table of the wavelength coverage is calculated with the two angles fixed at the selected position and the field angles δ and δ_p are varying within the CCD image:

$$\delta_p(\lambda) = \delta_p(\lambda(\delta, k)). \quad (1.9)$$

1.5.2 The échelle efficiency

The échelle grating has its maximum reflectance at the blaze angle which decreases as the angle changes. Also, as the incidence angle increases, the projected area of the grating is reduced which results in a beam area reduction. The total effect is calculated allowing to estimate the light collection efficiency at the given spectral setting.

The light reflectance with respect to the blaze intensity ($\epsilon = 0$) is

$$I_\lambda = \left(\frac{\sin u}{u} \right)^2, \quad \text{where } u = \pi \left(k - \frac{\lambda_1}{\lambda} \right). \quad (1.10)$$

The quantity $\lambda_1 = 225\,885.77\text{ \AA}$ is the wavelength in order $k = 1$ at the blaze angle ($N \lambda_1 = 2 \sin \theta \cos \gamma$).

The transmittance of the light due to the change of the illumination area of the échelle by the collimated beam as a function of the grating angle is given by the ratio of the two areas $S_{\text{ech}}/S_{\text{col}}$:

$$\frac{1}{4}S_{\text{ech}} = (\sin 2\rho + 2\rho) D_{\text{col}}^2 - \pi D_{\text{obs}}^2, \quad \frac{1}{4}S_{\text{col}} = \pi D_{\text{col}}^2 - \pi D_{\text{obs}}^2 \quad (1.11)$$

with

$$\rho = \frac{L_y}{D_{\text{col}}} \cos \alpha,$$

where L_y is the length of the longest échelle side (across the grooves), D_{col} is the diameter of collimator, and D_{obs} is the diameter of the diagonal flat mirror, which obscures the central part of the collimated beam. It is assumed that the collimated beam size equals the width of the échelle $D_{\text{col}} = L_x$. The transmittance decreases from 94% to 77% from the blue to the red side of the order; additionally, the resolution increases from blue to red.

The overall efficiency is shown in Fig. 1.11 as obtained by the multiplication of the blaze function with the transmittance. The maximal efficiency at the blaze angle is about 86%.

1.5.3 The resolving power

The resolving power $R = \lambda/d\lambda$ is one of the basic parameters of the spectrograph and describes its ability to resolve narrow spectral lines. For the given focal length of the optical camera, the resolution is a function of the échelle angles and it changes along spectral orders. Qualitatively, it is obvious that with the increase of the angle of incidence, the projected density of the grooves becomes higher, which results in a larger dispersion.

The wavelength size $d\lambda$ of the resolution element formed by the slit projection onto the CCD is

$$N k d\lambda = \cos \beta d\beta, \quad \text{where} \quad d\beta = \frac{p}{f_{\text{cam}}} \quad (1.12)$$

is the angular size of the resolution element given by the projected slit width p on the CCD and the focal length of the camera f_{cam} . Then the resolving power is

$$R = \frac{\lambda}{d\lambda} = \frac{\sin \alpha + \sin \beta}{\cos \beta} \cdot \frac{f_{\text{cam}}}{p} \quad (1.13)$$

which is a function of the échelle deflection angle ϵ , field angle δ , and the projected slit width p (the entrance slit width also depends on the above two angles). For the CCD centre at $\delta = 0$ it becomes

$$R = \frac{2 \tan(\theta + \epsilon)}{1 + \tan(\theta + \epsilon) \tan \gamma} \cdot \frac{f_{\text{cam}}}{p}. \quad (1.14)$$

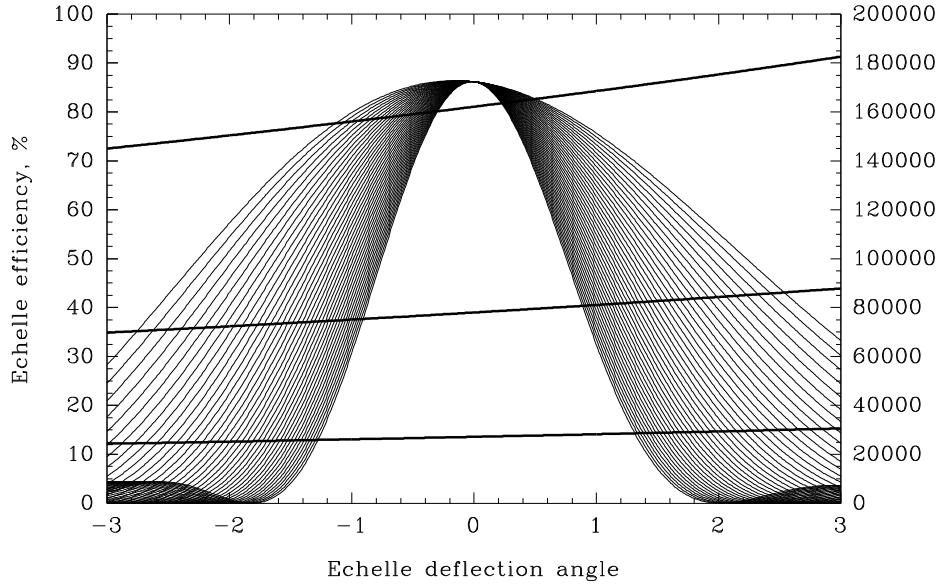


Figure 1.11: The échelle plus collimator efficiency is plotted with respect to the deflection angle in degrees. The uppermost curve corresponds to the red 20th order, and the innermost curve is for the blue 60th order. The resolving power is calculated for the three optical cameras for a resolution element of two pixels of the CCD.

1.5.4 The optimal slit width

The slit is called optimal when its image in the focal plane is optimally sampled by the CCD pixels. For the ordinary observing mode, the sampling interval is equal to one CCD pixel, which implies that the spatial cutoff (or Nyquist) frequency corresponds to two pixels on the CCD. The slit width which corresponds to an instrumental profile of two pixels FWHM is used for observations to provide the maximal resolving power for the given settings of the spectrograph.

The projected slit image is a convolution of three main profiles: the geometrical projection of the rectangular entrance slit, the aberration profile of the camera,

and the diffractive profile of the monochromatic beam on the collimated pupil. To calculate the resulting width, it is assumed that the profiles are Gaussians, hence, their widths can be added in squares:

$$p^2 = \left(\frac{f_{\text{cam}}}{f_{\text{col}}} \cdot \frac{\cos \alpha}{\cos \beta} \cdot w \right)^2 + A^2(\lambda) + \left(\frac{\lambda}{D_{\text{col}}} f_{\text{cam}} \right)^2. \quad (1.15)$$

The last term describes the diffraction broadening of the slit image. The middle term is the camera aberration as a function of image position; for simplicity, the aberration spot size is set constant and equal to $8 \mu\text{m}$ for all three optical cameras. The first term consists of the three factors: the magnification factor of the spectrograph, the angular magnification on the échelle, and the entrance slit width w . The magnification by the échelle follows from Eq. (1.3): $\cos \alpha d\alpha + \cos \beta d\beta = 0$.

The essential setup parameters for the three optical cameras are given in the following table for the central 40th order at 5647 \AA at the blaze. The slit width w , given in μm , corresponds to two pixels on the CCD. The slit relative throughput T in percent is calculated for $1''$ seeing. $\delta\lambda$ and δv are the pixel width in wavelength (m\AA) and radial velocities (m s^{-1}). $\Delta\lambda$ and Δk are the length in \AA and the number of spectral orders in the CCD image.

No.	Camera	R	w	w_{sky}	T	$\delta\lambda$	δv	$\Delta\lambda$	Δk
1	long	161 000	38	$0''.28$	25	17	930	20	16
2	medium	76 000	82	$0''.60$	50	37	1970	42	14
3	short	27 000	236	$1''.73$	100	104	5550	120	40

1.5.5 The pointing model of the spectrograph

The échelle and the cross-dispersion prism position angles are controlled by stepping motors. The pointing model establishes the relation between the step numbers and the position in wavelengths and order numbers for the centre of the CCD image and is used for the selection of spectral regions (Fig. 1.10).

To obtain the reference points, a series of comparison spectrum images were made in a grid of 5×7 different positions in dispersion direction and across the orders for the three optical cameras. The images were processed to obtain the central order number and its wavelength. Bivariate polynomial linear least-squares fits were used to approximate the échelle deflection angle ϵ in Eq. (1.3) and the central order number k as functions of the step motor numbers x and y as follows

$$\epsilon(x, y) = \mathbf{q}'(y)\mathbf{E}\mathbf{p}(x) \quad \text{and} \quad k(x, y) = \mathbf{q}'(y)\mathbf{C}\mathbf{p}(x), \quad (1.16)$$

where $\mathbf{E}_{1 \times 2}$ and $\mathbf{C}_{4 \times 1}$ are the matrices of polynomial coefficients associated with the vectors of the Chebyshev polynomials $\mathbf{q}(y)$ and $\mathbf{p}(x)$ of the corresponding

degrees. The polynomial coefficients were found sufficient for the SOFIN spectrograph to describe the surface with an appropriate accuracy, although, a more dense grid in the cross-dispersion direction would provide an accuracy similar to that achieved in the dispersion direction.

1.6 Stability of the spectrograph

As the alt-azimuth mounted telescope tracks the position of a star, the spectrograph mounted on the rotating adapter is changing its orientation which is described by the parallactic angle. The parallactic angle between the hour circle and the vertical circle (Woolard & Clemence 1966, p. 55) is calculated from

$$\begin{aligned}\sin z \sin q &= \cos \phi \sin h \\ \sin z \cos q &= \sin \phi \cos \delta - \cos \phi \sin \delta \cos h,\end{aligned}\tag{1.17}$$

where q is the parallactic angle, z is the zenith distance, ϕ is the latitude of the telescope in the northern hemisphere, δ is the declination of the object, and h is its hour angle. Fig. 1.12 shows how the rotator parallactic angle and the zenith distance of an object are changing in time. For a star with $\delta \approx \phi$ the rotator angle is changing very fast but the zenith distance is not. Apart from this declination, the slower change of the rotator angle is compensated by the near constancy of the zenith distance at the meridian. The most critical parts are on the east and west where both angles are changing very rapidly.

A change of the spectrograph orientation unavoidably results in a drift of spectral line positions, an effect known as the flexure of Cassegrain mounted spectrographs. Different optical components may change their positions in a different way as the spectrograph changes its orientation which makes the overall effect very complicated.

To evaluate the amplitude and the behaviour of the line drifts, an experiment was made in December 1997 for the long 1st and medium 2nd optical cameras as follows. To ensure that the ambient temperature changes are minimal, the experiment was carried out during a cloudy night with the telescope dome closed and the air conditioning system switched on. The altitude of the telescope was gradually decreased from 90° to 20° ; at each altitude the rotator was turned from -90° to $+90^\circ$, and at each rotator angle an exposure of the comparison spectrum was made. Then the whole sequence was repeated for the other camera. The line displacements were measured with respect to a group of lines at the image centre of the very first exposure with the cross-correlation technique. The results of the measurements are shown in Fig. 1.14, and the corresponding surfaces are shown in Fig. 1.15 and Fig. 1.16 which were approximated by a bivariate smoothing spline.

As was expected, the 1st camera traces show a twice larger amplitude due to

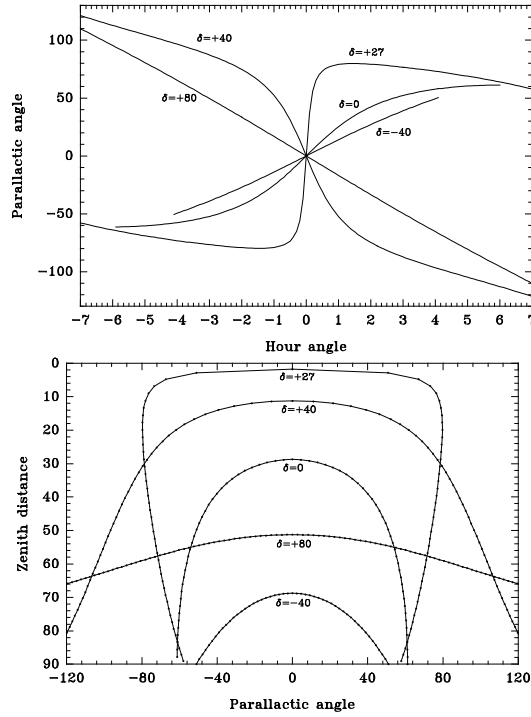


Figure 1.12: Change of the parallactic angle of the telescope rotator as function of hour angle (left) and zenith distance (right) at the latitude $\phi = 28.76^\circ$ of the NOT for stars with different declinations. The length of the curves is defined by the visibility of a star above the horizon. The time interval between two dots in the right panel is 10 min of hour angle.

the doubled focal length as compared to the other camera. At each trace when the altitude is fixed there is a turning point at which the drift in the direction of rows (the dispersion direction) is minimal and is at $+30^\circ$ of the rotator angle for the 1st camera and -30° for the 2nd. This is simply explained by the fact that the angle between the échelle-prism axis and the optical camera is 30° : at the corresponding rotator angle the camera is exactly in the plane of the vertical circle, therefore its bending is minimal (Fig. 1.13). As the zenith distance is changing, the lines are moving back and forth in the dispersion direction. The minimal change of the drift occurs at 30° zenith distance. There is no feasible explanation why it happens at this angle: probably there are some changes in the resulting vector of forces in the échelle turnable frame drawn out by the braced springs, but at 30° of zenith distance the angle between the échelle plane and the vertical is only 30° . The échelle stands vertical at a zenith distance of 60° , hence, the échelle unit counteracts the springs.

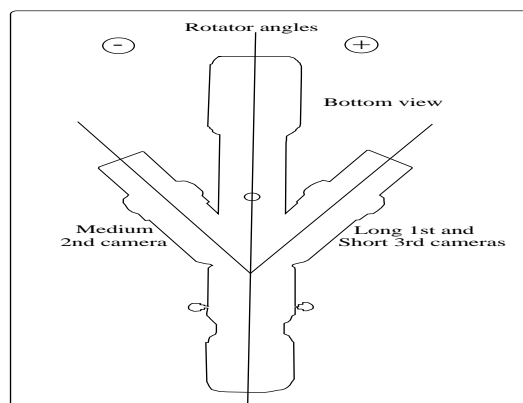


Figure 1.13: The bottom view of the spectrograph mounted on the telescope rotator adapter. Clockwise rotation corresponds to negative angles, and anticlockwise rotation corresponds to positive angles of the rotator. The angle between the optical cameras is 60° . When the rotator angle is -30° the medium 2nd camera is oriented in the plane of the vertical circle of the telescope.

The change of the spectral line width from one exposure to the other is shown in the surface fits. These surfaces are less conclusive but show that the focussing of the optical camera is degrading at certain orientations of the spectrograph and it is definitely degrading with increase of the zenith distance. One conclusion that can be made is that at the rotator angles ($\pm 30^\circ$), where the drift in the dispersion direction is minimal, the change of the focus is maximal.

The results of this experiment have merely practical consequences: to minimize the drift in the dispersion direction during observations the rotator angle for the long 1st camera should be around $+30^\circ$ (the same is true for the short 3rd camera where the measurements were not made but the mechanical configuration is the same), and -30° for the medium 2nd camera.

In order to obtain the optimal quality (stable lines and maximal resolution) long exposures should be subdivided into a series of short ones depending on the object position, with subsequent correction of the shifts.

1.6.1 Line broadening due to flexure

The drift of a spectral line across the CCD pixels during the integration results in an apparent shift of the line centre from where it is expected and leads to the increase of the line width. If the line shape can be described by a rectangular profile, then apparently, a shift of such a line by the amount Δ increases the line width by the same amount. Most of the real spectral lines can be described as

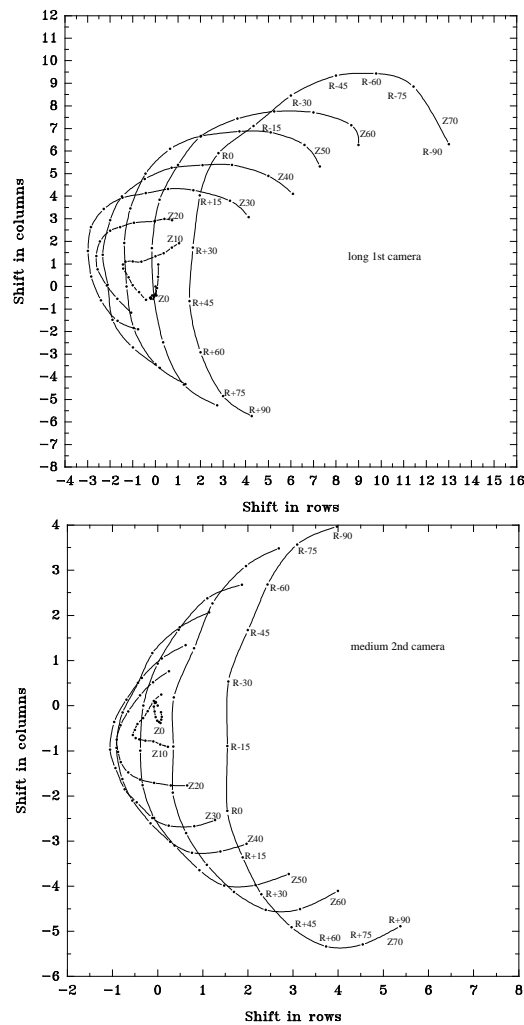


Figure 1.14: The line drift in two optical cameras as a function of the spectrograph spatial orientation. The shift in rows is along the dispersion direction and the shift in columns is in the cross-dispersion direction. The telescope rotator angle (R) is changing from -90° to $+90^\circ$ and the zenith distance (Z) is changing from 0° to 70° . The scale size for the medium camera plot is half that for the long camera plot.

Gaussian profiles; in the latter case the increase of the width due to the shift is less significant.

The whole process can be described as a convolution of the true line profile $p(x)$

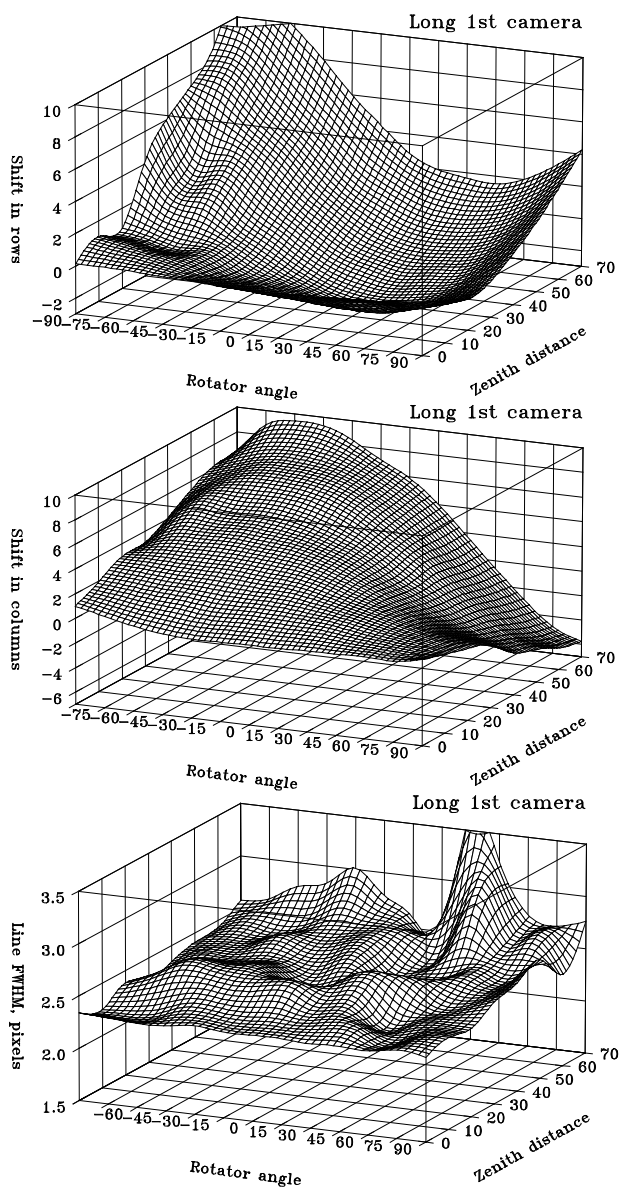


Figure 1.15: The surface fit shows the drift of a spectral line in the dispersion direction (upper panel), in the cross-dispersion direction (middle panel), and the change of the line FWHM as a function of zenith distance and rotator angle for the long 1st optical camera.

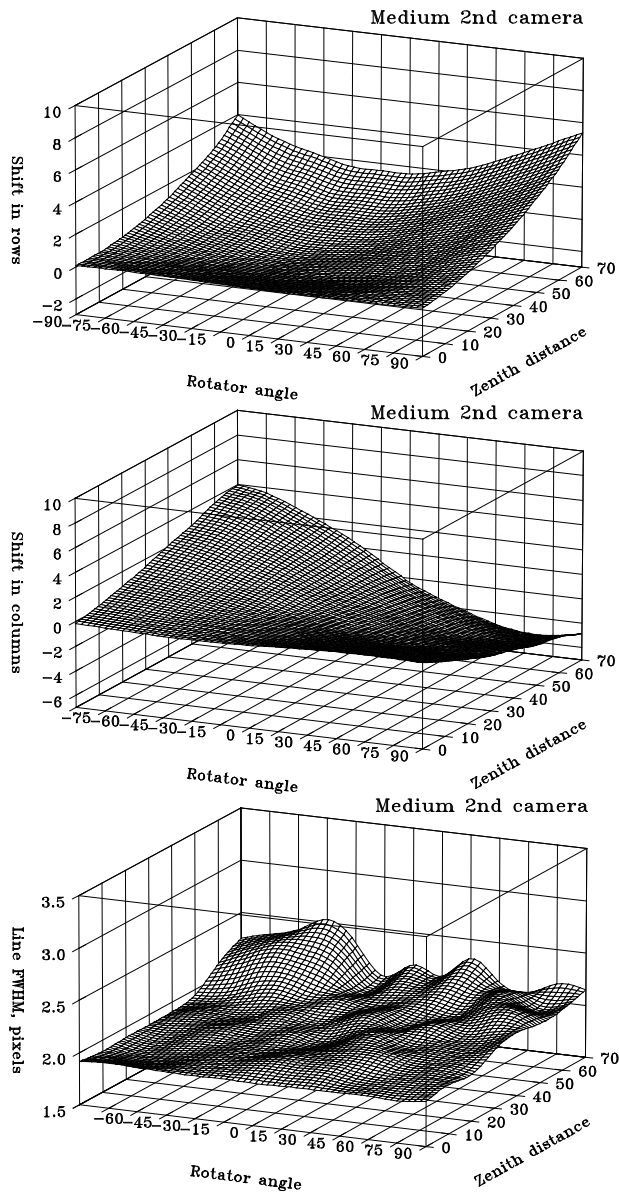


Figure 1.16: The surface fit shows the drift of a spectral line in the dispersion direction (upper panel), in the cross-dispersion direction (middle panel), and the change of the line FWHM as a function of zenith distance and rotator angle for the medium 2nd optical camera.

with the shift function $s(x)$ which results in the smeared profile $f(x)$. Assume that the shift function is a rectangular profile of the width Δ , i.e. the shift of the line is constant in time:

$$s(u) = \begin{cases} 1, & -\Delta/2 < u < +\Delta/2 \\ 0, & \text{otherwise.} \end{cases} \quad (1.18)$$

Let the line $p(u)$ be a Gaussian profile of the width σ , then the resulting profile is

$$f(x) = \int_{-\infty}^{+\infty} p(u) s(x-u) du = \int_{x-\Delta/2}^{x+\Delta/2} p(u) du = \int_{x-\Delta/2}^{x+\Delta/2} e^{-u^2/\sigma^2} du = \frac{\sqrt{\pi}}{2} \sigma (y_2 - y_1) \quad (1.19)$$

where

$$y_1 = \operatorname{erf}\left(\frac{x - \Delta/2}{\sigma}\right) \quad \text{and} \quad y_2 = \operatorname{erf}\left(\frac{x + \Delta/2}{\sigma}\right). \quad (1.20)$$

The resulting profile is not a Gaussian anymore but the difference of two error function profiles. The resulting full width w_f is calculated at half amplitude of the profile and plotted with respect to the width w_p and the shift Δ in the following form:

$$\frac{w_f}{w_p} = F\left(\frac{\Delta}{w_p}\right). \quad (1.21)$$

A more simple but less realistic case is when the shift function can be described by a Gaussian profile, i.e. the line position is a normally distributed random number with a mean equal to the expected line position and the width σ_2 (similar to the width Δ of the rectangular shift function). Then, the resulting profile is a convolution of the two Gaussians:

$$f(x) = \int_{-\infty}^{+\infty} p(u) s(x-u) du = \int_{-\infty}^{+\infty} e^{-u^2/\sigma_1^2} e^{-(x-u)^2/\sigma_2^2} du = \sqrt{\frac{\pi}{\sigma_1^2 + \sigma_2^2}} \cdot \sigma_1 \sigma_2 \cdot e^{-x^2/(\sigma_1^2 + \sigma_2^2)}. \quad (1.22)$$

The resulting curves for the two shift functions are shown in Fig. 1.17. A rectangular shift of a Gaussian profile of 2 pixels FWHM by two pixels would increase its width by 25%; a shift by four pixels doubles the line width.

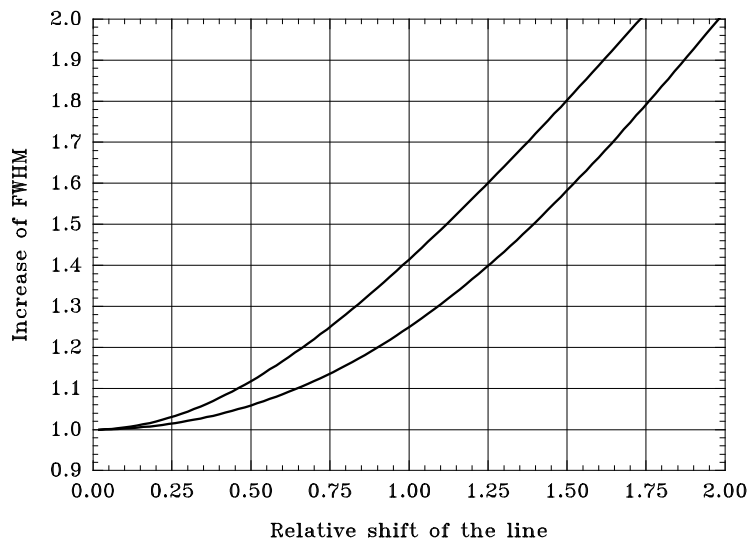


Figure 1.17: Relative increase of a Gaussian profiles FWHM as a function of the line shift with respect to its width. The bottom curve corresponds to a rectangular shift function, and the upper curve is for a Gaussian shift function.

To verify this in practice, we made an observation of α Cyg (A2 I) whose spectrum has very narrow interstellar absorption features in the Na I doublet. The observation was made with the 1st camera when the telescope was normally tracking the star and then when the telescope rotator was turned by 50° during the exposure. The comparison lines shifted by 0.5 pixels (425 m s^{-1}) during the exposure. The width of narrow absorption lines is about 4–5 pixels. The two spectra are shown in Fig. 1.18. No increase of the line width due to the shift was found in this experiment, because the expected increase of the line width is less than 1%.

1.6.2 Statical stability of the spectrograph

In this section we give an investigation of the statical stability of the spectrograph when the external long-term factors of the flexure due to telescope tracking are excluded. The importance of such a test is dictated by the need of understanding the nature of the positional instability of spectral lines due to instrumental effects. This is especially important when we study short term variations of spectral line profiles (e.g. non-radial pulsations or other monitoring programmes) where the physical effect could be compatible in amplitude with the effects of instrumental nature. On the other hand, slow variations (tens of minutes) of the line positions due to environmental effects give us additional suggestions of the proper operational modes of the SOFIN spectrograph which can be used to minimize the

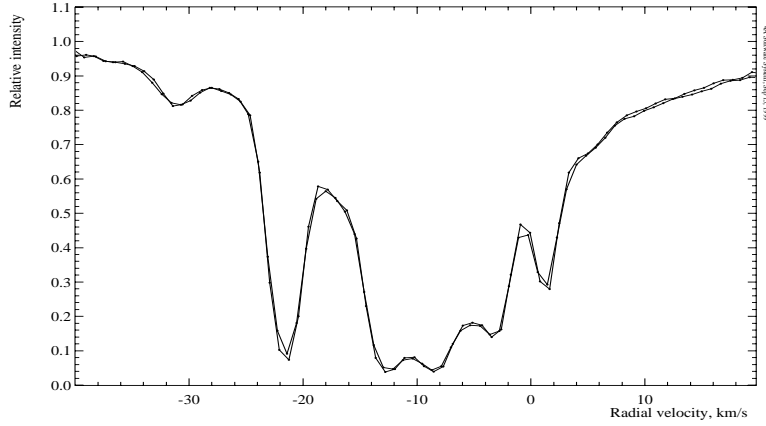


Figure 1.18: The reduced spectrum of α Cyg ($V=1.25$ A2Iae) taken with the long 1st camera ($R=176\,000$ at this spectral region) showing the profile of the interstellar Na I D₂ at 5889.9512 \AA . The two spectra were taken under different conditions: when the telescope was only tracking, and when the rotator was turned from 0° to $+50^\circ$ step by step during its 5 min exposure at the zenith distance of 20° . The rotation caused a shift of the comparison spectrum lines by 0.5 pixels (one pixel is 850 m s^{-1}). No apparent change of the width in the profile components is seen. The decomposition of the line profile onto a number of Gaussians also gives the same widths for the two spectra.

instrumental instability during observations and taken into account during data reduction.

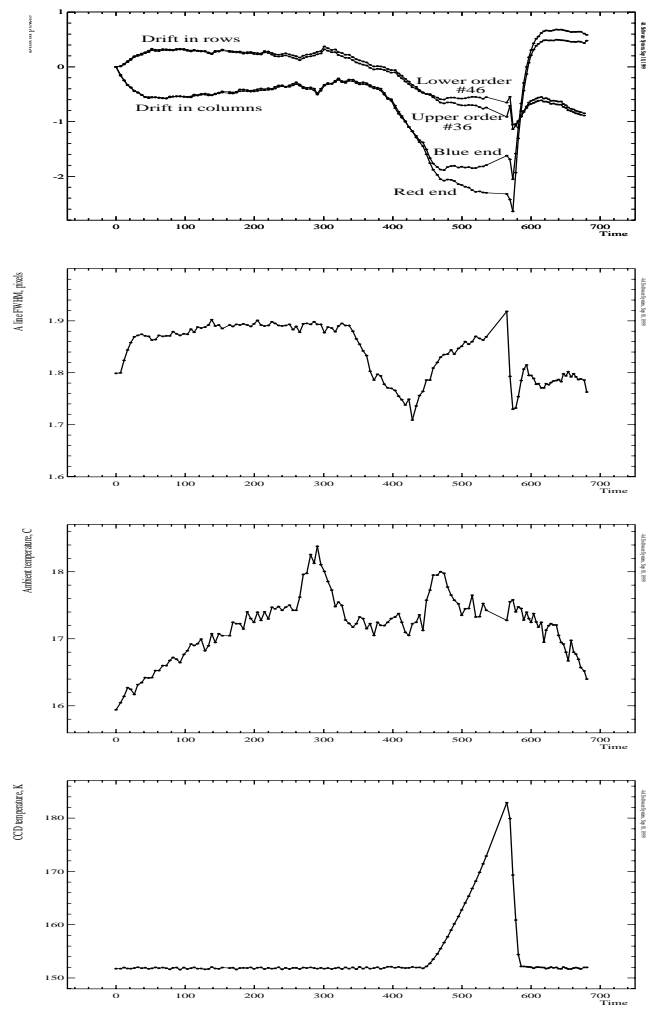


Figure 1.19: The stability test of the spectrograph in stand-by position. The horizontal axis is time in minutes. The panels from top to bottom are the image drift in CCD rows and columns, line FWHM, the ambient temperature in C, and the CCD temperature in K.

Chapter 2

The instrumental profile

2.1 The instrumental profile

The instrumental profile of a spectrograph defines its resolving power, a key parameter which determines the ability of the spectrograph to resolve narrow spectral lines. The resolving power is measured from the core of the profile, and its extended wings define the amount of scattered light of the spectrograph. This is another important parameter which can tell us how much the apparent line intensities differ from the true values and, therefore, defines the precision with which e.g. the equivalent widths of the lines can be measured.

2.1.1 Obtaining the instrumental profile

Following the prescriptions of Tull et al. (1995), Diego et al. (1995) and Barlow et al. (1995), the instrumental profile of SOFIN was measured in November 1998 for the 1st and the 2nd optical cameras. A HeNe laser was used as a source installed in front of the entrance slit. A small milk glass diffuser of the appropriate size was installed between the slit and the laser to ensure that the convergence of the entrance beam is $f/11$ and, therefore, the camera is uniformly illuminated. The spectral settings of the two cameras were adjusted so that the 6328 Å laser line appears close to the centre of the CCD image. The best focus was found prior to the series of exposures. The exposure times for the two cameras were set differently (10 s and 1 s, respectively) to achieve 25 000–30 000 ADUs per pixel at the maximum of the HeNe line profile (the dynamical range of the CCD is 65535 ADUs). A series of 200 exposures was carried out for the 1st and 2nd cameras giving a total signal-to-noise ratio at the line maximum of 10 000 and 5 500, respectively.

A similar measurement of the instrumental profile was carried out in April 2000 for the low resolution 3rd camera. A series of 150 exposures was obtained which yields a total signal-to-noise ratio of 3500.

A CCD bias column, averaged from the overscan in columns, was obtained and subtracted from every image separately to ensure that bias variations would not introduce any systematics. The photon noise is estimated from the Poisson statistics for the known CCD gain factor. A standard unweighted integration across the order was done to obtain the spectra of the line. The series of exposures took from 1 to 2 hours, therefore, a change of the ambient temperature and the CCD dewar weight due to liquid nitrogen evaporation could shift the line position. To eliminate the effect, the spectra were cross-correlated with respect to the first profile and the apparent shift in pixels was removed from each spectrum. The image in Fig. 2.1 shows a sum of all debiased individual images of the 1st camera, co-aligned in the dispersion direction.

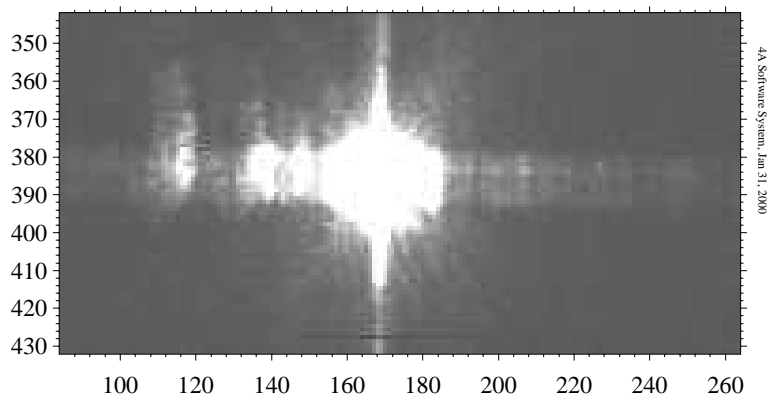


Figure 2.1: An image of the HeNe 6328 Å line obtained with the 1st camera. The image is a sum of 200 individual exposures co-aligned with each other.

We found that the immediate summation of all spectra results in an apparent increase of the core width of the resulting profile. The effect is well understood taking into account that due to the line drift and only a few pixels present in the line core, the undersampling of the core is severe, i.e. cannot be well described with the large pixel size. The increase of the line width will otherwise lead to the underestimation of the resolving power of the spectrograph. Therefore, we used the change of the line position in order to improve the sampling of the profile as follows.

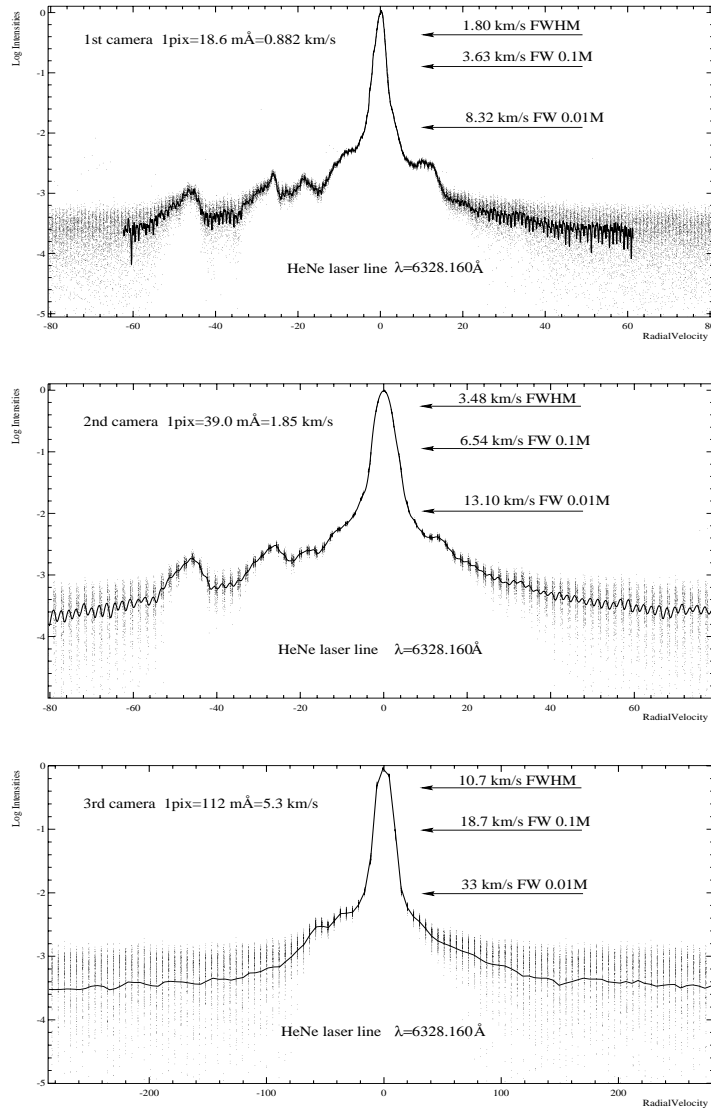


Figure 2.2: The instrumental profiles for the three optical cameras. The dots show the overlaid pixels of individual spectra coaligned to each other due to the line drift during the run of exposures. A spline fit is shown as a thin line for the camera 1 and 2. A jagged thin line in the camera 3 plot is the sum of individual spectra. The widths at the three intensity levels are indicated with arrows.

In order to exclude the effect of changes of the line intensity during the run due to variations of the exposure time and laser instability, the spectra were rescaled to the first spectrum. The linear scaling coefficients are determined by the cross-correlation method at the maximum of the cross-correlation function. The wavelength calibration was established from a ThAr comparison spectrum, the image of which was obtained before the series. The wavelengths of the spectra were transformed into radial velocities with respect to the line centre at 6328.160\AA . The spectra overlaid (interleaved) with each other in radial velocities show the structure of the profile at a number of pixels which were drifted over the time span of the run. The resulting profile was obtained by fitting a smoothing spline to the pixels obtained as a weighted average over a small interval in velocity scale (about 25 m s^{-1}).

The result of such a procedure is shown in Fig. 2.2 for the 1st and the 2nd cameras. In the case of camera 1, the overall line drift during the run is almost one pixel which resulted in the complete overlapping of the pixels. In the case of camera 2, the overall line drift was essentially smaller but well enough for the spline approximation. Unfortunately (for this application), the relative stability of the short camera is a few times higher than that of the other two. The corresponding pixels of the line profile were fixed to almost the same position during the run, giving no possibility to improve the sampling interval. Therefore, a sum of the cross-correlated spectra with small drifts corrected was calculated with the subsequent wavelength and radial velocity transformations.

2.1.2 The measurement of the resolving power

The resolving power definition involves the measurement of the line width. The line width for the 1st and 2nd camera was measured directly from the well-sampled profile. For the undersampled 3rd camera spectrum, the FWHM was measured from the weighted fit of a Gaussian to the core of the profile. Since only a few pixels are present in the core, the narrowest Gaussian was selected among all possible combinations of the pixels involved in the fit. The minimal number of pixels used for the fit is 4. This procedure is justified, because the very central part of the profile can be described by a Gaussian shape, as discussed later. In this section we assume, in the first approximation, that the internal line width of the HeNe laser line is negligible.

For the high resolution 1st camera, according to the model, the expected resolving power at this wavelength is $R = 168\,000$ ($R = \lambda/\Delta\lambda = c/v$) per resolution element of 2 pixels FWHM on the CCD. The measured width of the HeNe line is 1.80 km s^{-1} FWHM (2.04 pixels), which gives $R = 167\,000$. The 2nd camera profile yields a line width of 3.48 km s^{-1} FWHM (1.88 pixels) which results in $R = 86\,200$. The resolving power according to the model is $R = 81\,000$ for the 2 pixels FWHM resolution element. The width obtained with the low resolution 3rd camera is

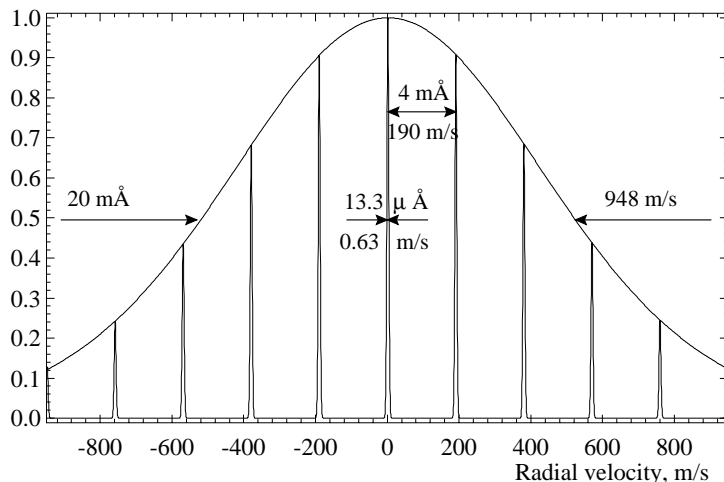


Figure 2.3: A schematic diagram of the fine structure of the HeNe laser 6328.16 Å line which was used for the instrumental profile calibration. The Doppler profile width is 1500 MHz ($T = 400$ K), the resonance mode spacing is 300 MHz (50 cm cavity length), and the single mode width is 1 MHz (this width is exaggerated 10 times for clarity). The width of the picture corresponds to two pixels ($2 \times 882 \text{ m s}^{-1}$) of the high resolution 1st camera.

10.7 km s^{-1} FWHM (2.02 pixels) and corresponds to $R = 28\,000$, which is close to the expected value $R = 28\,000$ for 2 pixels.

2.1.3 The natural width of the HeNe laser 6328 Å line

The natural width of the HeNe 6328 Å is assumed to be negligible for medium resolutions. According to Bloom (1966), the Doppler width of the line is at most 1.7 GHz, Melles Griot (1988) uses a typical value of 1.4 GHz (18.7 mÅ or 886 m s^{-1})¹. This value agrees with the direct measurements of Tull (1972) obtained with an échelle spectrograph and scanner (they used a $R = 60\,000$ spectrograph). On the other hand, Barlow et al. (1995) refer to a width of 0.03 mÅ or 1.4 m s^{-1} . Their measurements of the instrumental profile with the Ultra High Resolution Facility (UHRF) at AAT ($R = 10^6$) yields a core width of 300 m s^{-1} which implies that the natural width of their laser is indeed very small.

¹For the frequency interval transformation, we use the differential equality $\Delta\lambda = \lambda^2 c^{-1} \Delta\nu$ which follows from $\lambda\nu = c$.

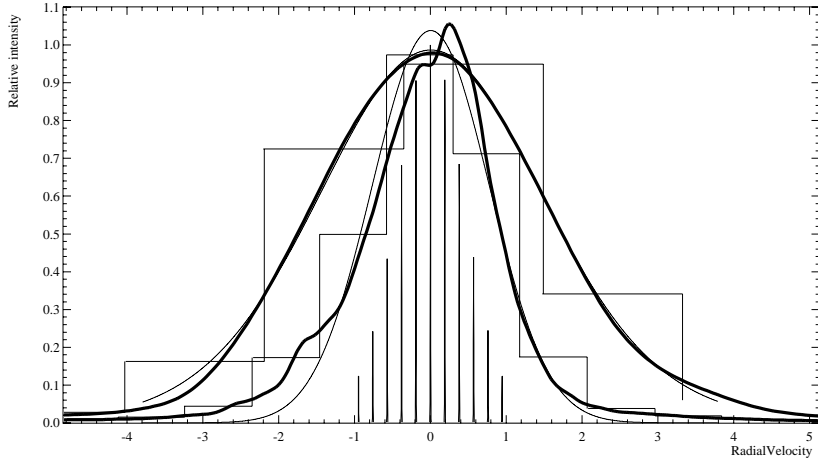


Figure 2.4: Shown in the middle is the comb of the HeNe laser line fine structure, its convolutions with a Gaussian profile (thin curves), where the narrow profile is for camera 1, the wider is for camera 2, the measured profiles approximated by a spline (thick curves), and the step functions which are the undersampled profiles calculated as the sum of the individual spectra (given for comparison).

To clarify the question of the true shape of the HeNe laser line, we refer to excellent introductions by Siegman (1971) and Svelto & Hanna (1989), some details are also given in Gray (1992, Ch.12). Fig. 2.3 shows the fine structure of the HeNe 6328.16 Å line, which consists of a number of single modes superimposed on a Doppler broadened profile. The width of a single mode is defined by the internal width of an atomic transition and is typically 1 MHz FWHM ($13.3 \mu\text{Å}$) for a HeNe laser. The mode spacing, or cavity resonance function, is defined by $\Delta\nu = c/2L$ and is caused by the multiple passing of the light packet between the two cavity mirrors of the laser, the distance between them is denoted by L . The shorter the cavity, the less modes are present (a laser with a very short cavity, $L < 15$ cm, operates in a single mode). In our case, $L \approx 50$ cm which implies that the spacing is about 300 MHz or 4 mÅ . The intensities of the resonance modes are distributed with a thermal Doppler broadening function (a Gaussian profile), which depends on the gas temperature and its atomic number. For Ne ($m=20$) at 6328 Å and for the gas temperature $T = 400$ K, a width of 1500 MHz or 20 mÅ FWHM for the thermal profile is obtained. All unstabilized HeNe lasers are subject to mode sweeping, an effect caused by thermal changes of the cavity length. The most important thing is, that it is a long term effect as the cavity length changes with the ambient temperature which may result in variations of the mode spacing and their frequencies.

The described structure of the HeNe line would now explain the fact that the natural width is laser specific. For such a measurement when the natural width is comparable with the spectrograph resolution, a laser with a short cavity working in a single mode would be required.

Now, when we established the model of the line structure, we obtained the possibility to exclude it from the measurements by deconvolution of the laser comb. Instead, we convolve the laser profile with Gaussians of different widths and compare it with the measurements. Here, we have to assume that the convolution function has a Gaussian shape, resulting from the geometrical slit width, diffraction, and aberrations. The convolutions of the laser comb with Gaussians of 1.7 pixels FWHM for the two cameras are shown in Fig. 2.4. The corresponding widths in velocities are 1.5 and 3.2 km s^{-1} which yield a higher resolving power of $R = 200\,000$ and 93 000 for the pure Gaussian shape assumption for the 1st and 2nd cameras, respectively.

2.1.4 The features

The core of the instrumental profile of SOFIN can be approximated by a Gaussian profile. Fig. 2.5 shows the degree of deviation of the core from a Gaussian. Comparison with the profile of the 2nd and 3rd cameras shows a similar behaviour. Down to the level of 10% of the central intensity the Gaussian is a good approximation to the instrumental profile, but at the level, where the Gaussian reaches 1% of the central intensity, the instrumental profile still has about 3–4% intensity.

The extended wings of the profile constitute the amount of scattered light added to the spectrum in the dispersion direction. For the 2nd camera profile, for instance, the contribution is about 0.1% of the central intensity at 30 km s^{-1} (0.6 Å) from the line centre. Examination of the original image shows that there is no difference in the amount of scattered light along and across the dispersion around the central peak. The scattered light across the spectral orders can be approximated within the interorder gaps and removed from the image. This is not the case for the scattering in the dispersion direction, as was discussed in Gray (1992, Ch.12).

The scattered light intensity differs by a factor of 2 for the two cameras (the ratio of their focal lengths) over the whole range of $\pm 100 \text{ km s}^{-1}$ as could be seen from the ratio of the two profiles. Griffin (1969) pointed out by using a log-log plot that the wings exhibit an inverse-square decline. The fit of a Lorentzian profile to the extended wings shows that the shape of the whole profile (except the satellites) can be well approximated by the sum of the two (but not with a Voigt profile which involves the convolution of the two). The FWHM of the Lorentzian profile is two times less than the FWHM of the Gaussian which fits the core. For the accurate convolution or deconvolution of the spectral lines, the instrumental profile should be used with the scattered light (far wings) subtracted from it. In practice, however, it is nearly impossible to distinguish between the scattered light and true

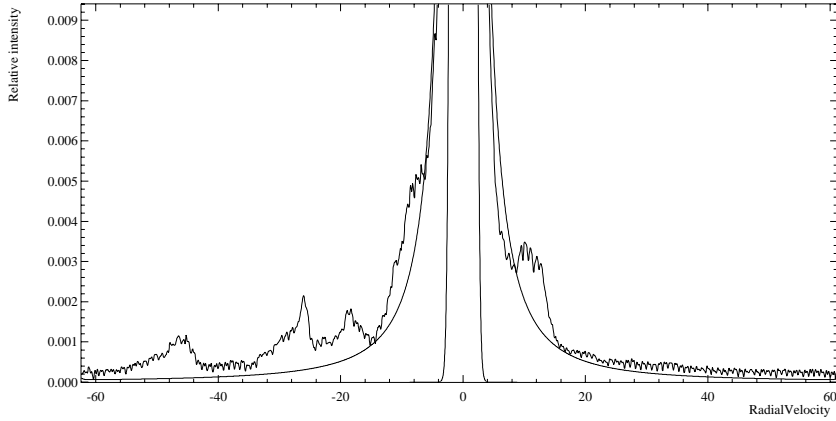


Figure 2.5: Comparison of the instrumental profile for the 1st camera with the best fit of a Gaussian profile (1.90 km s^{-1} FWHM) to the line core and a Lorentzian profile (0.95 km s^{-1} FWHM) to the extended wings.

features of the instrumental profile. Fortunately, for SOFIN, the scattered light contribution is so low, that it can be neglected.

Griffin (1969) distinguishes the following components of the instrumental profile:

1. The main peak (has been discussed above).
2. Rowland ghosts. This feature should be symmetrical with respect to the main peak. Most likely, they are absent in the observed profiles.
3. Diffracted wings. The diffraction maxima are unresolved in our case: the position of the first minimum is at 0.4 km s^{-1} , i.e. within one resolution element. The maximum $N = 30$ at 12 km s^{-1} has only 0.01% of the central intensity.
4. Small-angle scattering in the optical system.
5. Halation and scattering in the photographic emulsion (not present here).
6. True scattered light. Has been attributed above to the broad scattering wings.

Tull et al. (1995) add a number of new items:

7. Internal reflections and interference in the CCD. The two instrumental profiles were obtained by using two different CCDs (but of the same type). The

structure of the wings obtained is much the same, so that this component can be neglected.

8. Widening due to CCD transparency; the same argument as in the previous item.
9. Charge transfer inefficiency, which makes a characteristic tail in the direction of parallel (along the dispersion) or serial transfers (depending on which of these two registers is not fully optimized). The CCDs being used are optimized and specially tested for the effect.
10. External reflections (stray light images). This is the most plausible explanation for the satellites in the scattering wings. The equal positions of the satellites for the two cameras imply that the effect is taking place before entering the elements of the optical camera. Filling the collimator pupil would make external reflections on the collimator and échelle frames. Small-angle back-reflections on the optical elements are also possible. One of the features of SOFIN is a small flat mirror situated in the collimated beam. The mirror is a key element of the spectrograph design: it turns the light beam emerging from the slit by a right angle and renders it to the collimator; the use of the mirror reduces the size of the spectrograph and, therefore, improves its mechanical stability. However, the design has its drawback: the mirror is situated in the collimated beam which allows small-angle reflections back to the rear of the slit which results in the appearance of additional off-axis beams. The reflections which occur in the direction of the slit width will be seen as the displaced features in the dispersion direction, i.e. the satellites in the instrumental profile. The rear of the slit is protected from the back-illumination effect by a black metal shield with a hole, although, the size of the outlet leaves room for the small-angle back reflections. One other possibility for back-reflections in SOFIN is a filter installed between the slit and the flat mirror. The filter is composed of two pieces separated by a spacer: an “ideal” optical element to generate off-axis beams.

It has been a long discussion in the literature (e.g. Griffin 1969), that the instrumental profile obtained in the laboratory may differ from that obtained on the telescope. This important issue depends on the design of the spectrograph. Typically, the way how the collimator is illuminated is different for the calibration source and for the stellar image. In the former case, the collimator is uniformly illuminated, in the latter case, a central shadow area is present due to the secondary mirror of the telescope, hence, a difference in the shape of the profile may be expected, as well as a possible systematic shift in the line positions from the two sources. In the case of SOFIN, the diagonal flat mirror reduces the effect: the secondary mirror of the NOT is 20% of the primary in diameter, the flat mirror is 25% of the collimator. Therefore, the shadow from the telescope mirror is completely inside the shadow due to the flat mirror and one should not expect

any geometrical difference in the collimator illumination from the calibration and stellar sources. A non-uniform illumination of the collimator by the stellar source, which is also subject to temporal variations as opposed to the uniform illumination by the calibration source, causes the difference between the instrumental profiles obtained in the two cases.

2.1.5 Comparison with the solar spectrum

In this section we apply the measured instrumental profile to real observations. The solar spectrum is used and compared with the McMath FTS Solar Atlas (Kurucz et al. 1984), which has a resolving power of about 400 000 and a noise level below 0.1%. Another advantage is that the solar spectrum obtained with FTS is free of most instrumental effects, like the scattered light, and it is more accurate unlike a synthetic spectrum which may contain uncertainties in the line parameters.

The solar spectra of day light were obtained with the 1st and 2nd optical cameras in July 1996 in the spectral region around 5620 Å. The telescope was pointed without tracking to the sky with the dome and mirror opened. Pointing to the sky ensures that the collimator illumination is similar to the calibration or laser source. The exposure times were 15 and 8 min, yielding the signal-to-noise ratios 400 and 500 for the 1st and 2nd camera, respectively. The spectrum with the 3rd camera was obtained in similar conditions in June 1997 with the signal-to-noise ratio 260 in 8 min of exposure time.

A standard data reduction procedure was applied to the spectra including scattered light removal and wavelength calibration. No corrections to the wavelength scale other than the heliocentric correction were applied. The solar FTS spectrum was convolved with the measured instrumental profiles of the 1st, 2nd, and 3rd cameras in radial velocity scale. The continuum was derived by fitting a spline to the ratio of the observed spectra and the convolved FTS spectra.

The two spectra for the 1st camera are shown in Fig. 2.6: an excellent agreement with the two spectrographs at different line depths and consistency with the instrumental profile derived two years later. The difference between two spectra shows a scatter of 0.4% rms (depends on how many lines are present in the spectrum) which is higher than noise level of 0.25% due to photon statistics. The largest systematic deviations in the blue part of the spectrum occur possibly because of some small uncertainties in the wavelength scale. The comparison of the instrumental profile with a Gaussian in the previous sections shows that there is a systematic deviation at levels below 10% of the peak intensity. To check how significant the deviation is, we convolved the FTS spectrum with a number of Gaussians of different widths. For a convolution with 2 pixels FWHM all line profiles are 5% deeper than the observed spectrum. The best fit can be achieved with 4 pixels FWHM as far as the line depth is concerned, although the convolved line widths are then 10%

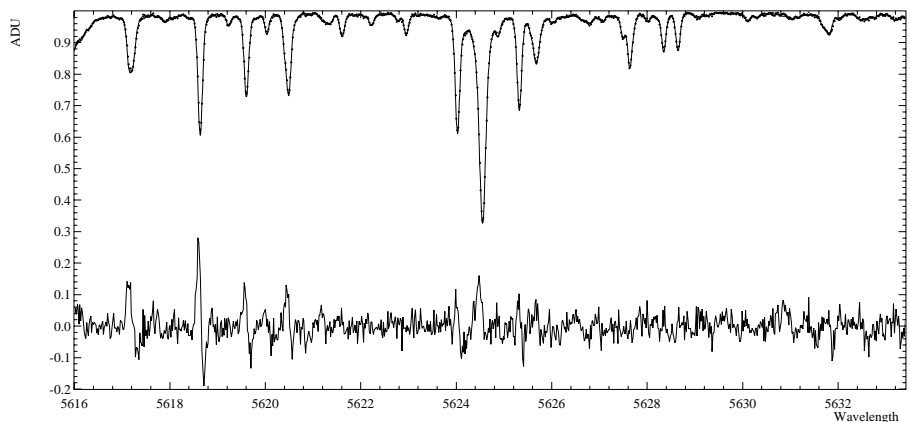


Figure 2.6: Comparison between the solar spectrum obtained with the 1st camera (dots) and the FTS spectrum convolved with the HeNe instrumental profile (thin line). The difference spectrum enlarged 10 times is plotted at the bottom. The mean difference is 0.4% rms, the maximal deviation is 2.8%.

larger than in the observed spectrum. Hence, it can be inferred that the profile wings below 0.1 are important and one should expect systematic deviations when using a pure Gaussian profile for the convolution with the synthetic data.

In the case of the 2nd camera, the observed spectrum is in best agreement with the convolved FTS spectrum (Fig. 2.7). The noise level in the difference spectrum 0.3% rms is almost completely due to the statistical noise level of 0.2%. However, a contribution to the excess could possibly be due to the fine structure of HeNe laser line present in the instrumental profile.

The comparison between the convolved FTS spectrum and the observed one with the camera 3 is given in Fig. 2.8. The convolved spectrum shows small, but systematic deviations of the line widths and depths from the observations: the lines are more narrow and shallow than in the observed spectrum, especially at the edges of the image.

2.1.6 The real resolving power

The above comparison with the observed spectra proves that the measured instrumental profile almost corresponds to the real profile. The core of the profile is broader due to the fine structure of the HeNe line but the near and far scattering wings are introducing a real effect when convolved with the FTS spectrum. The resolving power was measured from the deconvolved core of the profile and is in

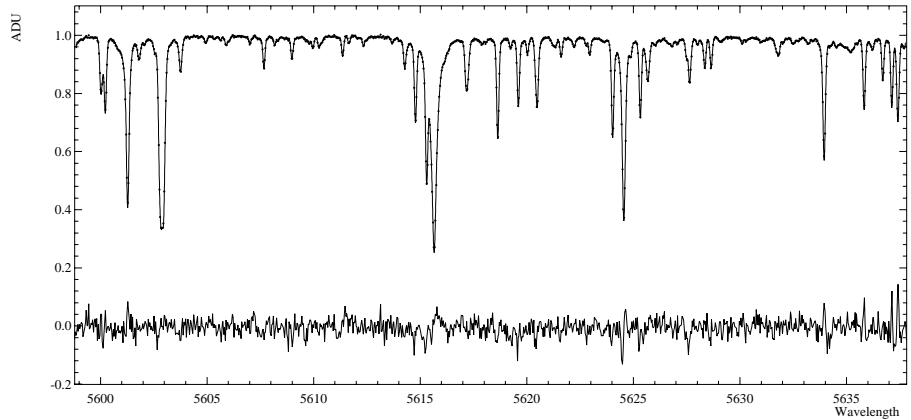


Figure 2.7: The solar FTS spectrum is convolved with the instrumental profile of the 2nd camera (thin line) and overplotted with the observed spectrum (dots). The difference spectrum enlarged 10 times is plotted at the bottom. The mean difference is 0.3% rms, the maximal deviation is 1.3%.

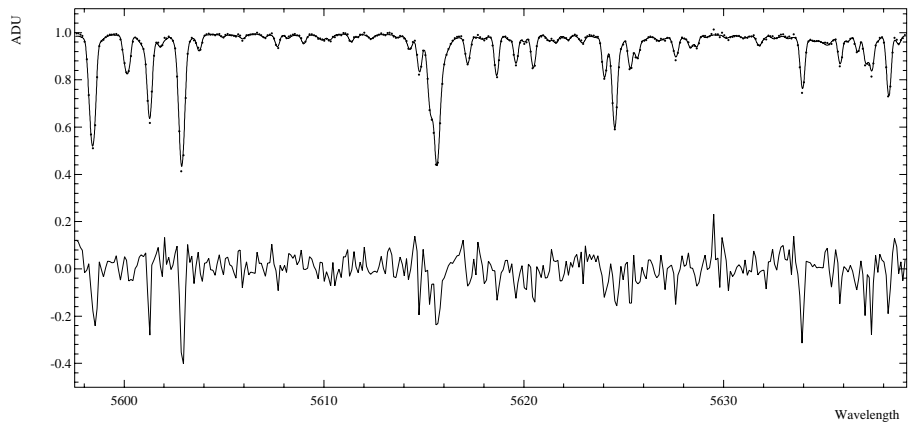


Figure 2.8: The solar spectrum observed with the 3rd camera (dots) and the FTS spectrum convolved with the HeNe laser instrumental profile. The difference spectrum enlarged 10 times is plotted at the bottom. The mean difference is 0.7% rms, the maximal deviation is 4%.

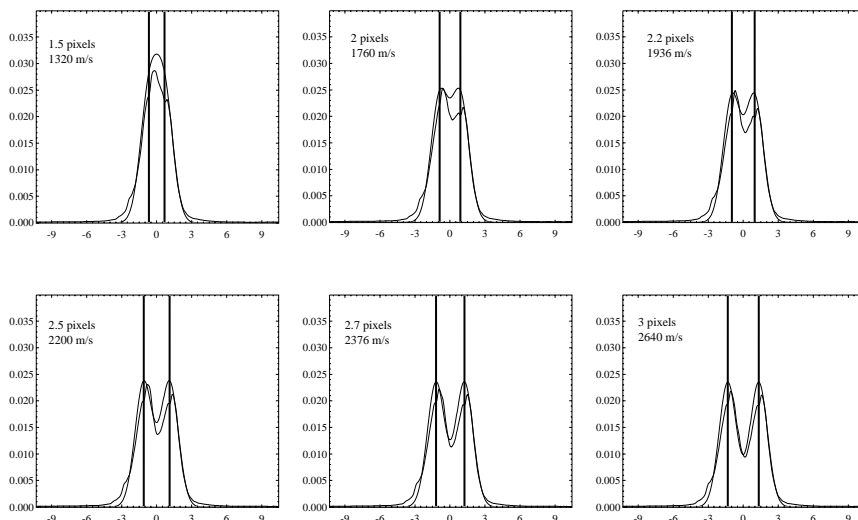


Figure 2.9: The convolution of two delta-functions of different separations with a Gaussian and with the instrumental profile of the 1st camera. The width of the convolved Gaussian profile is 2 pixels FWHM. The 1st camera instrumental profile is able to resolve two sharp features separated by less than 2 pixels (1.8 km s^{-1}) which corresponds to the resolving power better than $R = 167\,000$. The asymmetry and shift of the convolved instrumental profile with respect to the Gaussian is apparent; this could lead to a systematical error in radial velocities.

a good agreement with the expected values. A matter of practical considerations, is whether the real profile with its features is able to resolve narrow spectral lines and what is the real resolving power.

Two delta-functions were created in velocity scale with different separations to mimic narrow spectral features (Fig. 2.9). A convolution with a Gaussian profile of 2 pixels FWHM is given for comparison. The resolution can be defined as the minimal distance between two narrow features at which the convolved profile can be still numerically separated. The numerical separation involves either decomposition of the two profiles or deconvolution with the known instrumental function. The visual separation tells us that the convolved profile is still resolved at 2 pixels separation of the delta-functions.

One other test for the resolving power involves observation of interstellar clouds towards α Cyg (this spectrum was also used in Sec. 1.6.1 to demonstrate the effect of line broadening due to mechanical flexure). The spectrum of interstellar Na I D₂ at 5889.9512 \AA was taken with the 1st camera ($R = 176\,000$ at this spectral region)

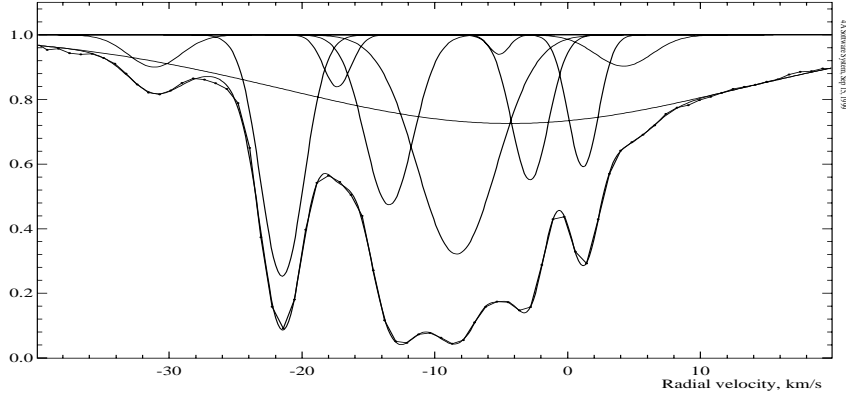


Figure 2.10: The spectrum of α Cyg ($V=1.25$ A2 Iae) taken with the 1st camera ($R=176\,000$ at this spectral region) showing the profile of interstellar NaI D₂ at 5889.9512 \AA . The profile is decomposed into 10 Gaussians. The line at -31 km s^{-1} with $\text{FWHM}=4.6\text{ km s}^{-1}$ is a telluric line.

and is shown in Fig. 2.10. The profile was decomposed into 10 Gaussians ($\chi^2_\nu = 7.7$) and compared with observations of Wayte et al. (1978) and Blades et al. (1980), made with a Michelson interferometer ($R = 500\,000$). They have resolved a hyperfine structure of the interstellar profile on the line of sight in a number of narrow $\approx 1\text{ km s}^{-1}$ components. The component at $+1\text{ km s}^{-1}$ is a blend of two narrow profiles separated by 1 km s^{-1} with the total width 2 km s^{-1} . Convolution with a two pixels Gaussian instrumental profile (the width is determined from the ThAr comparison spectrum lines) gives $\text{FWHM}=2.6\text{ km s}^{-1}$ which is exactly the width of the decomposed component.

2.1.7 Discussion

The above analysis has shown that the measured resolving power is consistent with that which is expected according to the design parameters. However, the estimated resolving power is higher than expected especially after the fine structure of the laser line was eliminated. The reduction of the profile width can be interpreted in different ways as follows.

Firstly, the observed line width could be narrower if the collimated beam does not fill the pupil completely, which results in only partial illumination of the optics of the spectrograph, i.e. the aberration spot becomes narrower. This problem was overcome by using a light diffuser situated at a certain distance above the slit. Secondly, there might be some uncertainty in the estimate of the aberration spot

for the optical cameras which is involved into the calculation of the slit width. And the last uncertainty may come from the slit calibration which is possibly resulting in a slit which is narrower than expected in linear scale. Nevertheless, the obtained instrumental profile is legitimate for the CCD image centre and for the optimal focus of the spectrograph.

The measured instrumental profiles show the typical shape common to all grating spectrographs (Dravins 1993). The core of the profiles can be approximated by a Gaussian down to 10% of its maximal intensity. Different kinds of estimations of the convolution width based on the sum of squares of widths remain valid up to the above accuracy. For higher accuracies, the real measured instrumental profile should be used for the convolution with the template (synthetic) spectrum to achieve the maximal correspondence to the observed spectrum. One should not use a Gaussian approximation of the PSF for the convolution.

Chapter 3

Optimization of CCD performance

3.1 Introduction

In this chapter we will consider some results of the practical work with the CCDs which were obtained during years of work with the Astromed CCD cameras used with SOFIN. In the first two sections, some prescriptions concerning the accurate flat fielding are given. Some preliminary results concerning the non-linearity effects as consequences of the charge transfer inefficiency are given in the following section. We proceed by describing a variant of the photon transfer technique which we employed to estimate the gain of the CCD system, and also to correct for the effects of non-linearity. Once the method has been developed and implemented, we managed to optimize the CCDs and make them linear, therefore, the method remains unused until future projects. Some general details about the mask method used for the optimization are given in the last section of the chapter.

3.2 Noise of the ideal CCD

The registered signal in a single CCD pixel can be expressed according to the following simplified model:

$$x_i = ys_i + b, \tag{3.1}$$

where y is the spatially uniform illumination level of the CCD in photoelectrons, x_i is the random number of photoelectrons registered in pixel number i . The function

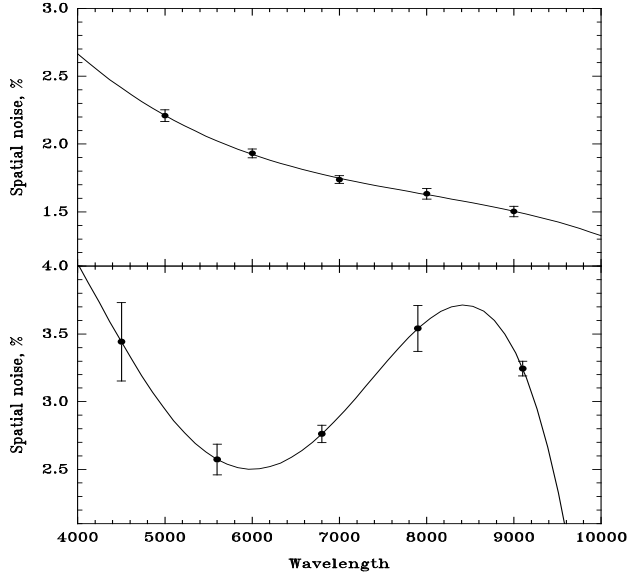


Figure 3.1: The behaviour of the high frequency pixel-to-adjacent-pixels spatial noise as a function of wavelength for two different CCDs. The upper panel shows the behaviour for the EEV P8600 576×385 CCD, and the lower panel is for the 580×520 virtual phase Electron Corp. CCD (from Shcherbakov et al. 1995) Note, that for the EEV CCDs, the pixel inhomogeneities are rather higher in the blue than in the red.

s_i describes the relative sensitivity of individual pixels and is often referred to as the high frequency spatial noise, pixel-to-adjacent-pixel noise, or fixed pattern noise of the CCD. The function is described by the mean $s = 1$ and its variance σ_s^2 . The amplitude of this noise σ_s is typically 1–6% and is constant for a given CCD across the chip. The amplitude varies from one CCD to another depending on its type and optimization quality. This noise is also wavelength dependent (see Fig. 3.1). The random number b describes the additive component to the signal and is associated with the electronic bias subtracted from the raw image, hence, its mean $b = 0$, and $\sigma_b^2 = \sigma_{\text{ron}}^2$ is the readout noise of the CCD in photoelectrons (e^-).

The total noise of the registered signal over a large sample of the CCD image is estimated using error propagation:

$$\sigma_x^2 = \sigma_y^2 s^2 + y^2 \sigma_s^2 + \sigma_{\text{ron}}^2, \quad (3.2)$$

which after division by y^2 yields the total relative noise of the registered signal:

$$\delta_x^2 = \delta_y^2 s^2 + \sigma_s^2 + \frac{\sigma_{\text{ron}}^2}{y^2} = \frac{1}{y} + \sigma_s^2 + \frac{\sigma_{\text{ron}}^2}{y^2}, \quad (3.3)$$

where in the first term the noise distribution of y is assumed to be Poissonian and the mean of $s^2 = 1$. Fig. 3.2 demonstrates the contributions of the three components to the total relative noise.

At the first crossing point $y = \sigma_{\text{ron}}^2$, the contributions of the readout noise and photon noise are equal (but dominating over the spatial noise) and limit the detectability of a very low signal with the CCD below this level. At the middle crossing point $y = \sigma_{\text{ron}}^2/\sigma_s$, the contributions from the additive and multiplicative noise components are equal, but the photon noise is dominating. The last crossing point is at $y = 1/\sigma_s^2$ where the readout noise has become negligible, but the accuracy of the measured signal is determined merely by the spatial noise. Hence, the final accuracy of the measured signal is based on the quality of the spatial noise correction. Some special pre-requirements for the flat fielding procedure are discussed in the next section.

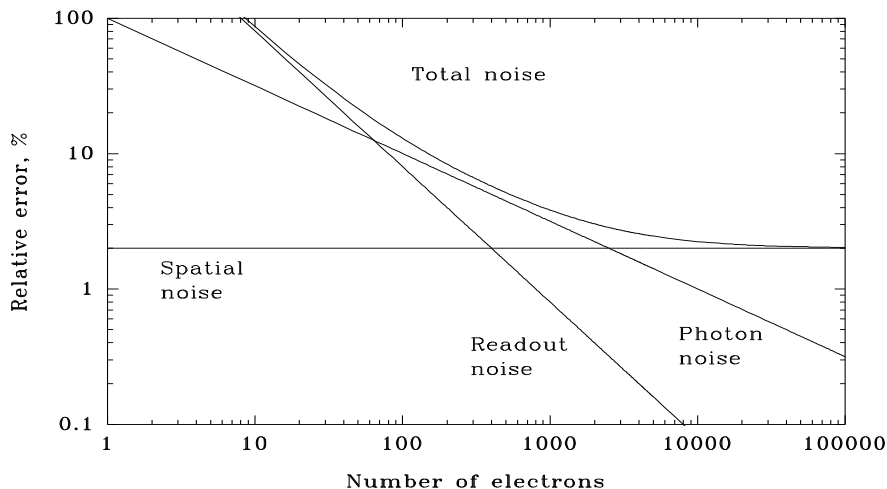


Figure 3.2: The three basic components of the total noise of the CCD. The amplitude of the spatial noise is set to $\sigma_s = 2\%$ and the readout noise to $\sigma_{\text{ron}}^2 = 8 e^-$. For the given parameters, the readout noise becomes dominant over the photon noise at light levels below $64 e^-$ while the spatial noise dominates at the levels above $2500 e^-$.

3.3 Correction for the high frequency spatial noise

The fixed pattern noise is a multiplicative component of the image structure, hence the correction is straightforward by division of the object image by an uniformly illuminated flat field image. The noise of the object image after the division may entirely depend on the noise level of the flat field image because of the statistical error of the accumulated flux: a poor flat fielding can significantly degrade the accuracy of the object image. Consider the amount of photoelectrons (e^-) accumulated in the object image y and in the flat field ny , where n is some number which implies that the flat field image is the sum of several individual exposures. The squared relative error of the ratio of two random independent variables is

$$\delta_r^2 = \delta_y^2 + \frac{1}{n} \delta_y^2, \quad (3.4)$$

where the readout noise contribution was neglected for simplicity. The following ratio of the relative errors is the accuracy reduction factor due to flat fielding and describes the achieved accuracy with respect to the one expected (which is equivalent to the ratio of the signal/noise of the two images):

$$\frac{\delta_r}{\delta_y} = \sqrt{1 + \frac{1}{n}}. \quad (3.5)$$

The following table gives for a range of flux ratios the corresponding accuracy reduction factors:

n	1	3	10	50	100
$\delta_r/\delta_y - 1, \%$	41	15	5	1	0.5

If the fluxes are equal ($n = 1$), the signal/noise degradation of the object image is $\sqrt{2}$ which is equivalent to the loss of half the exposure time. The use of 50 flat fields will degrade the resulting signal-to-noise ratio by 1% only.

To accumulate the flux ny sufficient for accurate flat-fielding, a series of flat field images of the same level can be obtained with the subsequent co-addition of all of them to form the master flat field.

The intensity level of the individual images should be, in fact, close to that of the object exposure in the case of CCD linearity problems. The amplitude of the fixed pattern may be different at high levels as compared to lower levels of the object exposure. Apparently, this can introduce spurious systematical deviations in the noise level of the corrected image. The ideal solution to the problem is to correct the image intensities with the intensity transfer function to make their response linear, and then perform the flat field division.

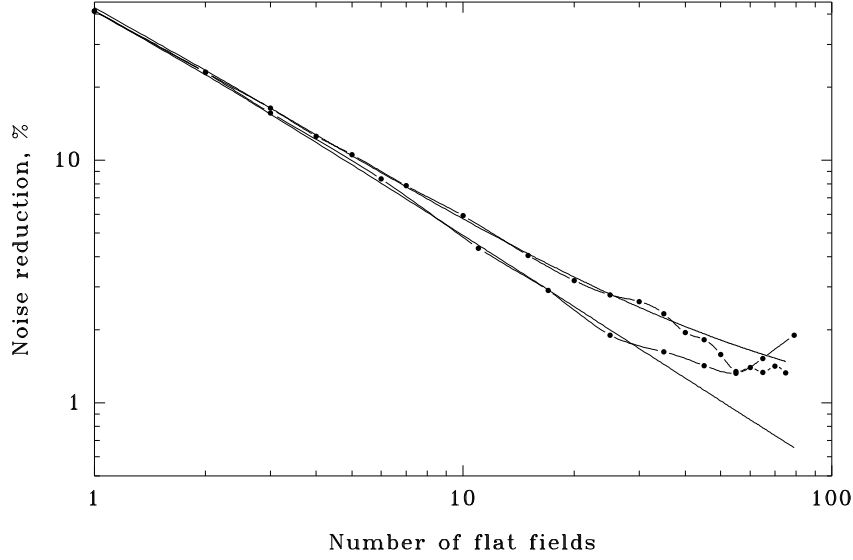


Figure 3.3: The accuracy reduction as a function of the number of co-added flat fields. Two different accumulation levels of $25000 e^-$ (the lower curve) and $130 e^-$ (the upper curve) were used. The solid curves are the expected accuracy reductions according to Eq. (3.7). The measurements were carried out in March 1996 with the P88100 CCD.

In the above equations the readout noise was neglected. Co-addition of many weak CCD images increases the noise component due to readout noise. The relative noise of the image divided by the sum of k flat fields, where the intensity of each individual image is a multiple n of the intensity of the source image, is given by:

$$\delta_r^2 = \delta_y^2 \left(1 + \frac{1}{nk} \right) + \frac{\sigma_{\text{ron}}^2}{y^2} \left(1 + \frac{1}{n^2k} \right), \quad (3.6)$$

which leads to the accuracy reduction equation:

$$\frac{\delta_r}{\delta_y} = \sqrt{\left(1 + \frac{\sigma_{\text{ron}}^2}{y} \right) + \frac{1}{n^2k} \left(n + \frac{\sigma_{\text{ron}}^2}{y} \right)}. \quad (3.7)$$

The first term reflects the readout noise component of the total noise of the source image and the second term is the contribution of the sum of the flat fields.

It is always useful to compare theory and practice. In our experiment we used the EEV P88100 1152×298 pixels CCD, uniformly illuminated by a red diode. 80 similar flat field images were obtained for two illumination levels. After the

bias subtraction, the first image was divided by the sum of the flat fields and the relative error was measured in some selected area of the corrected image. A plot of the measured and expected noise levels as a function of the number of flat fields is shown on Fig. 3.3. Unfortunately, the environmental conditions changed at the end of the experiment (the humidity in the NOT dome was about 100%) which spoiled the last images. Otherwise, this experiment shows that the accuracy reduction follows the prediction and no other additional noise sources are present.

3.4 Charge transfer efficiency

The efficiency of the charge transport during readout is measured in both directions of the parallel and the serial transfer. The basic method to calculate the overall efficiency is the so-called *extended pixel edge response* (EPER). The CCD is illuminated to get a uniform response with the subsequent readout of a number of trailing pixels which is more than the physical number of pixels in the CCD in order to obtain overscan areas in both directions. The amount of charge (the sum) spilled out of the last column/row, or equivalently, the amount of *deferred charge* is measured with respect to the bias level.

The charge transfer efficiency describes the fraction of the charge transferred from one pixel to the other:

$$\text{CTE} = 1 - \frac{d}{c \cdot n}, \quad (3.8)$$

where c is the intensity level of the uniform area in ADU (analogue-to-digital units), n is the number the CCD transfers, i.e. the number of times the charge loss was suffered in the direction of parallel or serial transfers, and d is the amount of measured deferred charge. The quantity $(1-\text{CTE})$ is called the *charge transfer inefficiency* (CTI).

The charge transfer inefficiency is one of the sources of CCD non-linearity: the charge trapped in a single pixel is accumulated until it is co-added to the next charge packet (column brightening), or in the case of a single event, it appears as a tail of the spilled charge opposite to the direction of the transfer. Since the charge is co-added to the other pixels, the ratio of the pixel intensities becomes dependent on the amount of the trapped charge as a function of the distance between pixels.

The above method of measuring CTE is the relative method. The absolute method is employed in CCD labs and uses an X-ray source with the known number of equivalent optical photoelectrons per single event (e.g. a $\text{Fe}^{55} + \text{Mn}$ source has $1620 e^-/\text{event}$). A plot of intensities versus column number shows the amount of charge lost as the number of transfers increases (e.g. Janesick 1997).

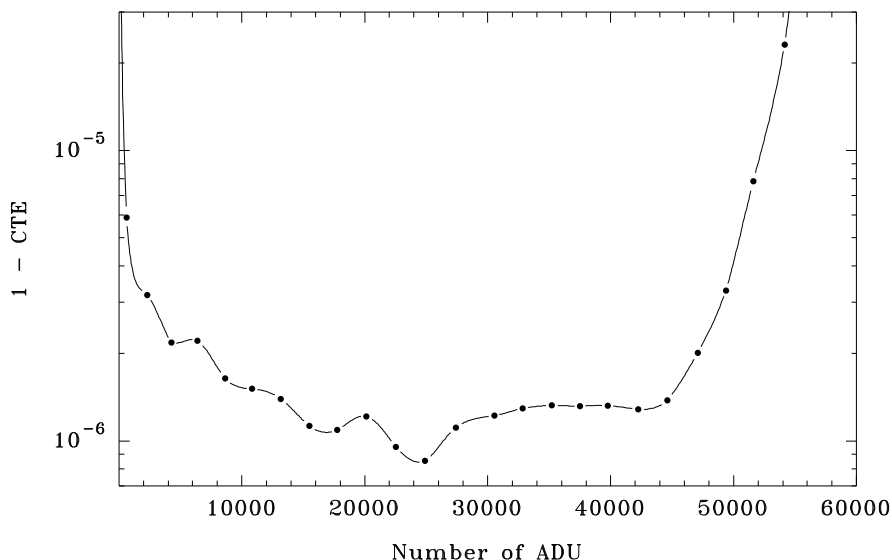


Figure 3.4: The charge transfer inefficiency 1-CTE in the direction of parallel transfer at different illumination levels of the P88100 CCD (December 1995). An average of two flat fields and 200 overscanned columns were used for the measurements.

Usually, the CTE of a CCD is characterized by a single number. We found that the CTE is not constant over a range of intensities (at least for our CCDs), and therefore cannot be expressed as a single number. In Fig. 3.4 we used the EPER technique at different flat field illumination levels. As can be seen, the minimal charge losses occur in the central part of the dynamical range. The systematical change of the CTE reflects the shape of the potential well. In principle, the structure of the well can be reconfigured with a fine tuning of the substrate bias voltage (vss). The other reason for the increase of CTI at low light levels is a too high level of the output gate voltage (VOG) which controls the height of the potential barrier when the next charge packet is transferred into the output node of the serial register (this is valid at least for the EEV CCDs). A too high level of the barrier can cause a complete blockage of the signal, and a partial trapping of the signal results in the appearance of a “fat zero” effect which also can be seen in the linearity curve (Thorne et al. 1987).

3.5 The intensity transfer function of the CCD

In this section we consider a method for correction of the CCD non-linearity effects in a qualitative way, i.e. the problem is to reconstruct the intensity transfer function

which can be used to correct the raw pixel intensities. The importance of the problem and possible ways to its solution were extensively discussed in ESO CCD-related works, the most relevant is Gosset & Magain (1993).

The method described here is an extension of the known photon transfer technique (Janesick 1997) in the sense that the measured quantities are based on the analysis of the variance of the detected signal. This is the principal difference to the absolute methods which employ X-ray sources. In the following considerations we are going to find the exact solution to the problem and, if possible, to eliminate many of the assumptions used in the photon transfer technique. However, our experience of using the method described below shows that a more complex model of the CCD signal transfer equation is needed which should include an additive component due to the charge transfer inefficiency. Nevertheless, we proceed with the simplified model similar to that already introduced.

We shall consider the CCD as a non-linear system with the signal transformation according to the model:

$$x_i = p(y)s_i + b, \quad (3.9)$$

where y is the mathematical expectation of the input signal to the system in photoelectrons and its variance is $\sigma_y^2 = y$, x_i is the signal measured in pixel i in ADUs, $p(y)$ is the unknown signal transformation function of the CCD amplifier and the digitizing circuit, s_i is the fixed pattern noise with the mean $s = 1$ and the variance σ_s^2 . The subtracted bias offset b is assumed to have the mean $b = 0$ and the variance $\sigma_b^2 = \sigma_{\text{ron}}^2$ in ADUs to be known.

Two identical exposures of the uniformly illuminated CCD yield two images which have almost the same average level but never the same due to small deviations from the average in shutter response, light source brightness, etc. The division of the two debiased images by each other yields a ratio image, which is used to obtain two quantities: the average ratio r and its variance σ_r^2 by using a large enough area of the CCD. We use the ratio of the two images (not the difference as in Janesick 1997) in order to eliminate the multiplicative fixed pattern noise. Recalling the relative error identity for the ratio of two independent random numbers, we have:

$$\frac{\sigma_r^2}{r^2} = \frac{p_1'^2 y_1 s^2 + \sigma_{\text{ron}}^2}{x_1^2} + \frac{p_2'^2 y_2 s^2 + \sigma_{\text{ron}}^2}{x_2^2}, \quad (3.10)$$

where $p_1' \equiv p'(y_1)$ and $p_2' \equiv p'(y_2)$ are the first derivatives of the unknown function $p(y)$, y_1 and y_2 are the unknown “true” numbers of photoelectrons, x_1 and x_2 are the measured average of the signal registered on the same CCD area of the two identical exposures (*not* to be confused with the signal at the pixel number 1 and 2), and the factor $s^2 = 1$ is omitted hereafter.

In order to exclude unnecessary variables, namely x_2 and y_2 , two assumptions

have to be made at this point, the first one is that

$$r = \frac{x_1}{x_2} \quad (3.11)$$

implying that the measured averages of the registered signals are not biased by the fixed pattern noise over a large sample, and the second one is that the unknown function $p(y)$ must be simple (Occam's approach is in action), i.e. within a small interval of intensities $[y_1, y_2]$ it can be approximated by a straight line:

$$x_2 - x_1 = p'(y_2 - y_1), \quad (3.12)$$

where the notation is $p' = p'_1 = p'_2$.

Applying these assumptions and after multiplication of both sides of Eq. (3.10) by x_1^2 , we get

$$\frac{\sigma_r^2}{r^2} x_1^2 = p'^2 (y_1 + r^2 y_2) + \sigma_{\text{ron}}^2 (1 + r^2) \quad (3.13)$$

and finally, after omitting the index referring to the first image of two identical exposures $x \equiv x_1$ and $y \equiv y_1$, it follows:

$$p'^2 \cdot \frac{y}{x} = \frac{\sigma_r^2 x}{r^2 (1 + r^2)} - p' \cdot \frac{r(1 - r)}{1 + r^2} - \frac{\sigma_{\text{ron}}^2}{x}, \quad (3.14)$$

which is a general form of the intensity transfer equation as a function of the number of different illumination levels measured as x .

3.5.1 The CCD gain function

Let us make a further simplification of the intensity transfer function, namely that it is

$$p(y) = \frac{y}{g(x)}, \quad (3.15)$$

i.e. the number of detected photoelectrons is $y = xg(x)$, where $g(x)$ is the gain function of the system in e^-/ADU units. This implies that $p'(y) = 1/g(x)$ and after some transformations we get the solution

$$g(x) = \frac{xr^2(1 + r)}{x^2\sigma_r^2 - \sigma_{\text{ron}}^2 r^2(1 + r^2)}. \quad (3.16)$$

The function, defined in the interval of different values of x over the dynamical range of the CCD, can be derived from the measurements of x , r , σ_r^2 , and σ_{ron}^2 obtained from a number of identical exposures. This approximation and the derived solution will be used later for the proposed “mask” method of the CCD quick characterization. Also, by neglecting the ratio term by setting $r = 1$ and for fluxes $x \gg \sigma_{\text{ron}}^2$, one will get a simple estimate of the gain factor:

$$g(x) = \frac{2}{x\sigma_r^2}. \quad (3.17)$$

3.5.2 Integration of the transfer equation

To restore the shape of the function $p(y)$ we need to integrate the differential equation Eq. (3.14). In fact, we are finally interested to restore the inverse function of $p(y)$, namely a generalization of the gain function:

$$y = xg(x) \quad (3.18)$$

which would give us the true, corrected for the non-linearity effects, number of the photoelectrons y detected from the measured number x of ADUs. Eq. (3.14) is a differential equation which is quadratic in $p'(y)$. To lower the degree and simplify the derivations, we approximate the term $p'(y)$ on the right hand side in Eq. (3.14) by a constant number $1/g_0$, which is the inverse gain of the system, Eq. (3.16). An estimate of g_0 can be obtained as a preliminary step prior to the integration. Then, the right hand side of Eq. (3.14) reads

$$f(x) = \frac{\sigma_r^2 x}{r^2(1+r^2)} - \frac{1}{g_0} \frac{r(1-r)}{1+r^2} - \frac{\sigma_{\text{ron}}^2}{x}, \quad (3.19)$$

which is a discrete function of the measurements at a number of different fluxes x . The variables are separated and integrated in parts as follows:

$$\int_0^y \frac{dy}{\sqrt{y}} = \int_0^x \frac{dx}{\sqrt{x f(x)}}, \quad (3.20)$$

where we write $p'(y) = dx/dy$. The integration can be done with the Runge-Kutta method in the case when the integration function is a smooth (and possibly an analytical) function. Here, we used two types of approximation of the integrated function depending on the complexity of its shape.

Polynomial approximation

Suppose, that the integration function can be approximated by a polynomial of degree n :

$$\frac{1}{\sqrt{f(x)}} = \sum_{k=0}^n c_k x^k; \quad (3.21)$$

after the integration it becomes

$$\sqrt{x} \sum_{k=0}^n \frac{c_k}{2k+1} x^k = \sqrt{y}. \quad (3.22)$$

Then, the unknown function is

$$g(x) = \frac{y}{x} = \left[\sum_{k=0}^n \frac{c_k}{2k+1} x^k \right]^2. \quad (3.23)$$

Smoothing spline approximation

Suppose, that the function $f^{-1/2}(x)$ cannot be well described by a polynomial but is approximated by a smoothing spline (the details of the implementation are given in Ilyin 2000). The smoothing cubic spline is defined on each interval $[x_i, x_{i+1}]$ of the data $i = 0, 1, \dots, n$, and together with its derivatives is written as follows:

$$\begin{aligned} q(p) &= a_i + b_i p + c_i p^2 + d_i p^3 & q''(p) &= 2c_i + 6d_i p \\ q'(p) &= b_i + 2c_i p + 3d_i p^2 & q'''(p) &= 6d_i, \end{aligned} \quad (3.24)$$

where

$$p = \frac{x - x_i}{h_i} \quad \text{and} \quad h_i = x_{i+1} - x_i. \quad (3.25)$$

The unknown polynomial coefficients of the cubic spline are calculated from its second derivatives y_i'' :

$$\begin{aligned} d_i &= \frac{h_i^2}{6} (y_{i+1}'' - y_i''), & c_i &= \frac{h_i^2}{2} y_i'', \\ b_i &= y_{i+1} - y_i - (d_i + c_i), & a_i &= y_i \end{aligned} \quad (3.26)$$

where the derivatives y_i'' are obtained from the solution of a system of linear equations and y_i are the *smoothed* points of the tabulated function. The integral

$$I_i(x) = \int_{x_i}^x \frac{1}{\sqrt{xf(x)}} dx \quad (3.27)$$

is defined on each interval $x \in [x_i, x_{i+1}]$. Integrating by parts, one can obtain:

$$\frac{I_i(x)}{2\sqrt{x}} = q(p) - \frac{2}{3} \left(\frac{x}{h_i} \right) q'(p) + \frac{4}{15} \left(\frac{x}{h_i} \right)^2 q''(p) - \frac{8}{105} \left(\frac{x}{h_i} \right)^3 q'''(p) \quad (3.28)$$

and the total integral $[0, x]$ consists of the sum:

$$J(x) = \int_0^x \frac{1}{\sqrt{xf(x)}} dx = \left[\sum_{i=0}^{k-1} I_i(x_{i+1}) \right] + I_k(x), \quad (3.29)$$

where the index k is chosen from the interval where $x_{k-1} \leq x < x_k$. Finally, the unknown integrated function is

$$g(x) = \frac{y}{x} = \frac{J^2(x)}{4x}. \quad (3.30)$$

3.6 The mask method

With the variation of the photon transfer technique as described above to obtain the CCD linearity curve, a series of pair exposures of different exposure times (or by changing the light source intensity) with the CCD uniformly illuminated is obtained. Each pair consists of two exposures of the same accumulated level. In practice we usually do about 10–30 pairs of exposures which, with the subsequent image processing (to obtain r and σ_r^2 for a number of selected image regions), takes an hour to obtain the linearity curve. Consequently, a faster method was invented to speed up the process and make the trial-and-error CCD optimization process efficient and practically applicable.

The proposed *mask* method is used which is less accurate but is much faster in the sense, that only two exposures are needed to obtain the linearity curve at once. The idea behind it is that the CCD is illuminated fairly non-uniformly which results in an image with a large range of accumulated ADUs. If the CCD is linear, the ratio of such two images should be approximately a constant. The noise level of the ratio gives an estimate of the gain factor as a function of ADUs (Eq. (3.16)). The ratio of two exposures at different illumination levels can reveal

possible non-linear effects of the CCD, and can be used as a merit function for the CCD optimization process.

The mask is a PostScript programmed image and printed on a transparent film with a 300 dpi PS-printer. Fig. 3.5 shows the mask and the associated code which can be found in the “PostScript Language Manual” (Adobe Systems Inc., Wesley).

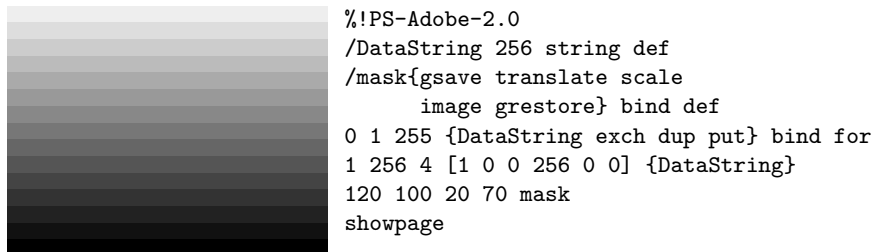


Figure 3.5: The mask (here printed with 600 dpi) used to obtain a non-uniformly illuminated CCD image and its corresponding code in PostScript. The numbers 120 100 in front of the `mask` command define the width and height of the mask and 20 70 are its lower-left position on the sheet in PostScript point units.

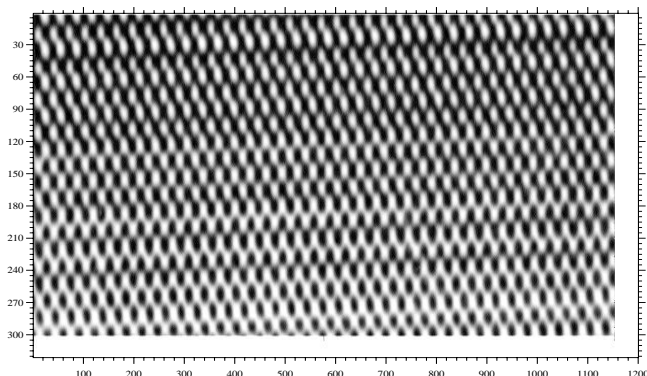


Figure 3.6: An image obtained through the mask installed in front of the CCD and uniformly illuminated by a light source. The actual CCD size is smaller than that of the mask shown in the previous figure. Thus, the fine structure results from light falling through the gaps between the dots which make up the “homogeneous” stripes in the mask. This installation was used for the P88100 CCD gain reconfiguration in October 1999. The range of pixel intensities is 10000–40000 ADUs.

The following figures show the results of the method and the success of the optimization procedure.

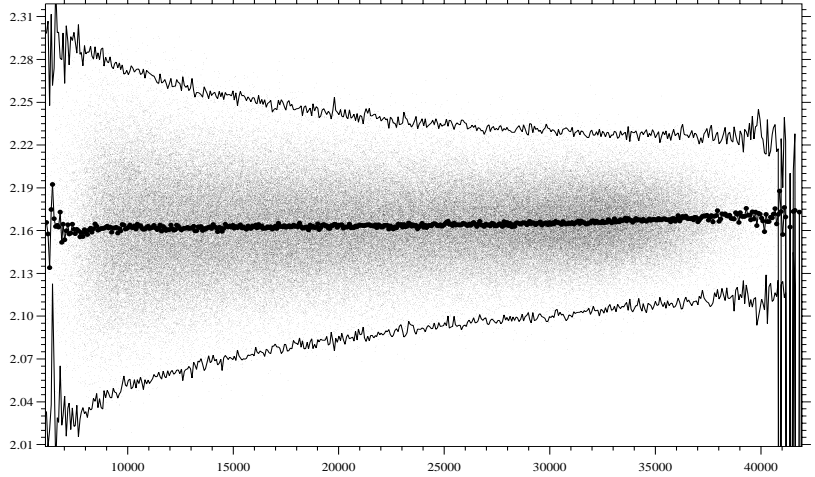


Figure 3.7: The ratio of two images taken with different fluxes versus intensity of the first image. Each point is the ratio of the intensities of the same pixels in two images. The mean and variance curves are calculated within every bin of 1/500 of the intensity range.

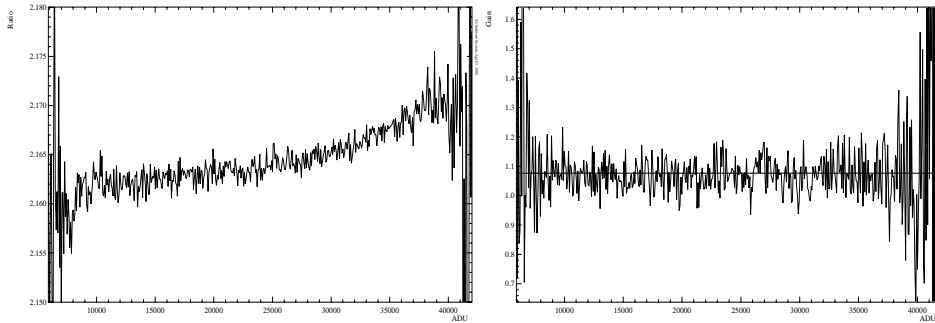


Figure 3.8: The ratio curve, enlarged from the previous figure, and the gain factor as functions of intensity. The ratio curve should be constant; it is tilted by only 0.3% within the range of intensities. Despite the tilt of the ratio, the gain factor curve is constant and the mean is $1.07 e^-/\text{ADU}$ for the reconfigured P88100 CCD camera with the adjusted parameters $\text{VOD}=14$, $\text{VRD}=3.5$, $\text{VRSPH}=-7.8$, and $\text{PGAIN}=8$.

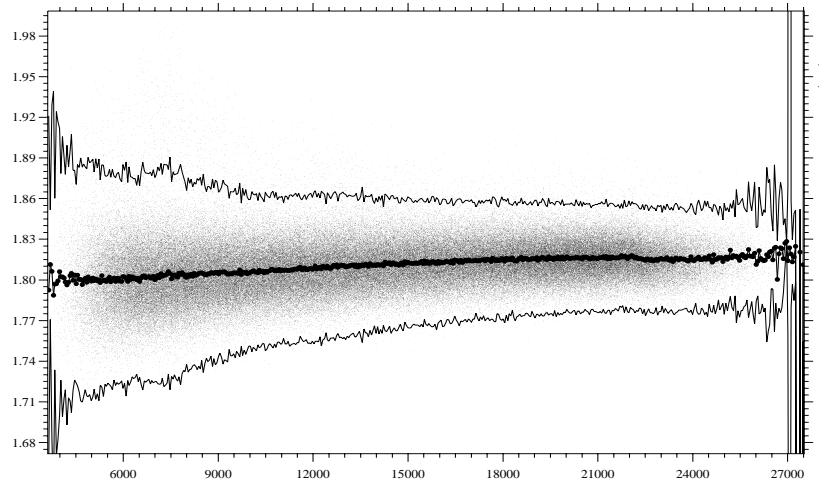


Figure 3.9: An example of the ratio plot of two CCD images with the incorrect voltage setup.

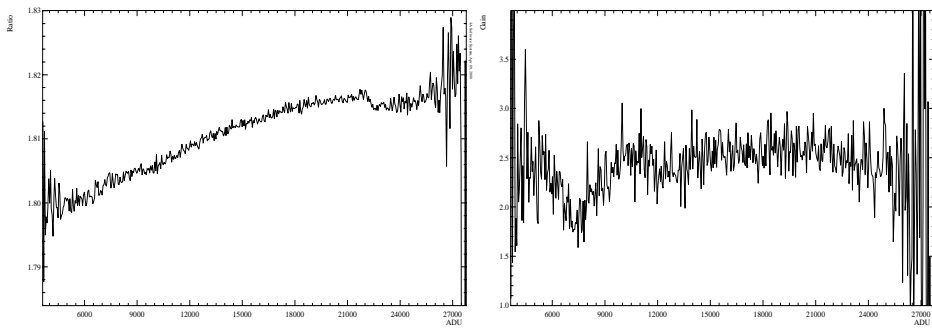


Figure 3.10: The enlarged ratio curve from the previous figure, the tilt is about 1.1%. The corresponding gain curve shows some tilt and breaks; the maximum non-linearity is about 30%. This was used as an indication that the the trial voltage parameters are wrong: $VOD=16$, $VRD=7$, $VRSPH=-3$, $PGAIN=8$.

Chapter 4

Processing astronomical spectra

4.1 The 4A software package

The Advanced Acquisition, Archiving, and Analysis (4A) software package is the main tool for providing observations with a remotely controlled spectrograph as well as the subsequent reduction and analysis of the data.

The package provides the software to control the SOFIN spectrograph and the CCDs which are used to register the échelle spectra.

The images and spectra are written as separate files stored in the FITS format, selected records of their headers constitute the contents of a database. Instead of using a command line prompt, file names, and shell scripts, like other data reduction facilities in astronomy, an interactive facility allows to operate with the data by its context as it is seen in the database. The procedures can be run interactively for a single image or spectrum for immediate evaluation of the result, or in an automatic, sequential mode for a number of images selected from the database.

The database facility allows to add new files to the database, copy or move them to another directory. New fields can be added, edited, and removed from the database. A number of mathematical operations, including time transformation routines, are incorporated to manipulate with the fields of the database, and, thus, records in the FITS headers.

One of the main features of the package is that it gives in the resulting spectra not only intensities but also errors of the intensities and pixel positions. All the routines are propagating the variances, which are ultimately based on the photon

noise statistics of the raw images.

Two groups of filters are implemented: the ranked filters with median and trimmed mean (including moving average filter), and the convolutional filters with the Gaussian, Lorentzian, and stellar rotational profiles. The approximation facility implements a weighted smoothing spline and polynomials; a clip-and-fit algorithm allows e.g. to approximate the outer envelope of the data or the interactive exclusion of intervals from the fit and facilitates reshaping the spectra e.g. during continuum normalization.

The software is written in the C language and contains about 100 000 lines of the source code (2.6 MB in total). It includes a graphical user interface, a number of mathematical routines (Ilyin 2000), the programs for the spectrograph and CCD control, data reduction and analysis facilities developed solely by the author. The total number of such programs is 140. Some standard mathematical routines were implemented from Press et al. (1992) and a number of routines for time and ephemeris transformations was coded from basic astronomical handbooks. Although the software is developed in MS-DOS, it is running in Linux and Windows-98 software emulation environments.

It is a frequently asked question why not to use other standard data reduction packages, like IRAF, MIDAS, AIPS, Figaro, or Starlink, instead of 4A. The answer is that they indeed can be used for the reduction of the SOFIN échelle spectra without any problems. But our (limited) experience with the other packages shows that 4A does it better and in a more efficient way. However, most of the procedures are common, some of them are based on rather different approaches, like the flat field correction of échelle spectra. The criterion for the efficiency is that the observer can now leave the telescope with his data completely reduced, somehow similarly to the pipeline data reduction in MIDAS and IRAF.

4.2 Reduction of CCD échelle spectra: an overview

The process of spectrum reduction involves a number of procedures to correct for the spectrograph and CCD instrumental effects and to extract the calibrated stellar spectra from the raw images. The following constitutes a short overview; a more technical description of the individual steps is given in the Appendix.

A very first step of any CCD reduction is the subtraction of the bias frame, an image obtained with a zero exposure time. If the bias is not uniform across the image but constant in time, the average of many such images is subtracted. However, if the bias is variable in time, then the overscan area of the same CCD image is used which involves the subtraction of the averaged and smoothed bias trace from the whole image.

Once the zero point of the intensity is removed and the images are trimmed at the edges, the estimation of the pixel variances is performed. The estimate of the pho-

ton noise is based on the known CCD gain factor and the amplitude of the readout noise. The variance of every pixel will then follow the intensity transformations at each and all subsequent steps of the data reduction.

The CCD pixels intrinsically have different sensitivities which vary within several percent depending on the CCD. The image of the pixel sensitivity can be obtained from the master flat field, which is made up by a sum of a large number of flat field exposures. Division of the images being processed by the master flat field can significantly reduce the apparent noise of the spectra.

Prior to the échelle order integration, the scattered light has to be subtracted from the image to ensure that the depth of the spectral lines remains undisturbed. The structure of the scattered light is usually very complex and results from the light diffusion and backwards reflections on the optical elements of the spectrograph. The background structure is difficult to describe in terms of a model, hence, an empirical approximation of the inter-order structure is used to retrieve the scattered light surface e.g. by means of a clip-and-fit smoothing spline in two dimensions.

The spectral orders of the échelle image are tilted and curved with respect to the regular grid of CCD pixels. The order definition involves recognition of the spectral orders in the image and approximation of the order positions with a bivariate polynomial.

The spectral orders are integrated at each wavelength pixel by using a weighted fit of the spatial profile to the intensity distribution of the pixels across the dispersion. Since the fit is linear, it allows to distinguish between good pixels and those which are affected by cosmic ray events. The latter are excluded from the fit. The image of the spatial profiles of the spectral orders is derived by smoothing the normalized intensities along the CCD columns in the dispersion direction.

The integrated spectra are usually curved due to the difference in illumination levels in the centre of the focal plane and in the edges. To correct for the vignetting function, flat field spectra are used which generally show the same shape in intensity. Appearance of interference fringes in the stellar spectra due to varying thickness of the CCD UV-coating film can also be accounted for with the aid of the flat field spectra.

The wavelength calibration of the stellar spectra is derived from the images of a ThAr comparison spectrum. The images are debiased, trimmed, and the variances are estimated. The background of the comparison images is obtained e.g. by a median filtration in the dispersion direction.

The bivariate polynomials of the spectral orders are used from the neighbouring object or flat field images. The position of the curves may not coincide with the centres of the spectral orders of the comparison image because of a drift between the two images. The exact position is obtained by fine tuning of the bivariate polynomial curves to the cross-dispersion profiles of the comparison spectrum image.

After integration of the spectral orders, the central positions of the lines are determined by fitting Gaussian profiles. To find the wavelengths of lines in a single order, a search algorithm is used which compares the positional configuration of the lines in the spectrum with the wavelength configuration of lines in a catalogue.

A fit of the line positions in pixels to their wavelengths defines the dispersion polynomial for a single order. The wavelength identification of the other spectral orders is done in a first approximation using the constancy of the ratio between échelle order numbers and wavelengths at a given pixel in the dispersion direction. The exact wavelength for every line of all other spectral orders is found by picking the nearest value from the catalogue of spectral lines.

Combination of hundreds of spectral lines into one fit based on the appropriate model significantly improves the accuracy of the wavelength calibration. Such a model is based on a bivariate polynomial fit of the line position in the dispersion direction as a function of wavelength and its position in cross-dispersion direction. The complexity of the model is justified by the fact that the dispersion of the spectral orders is changing non-linearly due to aberration effects in the optical cameras, misalignment of the optical elements, and centring errors due to possible asymmetry of the spectral lines. Furthermore, two subsequent comparison spectrum images exhibit a drift of the spectral line positions with respect to each other in either direction due to variations of the above factors in time as a function of the spectrograph's spatial orientation on the telescope and the ambient temperature in the dome. The model is capable to trace the temporal changes of the dispersion coefficients by inclusion of the third, the time dimension into the model, if at least two images are obtained at different times.

The pupil of the comparison spectrum is formed by uniform illumination of the slit. The pupil of the stellar image is defined by the width of the seeing profile. Any slit spectrograph is subject to the slit error which results in a small and random shift of the stellar lines with respect to the comparison spectrum lines. The amplitude of the effect depends on the relative sizes of the slit and the seeing profile, on the exposure time, and how accurately the stellar seeing image is centred onto the slit. The shift can be corrected using telluric lines which are very often present in some orders of the stellar spectra. The correction for the slit error is incorporated into the wavelength calibration model since the telluric lines obey the same dispersion relations as the comparison spectrum. A low order bivariate polynomial is added to the above 3D-polynomial and describes the deviation of the telluric line positions from the wavelength solution. A zero-order polynomial would specify a constant shift of all telluric lines with respect to the comparison lines.

Instead of rebinning the spectra into the wavelength scale, a wavelength table is added to the spectra giving the wavelength and its error for each pixel. The heliocentric wavelength correction and possible removal of the stellar radial velocity does a simple transformation of the wavelength table for every pixel. The spectra

are rebinned into the same wavelength scale when the weighted average or the sum of many spectra is calculated. The variances of the rebinned spectrum are calculated taking the variances of the pixel intensities and their wavelength errors into account.

The spectra are normalized to a continuum estimated from a synthetic or mean spectrum using a smoothing spline or polynomials. The clip-and-fit algorithm together with the interval selection feature (masking the pixels) facilitates the continuum approximation.

The cross-correlation facility is a tool to determine the position of a spectrum with respect to a template. Due to the non-linearity of the wavelength scale, the shift between two spectra can be determined in three different scales: pixels, wavelengths, and radial velocities. The weighted linear regression at each offset accounts for the variances of the spectra and their positional errors.

As a matter of fact, the cross-correlation is also used very often internally in many algorithms at different steps of the data reduction. The error of the offset is used in many instances as a weight for subsequent steps or as a significance level when the program should make a decision. Therefore, in the next section the details of the cross-correlation technique are described. In the last section of this Chapter some details of the radial velocity scale transformations are given which are related to the implementation of the cross-correlation method.

4.3 The cross-correlation offset determination

4.3.1 The cross-correlation method

Let $t(x_i)$, $i = 1, 2, \dots, N$ be a noise-free template spectrum and $p_i \equiv p(x_i)$ a programme spectrum given with the variance for each pixel σ_i^2 . The shift δ is determined as the offset at which the match between the spectra is best, i.e. the merit function is minimal:

$$\chi^2(a, b, \delta) = \sum_i \left(\frac{a + b \cdot t(x_i + \delta) - p_i}{\sigma_i} \right)^2, \quad (4.1)$$

where a and b constitute the intensity transformation of the template spectrum $t(x_i + \delta)$ to the programme spectrum p_i at the trial offset δ . The index i is ranging within the overlapping regions of the two spectra for the given δ with possible exclusion of masked features in the two spectra, which implies that the number of used pixels n is also a function of the offset δ . Since the template spectrum is given noise-free, the values of $t(x_i + \delta)$ can be interpolated for the offset equal to any fractional part of the step size. As it is seen from the model, the noisy programme spectrum $p(x_i)$ is not interpolated between pixels.

The above non-linear least-squares fit in general has no unique solution since in the case of stellar spectra the minimization function may consist of several minima at different offsets produced by similar spectral lines. Therefore, the problem must be solved in two steps: the first includes the solution of the linear fit to determine the parameters a and b for every trial offset δ , and the second one is to find the appropriate minimum of the $\chi^2(\delta)$ as a function of one variable.

The solution of the linear problem leads to the following transformation of the minimization function:

$$\chi^2(\delta) = (1 - r^2(\delta)) \cdot \sum \omega_i (p_i - \bar{p})^2, \quad (4.2)$$

where $\omega_i = 1/\sigma_i^2$ are the weighting factors as the inverse variances of the programme spectrum, r is the cross-correlation coefficient as a function of the offset:

$$r(\delta) = \frac{\sum \omega_i (p_i - \bar{p})(t_i(\delta) - \bar{t}(\delta))}{\sqrt{\sum \omega_i (p_i - \bar{p})^2 \cdot \sum \omega_i (t_i(\delta) - \bar{t}(\delta))^2}} \quad (4.3)$$

and the weighted averages are:

$$\bar{p} = \frac{\sum \omega_i p_i}{\sum \omega_i} \quad \text{and} \quad \bar{t}(\delta) = \frac{\sum \omega_i t_i(\delta)}{\sum \omega_i} \quad (4.4)$$

with the notation $t_i(\delta) \equiv t(x_i + \delta)$ for simplicity.

Since the latter term in Eq. (4.2) is constant, the minimum of the function can be found by choosing the appropriate peak of the cross-correlation function and using a centring algorithm to determine the position of the maximum. The variance of the parameter δ will then be defined as the inverse of the curvature matrix of $\chi^2(\delta)$ times the variance of the linear fit:

$$\sigma_\delta^2 = \frac{\chi^2(\delta)}{n-2} \cdot 2 \left(\frac{d^2 \chi^2}{d\delta^2} \right)^{-1}. \quad (4.5)$$

The second derivative of $\chi^2(\delta)$ is

$$\frac{d^2 \chi^2}{d\delta^2} = -2 \left[\left(\frac{dr}{d\delta} \right)^2 + r \frac{d^2 r}{d\delta^2} \right] \cdot \sum \omega_i (p_i - \bar{p})^2, \quad (4.6)$$

where the first derivative vanishes when the function is at minimum. Therefore

$$\frac{d^2 \chi^2}{d\delta^2} = -2r \frac{d^2 r}{d\delta^2} \cdot \sum \omega_i (p_i - \bar{p})^2 \quad (4.7)$$

and, finally, replacement of the weighted sum of the residuals from Eq. (4.2) gives:

$$\sigma_\delta^2 = - \left(\frac{d^2 r}{d\delta^2} \right)^{-1} \cdot \frac{1 - r^2}{r(n - 2)}, \quad (4.8)$$

where r is the amplitude of the cross-correlation peak at the offset δ , n is the number of the overlapped pixels of the two spectra at the given offset, and the inverse curvature of the peak can be determined with the selected centring algorithm.

The first component of the above formula describes the accuracy of the offset limited by the width and depth of the line(s): the shallower the line, the flatter the cross-correlation peak, hence, the larger the uncertainty of the offset. The second term describes both random and systematical components of the linear regression between the template and observed spectrum. The error of the centring of the cross-correlation peak and that of the curvature determination are small compared to the terms in Eq. (4.8) and, therefore, are neglected.

4.3.2 The accuracy for Gaussian profiles

Now, let us construct a simple example to gain some insight about the accuracy estimate. Let the program spectrum be a single Gaussian profile

$$p(x_i) = C \left(1 \pm d \exp \left[- \left(\frac{x_i - x_c}{\sigma_{\text{line}}} \right)^2 \right] \right) \quad (4.9)$$

centred at x_c with the width σ_{line} , d is the relative line depth (strength), C is the continuum level. The spectrum is sampled with the step size $\Delta\lambda$ over n pixels. Let the normally distributed noise with the variance σ^2 be added to the spectrum $p(x)$. Let the template spectrum be the same profile but noiseless.

The cross-correlation of two Gaussians is equivalent to the convolution of the two profiles which results in a Gaussian shape:

$$r(\delta) = r_0 \exp \left(- \frac{\delta^2}{2 \sigma_{\text{line}}^2} \right), \quad (4.10)$$

which gives the curvature of the cross-correlation function at its maximum

$$\frac{d^2 r}{d\delta^2} = - \frac{r_0}{\sigma_{\text{line}}^2}. \quad (4.11)$$

The sum of the weighted ($\omega_i = 1/\sigma^2$) squared deviations of the programme spectrum p_i from the mean \bar{p} is obtained after the integration:

$$\sum \omega_i (p_i - \bar{p})^2 = \sqrt{\frac{\pi}{2}} \cdot \frac{C^2}{\sigma^2} \cdot \frac{d^2 \sigma_{\text{line}}}{\Delta \lambda} \left(1 - \frac{\sqrt{2\pi} \sigma_{\text{line}}}{n \Delta \lambda} \right). \quad (4.12)$$

Neglecting the ratio in the brackets (if $n \Delta \lambda \gg \sigma_{\text{line}}$) and introducing the signal-to-noise ratio in the continuum ($\text{SNR} = C/\sigma$), the integral reads

$$\sum \omega_i (p_i - \bar{p})^2 = \sqrt{\frac{\pi}{2}} \cdot \frac{d^2 \sigma_{\text{line}}}{\Delta \lambda} \cdot (\text{SNR})^2. \quad (4.13)$$

The variance term in Eq. (4.5) will be

$$\frac{\chi^2(\delta)}{n-2} = 1 \quad (4.14)$$

in this model, since no systematical difference has been introduced between two equal Gaussians, therefore, the squared sum of weighted residuals $\chi^2(\delta)$ of the linear regression will be exactly equal to the number of degrees of freedom $n-2$.

Then, expressing σ_{line} by FWHM and putting all terms together we obtain:

$$\sigma_\delta^2 = \sqrt{\frac{1}{2\pi \ln 2}} \cdot \left(\frac{1}{r_0 \cdot \text{SNR} \cdot d} \right)^2 \Delta \lambda \cdot \text{FWHM}. \quad (4.15)$$

The constant in front of the equation is about 0.48. The equation derived resembles to ones obtained by other authors (e.g. Brown 1990). The better the sampling interval, the deeper and narrower the line; the higher the signal-to-noise ratio, the better the accuracy of the cross-correlation. It was also derived but omitted here for simplicity, that the inclusion of m similar Gaussians into the model will decrease the variance to σ_δ^2/m accordingly.

4.4 Rebinning into radial velocity scale

The offset in radial velocity scale between two spectral lines depends on the wavelengths of the lines. In order to measure the offset in radial velocities, the spectra in wavelengths have to be rebinned to a scale with a constant step size in velocities according to the Doppler formula:

$$\frac{\Delta v}{c} = \frac{\Delta \lambda}{\lambda} = \Delta \ln \lambda, \quad (4.16)$$

where Δv is the radial velocity difference between two wavelengths separated by $\Delta \lambda$ around wavelength λ , c is the speed of light, and in this linear approximation $\Delta v \ll c$ and $\Delta \lambda \ll \lambda$.

The constant step size in velocities is achieved after the transformation of the wavelength scale to the constant step size in $\ln \lambda$, which results in the definition of the rebinning grid:

$$\ln \lambda_i = \ln \lambda_0 + i \cdot \Delta \ln \lambda \quad (4.17)$$

with λ_0 being the initial wavelength of the spectrum, the index $i = 0, 1, \dots, n-1$. An ordinary rebinning in wavelengths implies that the difference in wavelengths in the new grid is constant, but in the case of radial velocities, the ratio between wavelengths in the new grid (in the subsequent nodes) must be constant.

It is more convenient than $\ln \lambda$ to have velocity units for describing the pixel positions. One should realize that the possibly high velocities resulting from this transformation do not have any physical meaning; only velocity differences between nearby ($\Delta v \ll c$) features in the same spectrum or between the same features in different spectra indicate the Doppler shift. The velocity scale is merely a reformulation of the commonly used $\ln \lambda$ scale.

One choice of the step size is a predefined velocity step size, the more flexible option is to select an average velocity as follows:

$$\Delta v = c \cdot \Delta \ln \lambda = c \cdot \frac{\ln \lambda_{n-1} - \ln \lambda_0}{n-1} = \frac{c}{n-1} \cdot \ln \frac{\lambda_{n-1}}{\lambda_0}. \quad (4.18)$$

The intensities of the spectrum are integrated

$$\hat{s}_i = \int_{\lambda^-}^{\lambda^+} s(\lambda_i) d\lambda \quad (4.19)$$

within the interval in wavelengths defined as

$$\lambda_i^\pm = \lambda_0 \cdot \exp \left[\frac{\Delta v}{c} \cdot (i \pm 0.5) \right]. \quad (4.20)$$

It is convenient to have a grid in the velocity scale common to different spectra. Since the grid is linear, the zero point can be established at the wavelength of a spectral feature λ_c common to a number of spectra. The initial velocity at the wavelength λ_0 of the first pixel of the spectrum and the velocity grid is therefore given by:

$$v_i = c \cdot \ln \frac{\lambda_0}{\lambda_c} + \Delta v \cdot i. \quad (4.21)$$

There is an alternative and intermediate way to transform into radial velocity scale without involving the rebinning procedure. This results in the unequally spaced

spectra with the linear velocity scale, i.e. the distance between two features caused by a radial velocity shift at different wavelengths remains constant. The procedure also involves the wavelength λ_c of a common feature of the spectra. The velocities for each pixel k in the spectrum are calculated according to

$$v_i = c \cdot \ln \frac{\lambda_i}{\lambda_c}. \quad (4.22)$$

The intensities of the spectrum remain unchanged in their pixels until a number of spectra have to be rebinned into the same grid for cross-correlation or arithmetical operations.

Chapter 5

Deconvolution of stellar spectra

5.1 Introduction

The observed stellar spectra are subject to broadening due to various instrumental and physical effects. If the effects are known and can be modeled then the true spectral profile can be recovered. Presence of noise in the spectra makes the problem of restoration ill-posed. The solution of the problem can be found by solving the inverse problem formulated in various ways. In this chapter we consider the restoration of the underlying spectrum and the broadening function. These inverse problems play a key role in the modern methods of the analysis of stellar spectra. The basic applications are highlighted as follows.

Deconvolution of the blurred spectra with the known point spread function (PSF) is the way to increase the spectral resolution and to resolve narrow features. Hereafter we refer to the term of the PSF caused only by the spectrograph, i.e. it is the instrumental profile. Deconvolution with e.g. the known rotational profile would refine the exact position and the structure of the interior of the spectral lines.

Deconvolution of the observed low resolution spectrum with the PSF obtained with a smaller step size (and a higher resolution) results in a spectrum of a higher resolution. The increase factor depends on the sample length. Another way to increase the resolution keeping the sample length fixed is to use a different observing technique known as dithering (Lauer 1999, where it is applied to the WFPC images of the HST) to obtain spectra shifted with respect to each other by a multiple of the pixel size. Such a number of spectra interleaved in the wavelength scale decreases the step size but not the resolution (Gray 1986 uses a dithering device to produce the interleaved spectra to improve the accuracy of the line bisectors).

Deconvolution with the proper PSF will increase the resolution of the observed spectra.

The restoration of the broadening function depends on the template spectrum. Several different cases can be summarized:

1. The template spectrum is of the same kind as the observed one, but obtained with a higher resolution and preferably with a higher signal-to-noise ratio (SNR). One natural choice is to use the solar spectrum obtained with the spectrograph and the FTS solar spectrum (Kurucz et al. 1984). The restoration of the PSF made with these spectra for several spectrographs was described by Valenti et al. (1995), who also used a spectrum of an iodine cell. The restoration is an alternative way to obtain the PSF of the spectrograph instead of its direct measurement with the use of a laser or telluric lines (Griffin 1969). The use of a synthetic spectrum is also possible but increases uncertainty of the restoration due to an additional freedom in the choice of the stellar parameters and the broadening function.
2. The template spectrum consists of a number of delta functions with their positions and intensities corresponding to the spectral line list. The restoration of the broadening function gives a mean spectral profile of the observed spectrum which is de-blended from the delta functions but includes the PSF. The use of many spectral lines, which is possible with échelle spectra, can increase the accuracy of the restored stellar profile. The use of the delta-spectrum convolved with the known PSF as a template in the deconvolution results in a mean profile free of the instrumental effects. The method has become known as the least-squares deconvolution (LSD) and was implemented by Donati et al. (1997) and Collier Cameron (1999).
3. The template is calculated by the integration of the local line profiles over the stellar disk weighted with a limb-darkening function. In the case of a rotational broadening mechanism, the restored broadening function will represent the true rotational profile, including effects like asymmetric macro-turbulence. This true profile can then be used to deblend lines which cannot be modeled reliably. The deconvolved profile is free from the assumptions made in modeling the rotational profile (Gray 1992, Ch.17).
4. Restoration of the blended profiles of binary systems as a function of the orbital phase involves a template spectrum of a single star. The method was successfully used by Rucinski (1999) to resolve the double components of the observed profile. It was demonstrated that the deconvolution has a certain advantage as compared to the widely used cross-correlation technique.

One related problem, where many of the same techniques used in deconvolution problems can also be applied, is the restoration of the distribution of stellar parameters across the star's surface. A range of techniques has been developed, known in

general as the Doppler imaging technique, to solve the ill-posed inversion problem to restore the stellar surface from a time series of one-dimensional stellar spectra (Vogt et al. 1987, Piskunov et al. 1990, Collier Cameron 1992, and Berdyugina 1998).

5.2 Formulation of the problem

The convolution of the known true spectrum $t(x)$ with the unknown kernel $p(x)$, which is the instrumental PSF or a broadening function, results for the continuous case in the blurred function $s(x)$ co-added with the known function of the random noise $\epsilon(x)$

$$s(x) = \int_{-\infty}^{+\infty} t(x-u)p(u)du + \epsilon(x) \quad (5.1)$$

which is the first problem: the reconstruction of the unknown function $p(x)$. The convolution of the unknown true spectrum $t(x)$ with the known kernel $p(x)$

$$s(x) = \int_{-\infty}^{+\infty} p(x-u)t(u)du + \epsilon(x) \quad (5.2)$$

is the second problem: the reconstruction of the true spectrum $t(x)$.

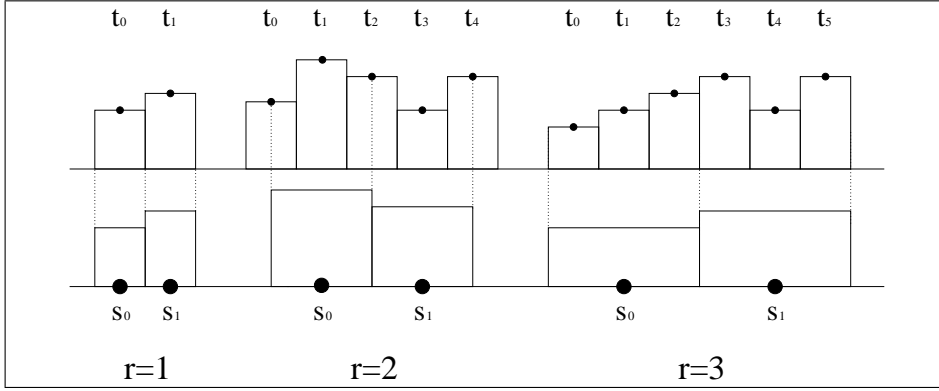
5.3 The sampling matrix

The convolution process becomes discrete once it is sampled and integrated (recorded) with the CCD. For simplicity, let the CCD pixels be adjacent (no gaps) and have a flat response within each pixel (Jordan et al. 1993 showed that this assumption is not very accurate). Furthermore, assume that either $t(u)$ or $p(u)$ are known on a sampling grid finer than the actual CCD pixel size. To match the spectra, we need to resample the convolved function to the pixel size of the observed spectrum.

The length of the restored function depends on the sampling rate, an *integer* multiple r of the sampling interval of $t(u)$ or $p(u)$ which equals the sampling interval of $s(x)$:

$$r = \frac{\Delta x}{\Delta u}. \quad (5.3)$$

The equal step size of the observed spectrum remains unchanged but the template (profile) is rebinned with the new step size $\Delta x/r$ according to the following scheme:



The choice for the configuration of the template pixels for even r is more complicated than e.g. Valenti et al. (1995); it is employed in order to minimize the loss of resolution. Therefore, we use a more sophisticated scheme where the centre of one of the template pixels coincides with that of the observed pixel.

The integration of a single pixel is described by the sampling row-vector $\mathbf{h}_{1 \times q}$ so that¹

$$s_i = \sum_{k=0}^{q-1} h_k t_{i-r+k} \quad (5.4)$$

and the number of pixels involved in the integration over one pixel in the observed spectrum is

$$q = \frac{r}{2} \cdot 2 + 1, \quad (5.5)$$

where the ratio is an *integer* division. The normalized elements of the sampling vector are

$$\mathbf{h}_{1 \times q} = [h_i] = \frac{1}{r} \begin{cases} (0.5 & 1 & \dots & 1 & 0.5), & r \text{ is even,} \\ (1 & 1 & \dots & 1 & 1), & r \text{ is odd.} \end{cases} \quad (5.6)$$

The resampling of the whole spectrum $\mathbf{t}_{l \times 1}$ into $\mathbf{s}_{n \times 1}$ is described by the product with the sampling matrix $\mathbf{H}_{n \times l}$:

$$\mathbf{s}_{n \times 1} = \mathbf{H}_{n \times l} \cdot \mathbf{t}_{l \times 1} \quad (5.7)$$

¹In this Chapter indices run from zero.

where the elements of the matrix are the sampling vectors shifted row-wise by the sampling rate r and given by:

$$\mathbf{H}_{n \times l} = [H_{i, ir+k}] = h_k, \quad k = 0, 1, \dots, q-1, \quad i = 0, 1, \dots, n-1. \quad (5.8)$$

The number of pixels of the template spectrum $\mathbf{t}_{l \times 1}$ satisfies the following condition:

$$l = \begin{cases} qn, & r \text{ is odd,} \\ (q-1)n + 1, & r \text{ is even.} \end{cases} \quad (5.9)$$

The following is the illustration of the sampling matrix with $r = 3$, $n = 2$, $l = 6$:

$$\begin{pmatrix} h_0 & h_1 & h_2 & 0 & 0 & 0 \\ 0 & 0 & 0 & h_0 & h_1 & h_2 \end{pmatrix} \begin{pmatrix} t_0 \\ t_1 \\ t_2 \\ t_3 \\ t_4 \\ t_5 \end{pmatrix} = \begin{pmatrix} s_0 \\ s_1 \end{pmatrix}.$$

5.4 Deconvolution of the PSF

The formation of the observed spectrum with the known true or expected spectrum in the discrete case is given by:

$$\mathbf{s}_{n \times 1} = \mathbf{H}_{n \times l} \cdot \mathbf{T}_{l \times m} \cdot \mathbf{p}_{m \times 1} + \boldsymbol{\epsilon}_{n \times 1}, \quad (5.10)$$

where \mathbf{s} is the observed spectrum and $\boldsymbol{\epsilon}$ is the vector of its random noise, \mathbf{H} is the sampling matrix, and \mathbf{T} is the offset matrix of the template spectrum $\mathbf{t}_{l \times 1}$. Its length is defined by the sampling matrix

$$l = \begin{cases} qn, & r \text{ is odd,} \\ (q-1)n + 1, & r \text{ is even,} \end{cases} \quad (5.11)$$

and \mathbf{p} is the unknown PSF of length m . The *odd* number of pixels m can be less than that of the template spectrum and should be selected from the interval $q \ll m \leq l$. The elements of the matrix \mathbf{T} are constructed by shifting the template spectrum $\mathbf{t}_{l \times 1}$ and the elements are:

$$\mathbf{T}_{l \times m} = [T_{ik}] = \begin{cases} t_{i-m/2+k}, & 0 \leq i - m/2 + k < l \\ 0, & \text{otherwise.} \end{cases} \quad (5.12)$$

The following example illustrates the contents of the matrices for $r = 2$, $n = 3$, $m = 5$, and $l = 7$:

$$\begin{pmatrix} h_0 & h_1 & h_2 & 0 & 0 & 0 & 0 \\ 0 & 0 & h_0 & h_1 & h_2 & 0 & 0 \\ 0 & 0 & 0 & 0 & h_0 & h_1 & h_2 \end{pmatrix} \begin{pmatrix} 0 & 0 & t_0 & t_1 & t_2 \\ 0 & t_0 & t_1 & t_2 & t_3 \\ t_0 & t_1 & t_2 & t_3 & t_4 \\ t_1 & t_2 & t_3 & t_4 & t_5 \\ t_2 & t_3 & t_4 & t_5 & t_6 \\ t_3 & t_4 & t_5 & t_6 & 0 \\ t_4 & t_5 & t_6 & 0 & 0 \end{pmatrix} \begin{pmatrix} p_0 \\ p_1 \\ p_2 \\ p_3 \\ p_4 \end{pmatrix} = \begin{pmatrix} s_0 \\ s_1 \\ s_2 \end{pmatrix}.$$

The design matrix of the convolution model is the product

$$\mathbf{A}_{n \times m} = \mathbf{H}_{n \times l} \cdot \mathbf{T}_{l \times m} \quad (5.13)$$

and the PSF profile can be found by solving the least-squares problem:

$$\mathbf{s}_{n \times 1} = \mathbf{A}_{n \times m} \cdot \mathbf{p}_{m \times 1} + \boldsymbol{\epsilon}_{n \times 1}. \quad (5.14)$$

The obtained system of equations should be well conditioned if $n \gg m$ and can be solved with the standard methods of least-squares with the use of e.g. the Cholesky decomposition for the inversion. Since, in general for the applications described, \mathbf{A} is not well-behaved, we shall proceed with the ill-posed solutions as described in Sec. 5.6.

5.5 Deconvolution of the spectrum

The formation of the observed spectrum convolved with the known PSF in the discrete case is given by:

$$\mathbf{s}_{n \times 1} = \mathbf{H}_{n \times m} \cdot \mathbf{P}_{m \times m} \cdot \mathbf{t}_{m \times 1} + \boldsymbol{\epsilon}_{n \times 1}, \quad (5.15)$$

where \mathbf{s} is the observed spectrum of length n and $\boldsymbol{\epsilon}$ is the vector of its random noise, \mathbf{H} is the sampling matrix, \mathbf{P} is the offset matrix of the known PSF vector $\mathbf{p}_{l \times 1}$. The length l is an *odd* number, \mathbf{t} is the unknown deconvolved spectrum and its length is defined by the sampling matrix:

$$m = \begin{cases} qn, & r \text{ is odd,} \\ (q-1)n+1, & r \text{ is even.} \end{cases} \quad (5.16)$$

The elements of the matrix \mathbf{P} are constructed by shifting the elements of the PSF vector \mathbf{p} :

$$\mathbf{P}_{m \times m} = [P_{ik}] = \begin{cases} p_{l/2+k-i} / \sum_k p_k, & 0 \leq l/2+k-i < l \\ 0, & \text{otherwise} \end{cases} \quad (5.17)$$

and the elements in each row are normalized to their sum in order to preserve the intensities of the deconvolved spectrum at its edges.

The following example illustrates the contents of the matrices for $r = 2$, $n = 3$, $m = 7$, $l = 5$, not showing the profile normalization:

$$\begin{pmatrix} h_0 & h_1 & h_2 & 0 & 0 & 0 & 0 \\ 0 & 0 & h_0 & h_1 & h_2 & 0 & 0 \\ 0 & 0 & 0 & 0 & h_0 & h_1 & h_2 \end{pmatrix} \begin{pmatrix} p_2 & p_3 & p_4 & 0 & 0 & 0 & 0 \\ p_1 & p_2 & p_3 & p_4 & 0 & 0 & 0 \\ p_0 & p_1 & p_2 & p_3 & p_4 & 0 & 0 \\ 0 & p_0 & p_1 & p_2 & p_3 & p_4 & 0 \\ 0 & 0 & p_0 & p_1 & p_2 & p_3 & p_4 \\ 0 & 0 & 0 & p_0 & p_1 & p_2 & p_3 \\ 0 & 0 & 0 & 0 & p_0 & p_1 & p_2 \end{pmatrix} \begin{pmatrix} t_0 \\ t_1 \\ t_2 \\ t_3 \\ t_4 \\ t_5 \\ t_6 \end{pmatrix} = \begin{pmatrix} s_0 \\ s_1 \\ s_2 \end{pmatrix}$$

The design matrix of the convolution model is the product

$$\mathbf{A}_{n \times m} = \mathbf{H}_{n \times m} \cdot \mathbf{P}_{m \times m} \quad (5.18)$$

and the deconvolved spectrum \mathbf{t} can be found by solving the inverse problem:

$$\mathbf{s}_{n \times 1} = \mathbf{A}_{n \times m} \cdot \mathbf{t}_{m \times 1} + \boldsymbol{\epsilon}_{n \times 1}. \quad (5.19)$$

The matrix \mathbf{A} is an r -times underdetermined system of linear equations: no unique solution exists unless we use the solution of ill-posed problems described below. The solution to the problem is extensively described in Sec. 5.6.

5.6 The principal components regression

Modern methods of matrix factorizations give a new treatment of the linear least-squares problem (Watkins 1991, Stoer 1993, Golub & van Loan 1989). The classical method of least-squares is a perfect way to solve the problem, except in the case

when the matrix of normal equations $\mathbf{A}'\mathbf{W}\mathbf{A}$ is close to singular.² This may happen when the number of free parameters exceeds the number of observations, or/and when the parameters of the model chosen to describe the observed process are heavily correlated with each other. This results in a linear dependence of rows of the design matrix \mathbf{A} , reduction of its rank, and singularity of the inversion or plurality of the solution.

The problem can be solved in a different way based on the concept of orthogonal decomposition of the model which we use to describe the observations. This results in a new system of equations, which uses orthogonal functions (i.e. a new orthogonal design matrix), and in a new set of unknown parameters, known as the *principal components*, which are independent of and uncorrelated with each other. The least-squares solution of the orthogonal system of equations to the observations gives the unknown principal components parameters.

The independence of the parameters will allow us to test the statistical significance of the terms in a simple manner to decide which of them can be eliminated from the fit. The vector from which the insignificant components have been eliminated comprises the *reduced principal components*. The original set of unknowns is then obtained by back composition of the truncated set of the independent parameters with a matrix which describes the linear dependence of the original parameters. Due to the cancellation of the insignificant principal components the solution in terms of the original unknown parameters is not unique, and forms a family of parameter sets. The size of the family can be reduced by imposing additional linear constraints on the problem.

One can see a similarity between the spectral decomposition by Fourier transformation and the above orthogonal functions. The difference is that the Fourier harmonics are the trigonometric functions while here, the orthogonal functions are not specified, except that they satisfy the orthogonality condition. The trigonometric functions are orthogonal only for continuous data; they are in general not orthogonal on a given data window; the construction of the principal components ensures that their associated basis functions are orthogonal given the observations. The same approach is used when a set of orthogonal polynomials is constructed.

The solutions to ill-conditioned and singular linear systems was described and discussed in many papers and monographs, some of them were used here: Hocking (1976), who reviewed the solutions based on the principal components and rigid estimators, Jackson (1991), Hansen (1997), and Dunteman (1989). The principal components solution is similar to the truncated least-squares (TLS) developed by Golub & van Loan (1980) for solving overdetermined systems of linear equations, who have also extended it to the total TLS approach where the variances of the variables of the model are incorporated into the minimization functional. Neumaier (1998) discussed the problem in terms of the truncated singular value decomposition (SVD), together with many other aspects of the inversion problems.

² \mathbf{A} is the design matrix, \mathbf{A}' is its transposed, and \mathbf{W} is the weight matrix.

Let the linear model, describing an observed process, be given in the form:

$$\mathbf{y} = \mathbf{A}\mathbf{p} + \boldsymbol{\epsilon}, \quad (5.20)$$

where $\mathbf{y}_{n \times 1}$ is the observations and $\boldsymbol{\epsilon}_{n \times 1}$ is the vector of their random noise, $\mathbf{A}_{n \times m}$ is the design matrix, and $\mathbf{p}_{m \times 1}$ is the vector of unknown parameters or underlying function. The number of unknown parameters m could be less or greater than the number of observations n . The noise in the observations is characterized by the positively definite and symmetric dispersion matrix $\mathcal{E}(\boldsymbol{\epsilon}'\boldsymbol{\epsilon}) = \mathcal{D}(\mathbf{y})$.

In order to satisfy the orthogonal condition of the decomposition of \mathbf{A} , we need to decompose the variance matrix into two matrices. If the variance matrix is not diagonal, the Cholesky factorization results in a lower triangular matrix \mathbf{S} :

$$\mathcal{D}(\mathbf{y}) = \sigma^2 \mathbf{W}^{-1} = \sigma^2 \mathbf{S}\mathbf{S}', \quad (5.21)$$

where it is assumed that the dispersions are known up to some scaling factor σ^2 . To obtain the weighting matrix we need to invert the dispersion matrix:

$$\mathbf{W} = \sigma^2 \mathcal{D}^{-1}(\mathbf{y}) = (\mathbf{S}^{-1})'(\mathbf{S}^{-1}) = \mathbf{V}'\mathbf{V}. \quad (5.22)$$

The inversion of the lower triangular \mathbf{S} is straightforward (Press et al. 1992). In the case of uncorrelated noise in the observations, the diagonal elements of \mathbf{V} are simply the inverse of the standard deviations: $\mathbf{V} = [\sigma_{ii}^{-1}]$.

The orthogonal basis of the matrix $(\mathbf{V}\mathbf{A})_{n \times m}$ can be obtained with the QR factorization (Golub & van Loan, 1989) or with the SVD (the algorithm in Press et al. 1992 is based on Golub & van Loan, 1989). The latter factorization is more suitable for the current problem and decomposes the matrix into three components:

$$\mathbf{V}\mathbf{A} = \mathbf{B}\mathbf{C}\mathbf{D}', \quad (5.23)$$

where the matrix $\mathbf{B}_{n \times m}$ contains the orthonormal *basis* vectors ($\mathbf{B}'\mathbf{B} = \mathbf{I}_{m \times m}$, but $\mathbf{B}\mathbf{B}' \neq \mathbf{I}$), the diagonal matrix $\mathbf{C}_{m \times m}$ contains the *singular* values of the decomposition, and the orthonormal $\mathbf{D}_{m \times m}$ is the linear *dependence* matrix ($\mathbf{D}'\mathbf{D} = \mathbf{D}\mathbf{D}' = \mathbf{I}_{m \times m}$).

The elements of $\mathbf{C} = \text{diag}(c_0, c_1, \dots, c_{m-1})$ are $c_0 \geq c_1 \geq \dots \geq c_{m-1} \geq 0$ and the rank of $\mathbf{V}\mathbf{A}$ equals the number of non-zero singular elements.

The columns of \mathbf{B} are the eigenvectors and \mathbf{C}^2 are the eigenvalues of

$$(\mathbf{V}\mathbf{A})(\mathbf{V}\mathbf{A})' = \mathbf{B}\mathbf{C}^2\mathbf{B}'$$

The columns of \mathbf{D} are the eigenvectors and \mathbf{C}^2 are the eigenvalues of

$$(\mathbf{V}\mathbf{A})'(\mathbf{V}\mathbf{A}) = \mathbf{A}'\mathbf{W}\mathbf{A} = \mathbf{D}\mathbf{C}^2\mathbf{D}'$$

The approximated function becomes

$$\tilde{\mathbf{y}} = \mathbf{A}\mathbf{p} = \mathbf{V}^{-1}\mathbf{B}\mathbf{C} \cdot \mathbf{D}'\mathbf{p} = \mathbf{T} \cdot \mathbf{q} \quad (5.24)$$

i.e. expressed in the new terms

$$\mathbf{T} = \mathbf{V}^{-1}\mathbf{B}\mathbf{C} \quad \text{and} \quad \mathbf{q} = \mathbf{D}'\mathbf{p} \quad (5.25)$$

of the new design matrix \mathbf{T} which is orthogonal with the weights of observations $\mathbf{T}'\mathbf{W}\mathbf{T} = \mathbf{C}'\mathbf{C} = \mathbf{C}^2$, and of the vector \mathbf{q} of uncorrelated unknowns, known as the principal components of the vector \mathbf{p} .

Denoting the vector of the residuals of the fit as $\mathbf{r} = \mathbf{y} - \tilde{\mathbf{y}}$, the minimization functional becomes

$$\sigma^2\chi^2(\mathbf{q}) = \mathbf{r}'\mathbf{W}\mathbf{r} = (\mathbf{y} - \mathbf{T}\mathbf{q})' \mathbf{W}(\mathbf{y} - \mathbf{T}\mathbf{q}) \quad (5.26)$$

The minimum of the norm $(\mathbf{A}\mathbf{x} - \mathbf{y})'(\mathbf{A}\mathbf{x} - \mathbf{y})$ is at \mathbf{x} obtained from the normal equations $\mathbf{A}'\mathbf{A}\mathbf{x} = \mathbf{A}'\mathbf{y}$.

The system of normal equations is

$$\mathbf{T}'\mathbf{W}\mathbf{T}\mathbf{q} = \mathbf{T}'\mathbf{W}\mathbf{y} \quad (5.27)$$

which then becomes

$$\mathbf{C}^2\mathbf{q} = \mathbf{C}\mathbf{B}'\mathbf{V}\mathbf{y} \quad (5.28)$$

and readily gives the solution for the principal components

$$\mathbf{q} = \mathbf{C}^{-1}\mathbf{B}'\mathbf{V}\mathbf{y}. \quad (5.29)$$

The original parameters, or the underlying function, is a linear combination of the principal components:

$$\mathbf{p} = \mathbf{D}\mathbf{q}. \quad (5.30)$$

The diagonal of the dispersion matrix of the principal components is:

$$\mathcal{D}(\mathbf{q}) = \mathbf{C}^{-1}\mathbf{B}'\mathbf{V} \cdot \mathcal{D}(\mathbf{y}) \cdot \mathbf{V}\mathbf{B}\mathbf{C}^{-1} = \sigma^2 \mathbf{C}^{-2} \quad (5.31)$$

and the dispersion matrix of the original parameters is

$$\mathcal{D}(\mathbf{p}) = \mathbf{D}\mathcal{D}(\mathbf{q})\mathbf{D}' = \sigma^2\mathbf{D}\mathbf{C}^{-2}\mathbf{D}'. \quad (5.32)$$

And finally, the approximated function is

$$\tilde{\mathbf{y}} = \mathbf{A}\mathbf{p} = \mathbf{T}\mathbf{q} = \mathbf{V}^{-1}\mathbf{B}\mathbf{C}\mathbf{q}. \quad (5.33)$$

The dispersion matrix of the fit is

$$\mathcal{D}(\tilde{\mathbf{y}}) = \mathbf{T}\mathcal{D}(\mathbf{q})\mathbf{T}' = \sigma^2(\mathbf{V}^{-1}\mathbf{B}) \cdot (\mathbf{V}^{-1}\mathbf{B})' = \sigma^2\mathbf{S}\mathbf{B}\mathbf{B}'\mathbf{S}', \quad (5.34)$$

where $\mathbf{V}^{-1} = \mathbf{S}$ as it was introduced for the standard deviations of the additive random noise of the observations in (5.21) and (5.22).

5.7 Selection of the principal components

To find a stable solution to the problem, we have to eliminate the $m - k$ smallest principal components in \mathbf{q} which have the largest variances and contribute noisy components to \mathbf{p} . A number of tests can be used which results in a vector of the *reduced principal components* $\tilde{\mathbf{q}}$ with the last $m - k$ terms are set to zero. This causes also the corresponding terms of the singular values in \mathbf{C} to become zero.

5.7.1 The F -test

The squared sum of the residuals of the fit (RSS) is

$$\mathbf{r}'\mathbf{W}\mathbf{r} = \mathbf{y}'\mathbf{W}\mathbf{y} - \sigma^2\mathbf{q}'\mathcal{D}^{-1}(\mathbf{q})\mathbf{q} = \mathbf{y}'\mathbf{W}\mathbf{y} - \mathbf{q}'\mathbf{C}^2\mathbf{q}, \quad (5.35)$$

which is the series of the terms

$$\text{RSS}_m = \mathbf{y}'\mathbf{W}\mathbf{y} - \sum_{k=0}^{m-1} q_k^2 c_k^2 = \sum_{i=0}^{n-1} \omega_i y_i^2 - \sum_{k=0}^{m-1} q_k^2 c_k^2 \quad (5.36)$$

and obeys the recurrence relation:

$$\text{RSS}_k = \text{RSS}_{k-1} - q_k^2 c_k^2. \quad (5.37)$$

Since the principal components \mathbf{q} are linearly (hence, statistically) independent, each of them can be tested for its statistical significance in the fit.

A standard F -test can be applied to the principal components by evaluating the change of the RSS as a function of the index k . The null hypothesis $H : q_k = 0$ is tested against its alternative $H_1 : q_k \neq 0$ to check the significance of q_k . If the hypothesis is true, then it follows that $\text{RSS}^H = \text{RSS}_{k-1}$, and the F statistics is

$$F_k = \frac{\text{RSS}_{k-1} - \text{RSS}_k}{\text{RSS}_k/(n-k)} = \frac{q_k^2 c_k^2}{\text{RSS}_k/(n-k)}. \quad (5.38)$$

The hypothesis is accepted if the probability for F_k being as small as it is obtained,

$$P(F > F_k) = Q(F_k, 1, n-k) > 1 - \alpha, \quad (5.39)$$

is higher than some level given by the significance of the fit α which is e.g. 95%. If the hypothesis H is accepted, then the element k is considered insignificant and all subsequent $m - k$ components are set to zero. In many practical cases, the statistics F may show a wiggly or noisy behaviour superimposed on the obvious decaying trend as the index k increases. Therefore, a careful analysis based on several consecutive components is needed to decide where it crosses the significance level.

5.7.2 Goodness of the fit

The reduced χ^2 of the minimization functional is a function of the number k of the principal components (χ^2 is also the correction coefficient for the sample variance σ^2):

$$\chi_{n-k}^2 = \sigma^2 = \frac{\text{RSS}_k}{n-k}, \quad (5.40)$$

where the index $k = 0, 1 \dots r$ and $r = \text{rank}(\mathbf{VA})$ is a number of the non-zero singular values $r \leq \min(n, m)$. If the variances of the observations are known exactly ($\sigma^2 = 1$), then the number of the principal components can be selected when χ_{n-k}^2 as a function of k descends to the unity level, or any other pre-defined level if the variances are not exactly known.

A visual inspection of the plot of χ_{n-k}^2 as a function of the index k is also useful for the subjective definition of the number of components at some kink or sudden drop of the function.

5.7.3 Analysis of variance

As it was shown, the sum of the diagonal elements of the dispersion matrix of the original parameters equals the total sum of variances of the principal components:

$$\text{tr}\mathcal{D}(\mathbf{p}) = \text{tr}\mathcal{D}(\mathbf{q}) = \text{tr}\mathbf{C}^{-2} \quad (5.41)$$

i.e. this defines the third stopping criterion to select the number of components for which the sum of variances is less than a predefined threshold for the maximally

allowed sum of variances of the original parameters. The criterion described by Kendall (1975) is based on the analysis of the sum of the minimal singular values \mathbf{C} which obeys the χ^2 distribution.

5.8 The constrained principal components solution

The solution to the constrained linear least-squares problem is detailed in Ilyin (2000):

$$\begin{aligned} \mathbf{y} &= \mathbf{A}\mathbf{p} + \boldsymbol{\epsilon} & \text{subject to :} & & \mathbf{G}\mathbf{p} &\geq \mathbf{c} \\ \mathbf{y} &= \mathbf{A}\mathbf{p} + \boldsymbol{\epsilon} & \text{subject to :} & & \mathbf{G}\mathbf{p} &\leq \mathbf{c}, \end{aligned} \quad (5.42)$$

where $\mathbf{G}_{l \times m}$ is the linear condition matrix, $\mathbf{c}_{l \times 1}$ is the vector of constants constraining the solution $\mathbf{p}_{m \times 1}$, and the number of the constraints $l \leq m$.

The use of the principal components does not change essentially in the solution, although, the form of the Lagrangian solution is slightly modified:

$$\mathbf{p} = \bar{\mathbf{p}} - (\mathbf{D}\mathbf{C}^{-2}\mathbf{D}')\mathbf{G}' \cdot (\mathbf{G}(\mathbf{D}\mathbf{C}^{-2}\mathbf{D}')\mathbf{G}')^{-1} \cdot (\mathbf{G}\bar{\mathbf{p}} - \mathbf{c}), \quad (5.43)$$

where $\bar{\mathbf{p}} = \mathbf{D}\bar{\mathbf{q}}$ is the unconstrained reduced principal components solution.

As an example it is demonstrated how it works in one particular case often met in practice when we need to find the solution whose sum is equal to some predefined number

$$\sum_{k=0}^{m-1} p_k = c, \quad (5.44)$$

or, in the other words, the solution is normalized. The matrix $\mathbf{G}_{1 \times m} = (1, 1, \dots, 1)$ is a unity row, and the constant sum is $\mathbf{c}_{1 \times 1} = c$. Denoting the elements of the dispersion matrix $\mathcal{D}(\mathbf{p})\sigma^{-2} = \mathbf{D}\mathbf{C}^{-2}\mathbf{D}' = [\sigma_{ik}^2]$, we form a vector

$$\mathbf{v}_{m \times 1} = [v_i] = \sum_{k=0}^{m-1} \sigma_{ik}^2, \quad (5.45)$$

i.e. the sums of the dispersions in each row. Then the elements of the vector of the constraint solution is

$$p_i = \tilde{p}_i - \frac{v_i}{\sum v_k} \cdot (\sum \tilde{p}_k - c), \quad (5.46)$$

which shows that the difference between the obtained and expected sums is applied via the multiple correlation coefficient to correct the solution. One can also see that in the constrained solution $\sum p_i = c$.

5.9 Linear regularization methods

The principal components analysis is, in fact, a particular method of a more general class of minimization problems known as the regularization methods of the inverse problem.

The orthogonal decomposition of the design matrix, described in the previous sections, is equivalent to spectral decomposition of the observed process. The set of orthogonal functions is the set of discrete spatial harmonics, which describe the data, and comprises the columns of the matrix \mathbf{T} and the principal components \mathbf{q} are interpreted as their amplitudes. Selection of the reduced set of the components acts as a spatial filter which is a trade-off between the amplitude of the smallest spatial harmonics and the noise. Generally speaking, such a compromise can be established in many inverse problems where the amplitude of the smallest spatial harmonic is well distinguished from the low level noise, i.e. it works very well for the broad features in a spectrum with high signal-to-noise ratio. For a lower signal-to-noise the principal components cannot distinguish between the harmonics and the random noise, hence, they tend to pick noisy features of the solution (one possible remedy to the problem is to obtain these harmonics with a higher accuracy by extending the length of the data sample, i.e. use of many spectra instead of one for deconvolution, for example). This is the insufficiency of the method and leads to the addition of external conditions which can control, e.g. the shape of the solution. The additional conditions are invoked into the minimization functional which controls the shape of the solution and the strength of this control is attributed to a regularization parameter (a Lagrangian multiplier).

5.10 The standard formulation

In brief, the regularization solution to the underdetermined least-squares problem ($n < m$) can be obtained as follows (Craig & Brown, 1986). Find the solution \mathbf{p} which minimizes the functional of the modified least-squares, or ill-posed problem:

$$\chi^2(\mathbf{p}) = \frac{1}{\sigma^2} \mathbf{r}'\mathbf{W}\mathbf{r} + \alpha \mathbf{p}'\mathbf{R}\mathbf{p} \quad (5.47)$$

where the residuals are $\mathbf{r} = \mathbf{y} - \mathbf{A}\mathbf{p}$, the regularization parameter is $\alpha > 0$, and \mathbf{R} is a symmetric and positively definite regularization matrix which controls the solution depending on the definition of the matrix. The equation of the minimum of the functional $\partial\chi^2(\mathbf{p})/\partial\mathbf{p} = 0$ is

$$\mathbf{A}'\mathbf{W}\mathbf{A}\mathbf{p} - \mathbf{A}'\mathbf{W}\mathbf{y} + \lambda\mathbf{R}\mathbf{p} = 0 \quad (5.48)$$

where $\lambda = \frac{1}{2}\alpha\sigma^2$. The solution is

$$\mathbf{p} = (\mathbf{A}'\mathbf{W}\mathbf{A} + \lambda\mathbf{R})^{-1} \cdot \mathbf{A}'\mathbf{W}\mathbf{y} \quad (5.49)$$

The standard methods to obtain the solution of the regularized inverse problems is a normal matrix inversion (Press et al. 1992). The LU or Cholesky decomposition can be used for the inversion since the matrix is not singular due to the presence of the non-zero regularization matrix \mathbf{R} .

Several types of the regularization matrices can be used. The simplest is the zeroth order regularization matrix $\mathbf{R} = \mathbf{I}$, i.e. the product $\mathbf{p}'\mathbf{R}\mathbf{p} = \mathbf{p}'\mathbf{p}$ is the minimization of the sum of squares of the solution. The first, second, etc. order regularization matrices are minimizing the total square of the first, second, etc. derivatives of the solution, $\mathbf{R} = \mathbf{H}$, where $\mathbf{H} = \mathbf{H}'_1\mathbf{H}_1$ or $\mathbf{H} = \mathbf{H}'_2\mathbf{H}_2$. The matrices \mathbf{H}_1 and \mathbf{H}_2 are called the difference matrices and are given in Press et al. (1992). For completeness, we have them also here.

The first difference matrix has the following elements:

$$(\mathbf{H}_1)_{(m-1)\times m} = \begin{pmatrix} -1 & 1 & & & 0 \\ & -1 & 1 & & \\ & & \cdots & & \\ & & & -1 & 1 \\ 0 & & & & -1 & 1 \end{pmatrix} \quad (5.50)$$

and its quadratic form is a three band-diagonal matrix:

$$(\mathbf{H}'_1\mathbf{H}_1)_{m\times m} = \begin{pmatrix} 1 & -1 & & & & & 0 \\ -1 & 2 & -1 & & & & \\ & -1 & 2 & -1 & & & \\ & & \cdots & \cdots & & & \\ & & & -1 & 2 & -1 & \\ & & & & -1 & 2 & -1 \\ 0 & & & & & -1 & 1 \end{pmatrix} \quad (5.51)$$

The second difference matrix has the elements:

$$(\mathbf{H}_2)_{(m-1) \times m} = \begin{pmatrix} -1 & 2 & -1 & & & & 0 \\ & -1 & 2 & -1 & & & \\ & & \dots & & & & \\ & & & -1 & 2 & -1 & \\ 0 & & & & -1 & 2 & -1 \end{pmatrix} \quad (5.52)$$

and its quadratic form is a five band-diagonal matrix:

$$(\mathbf{H}_2' \mathbf{H}_2)_{m \times m} = \begin{pmatrix} 1 & -2 & 1 & & & & & 0 \\ -2 & 5 & -4 & 1 & & & & \\ 1 & -4 & 6 & -4 & 1 & & & \\ & 1 & -4 & 6 & -4 & 1 & & \\ & & \dots & \dots & & & & \\ & & & 1 & -4 & 6 & -4 & 1 \\ & & & & 1 & -4 & 6 & -4 & 1 \\ & & & & & 1 & -4 & 5 & -2 \\ 0 & & & & & & 1 & -2 & 1 \end{pmatrix} \quad (5.53)$$

5.11 Regularized principal components solution

The regularization method was initially developed to solve the problem of the matrix inversion in ill-posed problems by means of biasing of its diagonal with a small amount of positive additive to improve the matrix condition number and therefore to avoid its singularity during the inversion.

Similarly, the singularity in the inversion is avoided when the solution is obtained with the principal components where the last $m - k$ presumably small singular values are eliminated or truncated according to the selected stopping criteria. Hence, the reduced principal components can be formulated as the solution to the minimization problem:

$$\chi^2(\mathbf{q}) = \frac{1}{\sigma^2} \mathbf{r}' \mathbf{W} \mathbf{r} \quad \text{subject to: } \mathbf{q}_i = 0 \quad \text{for } i = k, k + 1, \dots, m - 1 \quad (5.54)$$

i.e. it acts as a uniform cut-off filter to the vector \mathbf{q} . The regularization of singular linear systems stabilizes the solution by controlling its smoothness, i.e. it has filtering properties.

The solution \mathbf{p} of a singular linear system was expressed in terms of the orthogonal decomposition of the design matrix. Therefore, we can also formulate and solve the regularization problem in terms of the principal components. It has also an advantage that once the principal components solution is obtained, it can be further improved, in terms of smoothness, by means of the regularization. The use

of different regularization matrices and various regularization functionals allows to control the smoothness and the shape of the principal components in a number of different ways. This results in a number of solutions for the original parameters, and the choice of the correct solution has to be done from the specific formulation of the minimization problem.

The regularization problem can be formulated as follows: find the solution \mathbf{q} which minimizes the functional

$$\chi^2(\mathbf{q}) = \frac{1}{\sigma^2} \mathbf{r}'\mathbf{W}\mathbf{r} + \alpha \mathbf{q}'\mathbf{R}\mathbf{q}, \quad (5.55)$$

where the same notations are used as before, but the vector of the residuals is $\mathbf{r} = \mathbf{y} - \mathbf{T}\mathbf{q}$. The equation of the minimum of the functional $\partial\chi^2(\mathbf{q})/\partial\mathbf{q} = 0$ is

$$\mathbf{T}'\mathbf{W}\mathbf{T}\mathbf{q} - \mathbf{T}'\mathbf{W}\mathbf{y} + \lambda \mathbf{R}\mathbf{q} = 0, \quad (5.56)$$

where $\lambda = \frac{1}{2}\alpha\sigma^2$. The equation becomes

$$(\mathbf{C}^2 + \lambda \mathbf{R})\mathbf{q} = \mathbf{C}^2\hat{\mathbf{q}}, \quad (5.57)$$

where the normal principal solution is denoted as

$$\hat{\mathbf{q}} = \mathbf{C}^{-1}\mathbf{B}'\mathbf{V}\mathbf{y}. \quad (5.58)$$

The *regularized principal components* solution is

$$\mathbf{q} = (\mathbf{C}^2 + \lambda \mathbf{R})^{-1} \cdot \mathbf{C}^2\hat{\mathbf{q}}, \quad (5.59)$$

or, in the alternative form

$$\mathbf{q} = (\mathbf{I} + \lambda \mathbf{C}^{-2}\mathbf{R})^{-1} \cdot \hat{\mathbf{q}} \quad (5.60)$$

as a function of the regularization parameters λ . The dispersion of the regularized solution has become

$$\mathcal{D}(\mathbf{q}) = \sigma^2 (\mathbf{C}^2 + \lambda \mathbf{R})^{-1} \cdot \mathbf{C}^2 \cdot (\mathbf{C}^2 + \lambda \mathbf{R})^{-1}. \quad (5.61)$$

The parameter λ can be estimated in the first approximation from the equality of the two components of the sum:

$$\lambda = \alpha\sigma^2 = \frac{\text{tr}\mathbf{C}^2}{\text{tr}\mathbf{R}}. \quad (5.62)$$

Then, the parameter λ should be decreased until

$$\frac{1}{\sigma^2} \mathbf{r}' \mathbf{W} \mathbf{r} < \delta, \quad (5.63)$$

i.e. the weighted sum of the residuals reaches some level δ . Another method of choosing the regularization parameters is the cross-validation method and the L-curve criterion discussed in Fierro et al. (1997).

The regularized solution of the original parameters is as before

$$\mathbf{p} = \mathbf{D} \mathbf{q}. \quad (5.64)$$

The product in front of $\hat{\mathbf{q}}$ in Eq. (5.59) can be interpreted as a damping filter which suppresses the noisy components of the vector: the smaller the square of the singular values in \mathbf{C} , the stronger the dumping of the components of $\hat{\mathbf{q}}$. The degree of the suppression depends on the regularization parameter λ , and the shape of the filter is defined with the regularization matrix \mathbf{R} . Here we can apply different regularization matrices to \mathbf{q} to obtain a class of various regularized solutions to \mathbf{q} , \mathbf{p} , and to the fitting function $\tilde{\mathbf{y}}$.

5.11.1 Regularization of the principal components

I Minimum squares of \mathbf{q} , i.e. $\mathbf{R}=\mathbf{I}$. The solution to the problem is

$$\mathbf{q} = (\mathbf{C}^2 + \lambda \mathbf{I})^{-1} \cdot \mathbf{C}^2 \hat{\mathbf{q}}. \quad (5.65)$$

Since the inversion matrix is diagonal, the components of the vector are

$$q_k = \frac{c_k^2}{c_k^2 + \lambda} \cdot \hat{q}_k. \quad (5.66)$$

The filtering properties of this solution are obvious: the larger the parameter λ , the stronger the suppression of the noise in $\hat{\mathbf{q}}$ as the singular values $c_k \rightarrow 0$ along with their variances $\sigma_{q_k} \rightarrow 1/\lambda$. The variances of the solution are given by

$$\sigma_{q_k}^2 = \frac{c_k^2}{(c_k^2 + \lambda)^2}. \quad (5.67)$$

Fierro et al. (1997) investigated the filtering properties of this solution applied to the problem of total truncated least-squares.

H Maximal smoothness of the solution \mathbf{q} , i.e. $\mathbf{R}=\mathbf{H}$. The solution to the problem is

$$\mathbf{q} = (\mathbf{C}^2 + \lambda \mathbf{H})^{-1} \cdot \mathbf{C}^2 \hat{\mathbf{q}}. \quad (5.68)$$

At zero singular values $c_i \equiv 0$, where $i \geq r = \min(n, m)$, the submatrix of the inversion matrix becomes singular because the regularization matrix \mathbf{H} itself is not positively definite (i.e. $\mathbf{x}'\mathbf{H}\mathbf{x} > 0$ is not true for all \mathbf{x} , in particular, it is zero for the unity vector \mathbf{x}). The solution to \mathbf{q} should be found for the vector and the inversion matrix truncated to the rank r with zero singular values excluded from the inversion.

5.11.2 Regularization of the original parameters

The problem is to find the solution \mathbf{q} which minimizes the functional

$$\chi^2(\mathbf{q}) = \frac{1}{\sigma^2} \mathbf{r}'\mathbf{W}\mathbf{r} + \alpha \mathbf{p}'\mathbf{R}\mathbf{p} = \frac{1}{\sigma^2} \mathbf{r}'\mathbf{W}\mathbf{r} + \alpha \mathbf{q}'\mathbf{D}'\mathbf{R}\mathbf{D}\mathbf{q}, \quad (5.69)$$

i.e. controls the shape and the smoothness of the original parameters. The regularization matrix to \mathbf{q} is now $\mathbf{D}'\mathbf{R}\mathbf{D}$ and the solution to the problem is

$$\mathbf{q} = (\mathbf{C}^2 + \lambda \mathbf{D}'\mathbf{R}\mathbf{D})^{-1} \cdot \mathbf{C}^2 \hat{\mathbf{q}}. \quad (5.70)$$

I Minimum squares of \mathbf{p} , i.e. $\mathbf{R}=\mathbf{I}$. The solution to the problem is

$$\mathbf{q} = (\mathbf{C}^2 + \lambda \mathbf{I})^{-1} \cdot \mathbf{C}^2 \hat{\mathbf{q}} \quad (5.71)$$

the same as in Eq. (5.65).

H Maximal smoothness of the solution, i.e. $\mathbf{R}=\mathbf{H}$. The solution to the problem is

$$\mathbf{q} = (\mathbf{C}^2 + \lambda \mathbf{D}'\mathbf{H}\mathbf{D})^{-1} \cdot \mathbf{C}^2 \hat{\mathbf{q}}. \quad (5.72)$$

5.11.3 Regularization of the fitting function

Find \mathbf{q} which controls the smoothness of the fit weighted with the variances of the observations, i.e. which minimizes the functional

$$\chi^2(\mathbf{q}) = \frac{1}{\sigma^2} \mathbf{r}'\mathbf{W}\mathbf{r} + \alpha (\mathbf{V}\tilde{\mathbf{y}})' \mathbf{R} (\mathbf{V}\tilde{\mathbf{y}}) = \frac{1}{\sigma^2} \mathbf{r}'\mathbf{W}\mathbf{r} + \alpha \mathbf{q}' \cdot \mathbf{C}\mathbf{B}'\mathbf{R}\mathbf{B}\mathbf{C} \cdot \mathbf{q}, \quad (5.73)$$

where the orthogonal decomposition Eq. (5.24) of the fitting function was used. The regularization matrix to \mathbf{q} is $\mathbf{C}\mathbf{B}'\mathbf{R}\mathbf{B}\mathbf{C}$ and the solution to the problem is

$$\mathbf{q} = (\mathbf{C}^2 + \lambda \mathbf{C}\mathbf{B}'\mathbf{R}\mathbf{B}\mathbf{C})^{-1} \cdot \mathbf{C}^2 \hat{\mathbf{q}}. \quad (5.74)$$

I Minimum squares of the fit, $\mathbf{R}=\mathbf{I}$, then

$$\mathbf{q} = \frac{1}{1 + \lambda} \hat{\mathbf{q}}, \quad (5.75)$$

i.e. scaling the principal components changes the amplitude of the fit, hence its total square.

H Maximal smoothness of the fit, i.e. $\mathbf{R}=\mathbf{H}$, then

$$\mathbf{q} = (\mathbf{C}^2 + \lambda \mathbf{C}\mathbf{B}'\mathbf{H}\mathbf{B}\mathbf{C})^{-1} \cdot \mathbf{C}^2 \hat{\mathbf{q}}, \quad (5.76)$$

or, in a similar form

$$\mathbf{C}\mathbf{q} = (\mathbf{I} + \lambda \mathbf{B}'\mathbf{H}\mathbf{B})^{-1} \cdot \mathbf{C} \hat{\mathbf{q}} \quad (5.77)$$

5.12 Regularized differential solution

In the regularization functionals considered so far, the solution was formed in the arbitrary basis of all possible solutions. In the case $\mathbf{R} = \mathbf{H}$, the solution is smoothed by minimizing the differences of subsequent pixels and the differential nature of the matrix does not change the norm of the solution. This is not the case for the zeroth-order regularization matrix $\mathbf{R} = \mathbf{I}$, which minimizes the norm of the solution as the factor λ increases. This limits the application of the zeroth-order regularization to these data which are around zero, i.e. this regularization suppresses the wildly oscillating solutions around zero by controlling their amplitude. On the other hand, the use of the zeroth-order regularization is the most simple from the computational point of view, since it operates with diagonal matrices, and it has the simplest functional form which is easy to interpret in order to understand more complex problems. One of such insights is that the zeroth order regularization implicitly uses the *a priori* information about the solution assuming that it should be around zero. This leads us to the inclusion of the *a priori* information in a more general functional which will seek for the solution closest to any predefined function or any other deterministic information about the solution. The solution obtained with the known *a priori* information will be called the *regularized differential solution*.

This is, on the other hand, the basis for the solution to the pattern recognition problem where the goodness of the fit is used as a criterion to make the decision. The regularized differential solution is also widely-known as *Occam's inversion*.

The English fourteenth century philosopher William Occam wrote that *it is vain to do with more what can be done with fewer*, which has become known as Occam's razor - a fundamental tenet of modern science: hypotheses should be neither unnecessarily complicated nor unnecessarily numerous (Constable et al. 1987, who have first applied Occam's principle to the inversion).

The minimization functional in terms of the orthogonal decomposition is

$$\chi^2(\mathbf{q}) = \frac{1}{\sigma^2} \mathbf{r}'\mathbf{W}\mathbf{r} + \alpha (\mathbf{q} - \tilde{\mathbf{q}})'\mathbf{R}(\mathbf{q} - \tilde{\mathbf{q}}), \quad (5.78)$$

where $\tilde{\mathbf{q}}$ is an *a priori* known function. In the absence of the *a priori* information, the reduced principal components solution $\tilde{\mathbf{q}}$ can be used instead as the first guess to the solution. After derivations similar to the ones above, the minimization equation becomes

$$\mathbf{C}^2\mathbf{q} + \lambda\mathbf{R}(\mathbf{q} - \tilde{\mathbf{q}}) = \mathbf{C}^2\hat{\mathbf{q}} \quad (5.79)$$

and the solution is given by

$$\mathbf{q} = (\mathbf{C}^2 + \lambda\mathbf{R})^{-1} \cdot (\mathbf{C}^2\hat{\mathbf{q}} + \lambda\mathbf{R}\tilde{\mathbf{q}}), \quad (5.80)$$

where $\hat{\mathbf{q}}$ is the principal components solution as before.

I Let the regularization matrix be of zeroth order $\mathbf{R} = \mathbf{I}$. The components of the vector \mathbf{q} become

$$q_i = \frac{c_i^2 \hat{q}_i + \lambda \tilde{q}_i}{c_i^2 + \lambda}. \quad (5.81)$$

Once again, the vector of the reduced principal components solution has the elements:

$$\tilde{q}_i = \begin{cases} \hat{q}_i, & i = 0, 1, \dots, k-1 \\ 0, & i = k, k+1, \dots, m \end{cases} \quad (5.82)$$

therefore the regularized differential solution has the elements

$$q_i = \begin{cases} \hat{q}_i, & i = 0, 1, \dots, k-1 \\ \frac{c_i^2}{c_i^2 + \lambda} \cdot \hat{q}_i, & i = k, k+1, \dots, m. \end{cases} \quad (5.83)$$

That is exactly what we often need in practice: to keep the real part of the spatial harmonics of the solution and smooth its noisy tail with the chosen parameter λ . This solution, in turn, does not require an additional inversion of the matrix.

H In case we need to determine that solution whose residuals with respect to the *a priori* solution are smooth, the regularization matrix of the higher orders should be used: $\mathbf{R} = \mathbf{H}$. The solution becomes

$$\mathbf{q} = (\mathbf{C}^2 + \lambda \mathbf{H})^{-1} \cdot (\mathbf{C}^2 \hat{\mathbf{q}} + \lambda \mathbf{H} \bar{\mathbf{q}}). \quad (5.84)$$

The solution should be found for the truncated inversion matrix when $c_i > 0$ as it was discussed for Eq. (5.68).

Similar is the case when the reduced principal components solution in the original parameters space $\tilde{\mathbf{p}} = \mathbf{D} \bar{\mathbf{q}}$ is used as the *a priori* information:

$$\chi^2(\mathbf{q}) = \frac{1}{\sigma^2} \mathbf{r}' \mathbf{W} \mathbf{r} + \alpha (\mathbf{p} - \tilde{\mathbf{p}})' \mathbf{R} (\mathbf{p} - \tilde{\mathbf{p}}), \quad (5.85)$$

which has the solution given by

$$\mathbf{q} = (\mathbf{C}^2 + \lambda \mathbf{D}' \mathbf{R} \mathbf{D})^{-1} \cdot (\mathbf{C}^2 \hat{\mathbf{q}} + \lambda \mathbf{D}' \mathbf{R} \mathbf{D} \bar{\mathbf{q}}). \quad (5.86)$$

In the case $\mathbf{R} = \mathbf{I}$, the solution is the same as in Eq. (5.83), and for $\mathbf{R} = \mathbf{H}$ it is obtained by straightforward substitution of the regularization matrix.

5.13 Astronomical example

In this section we give an example of the deconvolution applied to real observations. We use the solar spectrum which was used in Sec. 2.1 for the comparison with the FTS solar spectrum convolved with the instrumental profile. Here, we use the same spectrum obtained with the high resolution 1st camera and the measured HeNe laser instrumental profile for deconvolution and compare it with the original FTS spectrum.

The process of deconvolution is demonstrated with a number of figures. The weighted design matrix of the convolution model Eq. (5.18) is constructed from the offset instrumental profile and the sampling matrix with the sampling rate $r = 1$, and is shown in Fig. 5.1.

The result of its SVD factorization (Eq. (5.23)) is shown in Fig. 5.2 where the two matrices \mathbf{B} and \mathbf{D} are given. One can see from the images that the orthogonal functions in the columns of the matrices have rather different spatial frequencies from the left to the right. The vector of singular values \mathbf{C} is given in Fig. 5.1. The solution of the least-squares problem results in the vector of the principal components \mathbf{q} (Eq. (5.29)), which is plotted in Fig. 5.3. The best solution was selected, in this particular study case, from the plot of χ^2_ν (Fig. 5.3), which describes the mismatch error of the fit. The number $k = 450$ of the first significant principal

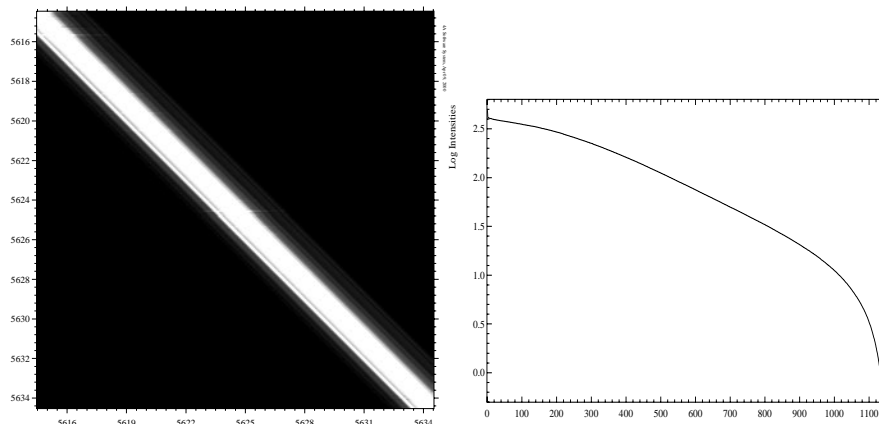


Figure 5.1: The image of the weighted design matrix \mathbf{VA} and the vector of singular values of the diagonal of \mathbf{C} in log scale.

components was selected where $\chi_\nu^2 = 1$, and all other components were set to zero. The particular solution in the original parameter space (the deconvolved spectrum) is obtained by using Eq. (5.30) and shown in Fig. 5.5. The covariance matrix for the selected solution is shown in Fig. 5.4, which gives us the degree of correlation between neighbouring pixels of the solution.

To ensure that the selected solution is indeed the best, we create an image (Fig. 5.4) of the family of solutions, where the deconvolved spectra are given in each row; the number of the reduced principal components increases from top to bottom. We see that the inclusion of the first few tens of the principal components gives a rough estimate of the spectrum, the further down the more details are reproduced, and towards the end the noise magnification occurs.

The deconvolved spectrum shown in Fig. 5.5 is overplotted with the FTS spectrum. The difference spectrum reveals a quite good agreement between the spectra.

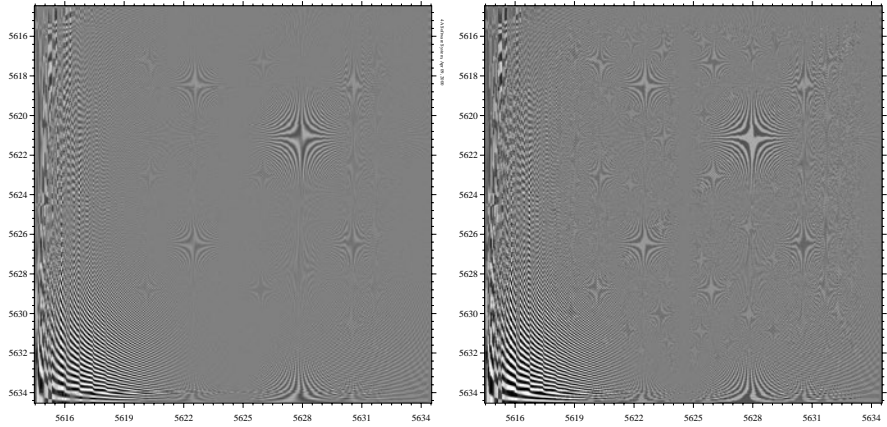


Figure 5.2: The image of the orthogonal matrices \mathbf{B} and \mathbf{D} of the weighted design matrix \mathbf{VA} .

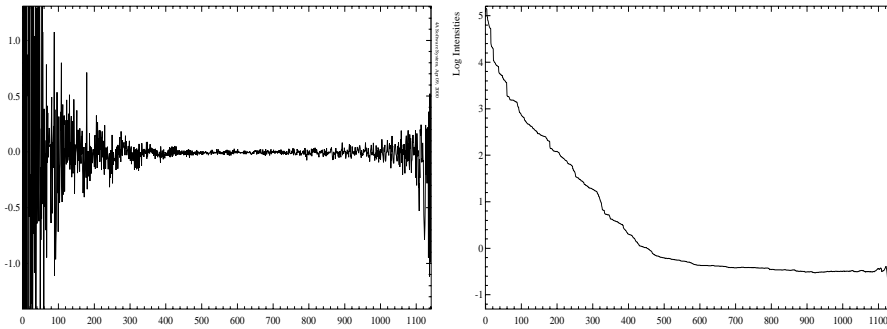


Figure 5.3: The vector of the principal components \mathbf{q} and the run of $\log \chi_{n-k}^2$ as a function of the number of principal components k . The best solution is at $k = 450$ when $\chi_{n-k}^2 = 1$.

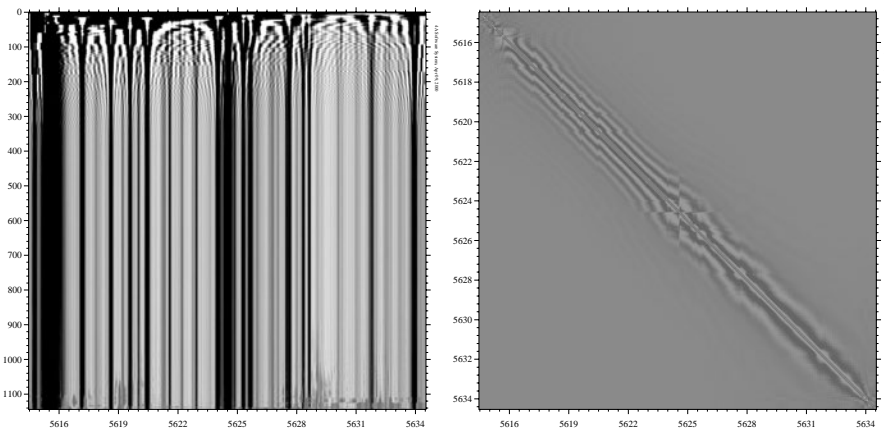


Figure 5.4: The image containing all principal solutions and the covariance matrix of the selected solution.

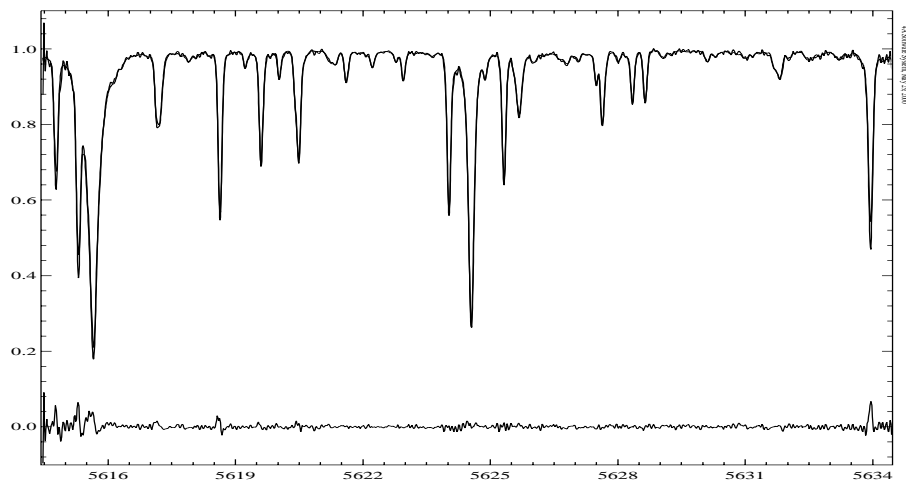


Figure 5.5: Comparison of the deconvolved spectrum and the FTS solar spectrum. The difference between the spectra is shown at the bottom. The rms of the difference is 0.4%.

Chapter 6

Line profile variations of the binary star α And

6.1 Introduction

α And (HR 15, HD 358) is a well-known peculiar bright double-lined binary system which has a mercury-magnesium primary component (B8 IVpMnHg). The primary component is the hottest ($T_{\text{eff}}=13800\text{ K}$) star among its class and shows abundances of Mn, Hg, P, and Ga which are 4–5 orders of magnitude higher than in the Sun (Ryabchikova et al. 1999). The spectral variability of the line profiles has been known for a long time. Rakos et al. (1981) reported the detection of variations in the UV Si II line profiles (1100–1300Å) with a period of around 3^h based on Copernicus observations. The variations of the continuum level in the lineless 3431Å region show a period of 23^h. The presence of such different variations complicates the explanation of the abundance anomalies by diffusion. In this study, we concentrate on the profile variability of the Hg II 3984 Å line which was earlier suspected to show some variations (Ryabchikova et al. 1999). The observations and subsequent analysis yield that the line indeed shows variations of its shape modulated by the stellar rotation, and the most plausible explanation is the presence of two strong Hg spots on the stellar surface.

6.2 Observations and data reduction

The observations of α And were obtained with the SOFIN spectrograph at the 2.56 m Nordic Optical Telescope (NOT) at Roque de los Muchachos Observatory, La Palma, Spain. A total number of 68 observations was obtained during 21 nights

in May, June, August, September, October, and November 1999 covering a time span of 180 days. The entrance slit width was set to $82 \mu\text{m}$ ($0''.6$ on the sky) providing the resolution element of 2 pixels FWHM and the resolving power of 80 000 at the spectral setting centred on 3984 \AA at order number 57. The spectra were recorded with an Astromed-3200 CCD camera providing a spectral coverage of 10 échelle orders (51–60) of about 30 \AA in length from 3766 \AA to 4450 \AA . Exposure time varied from 1 to 10 min depending on the seeing conditions, the signal-to-noise ratio achieved ranges from 80 to 350. Typically, one to three observations were made per night, within the time span of 2–3 hours given the unknown periodicity of the Hg II 3984 \AA line on short (hours) and long (days) time-scales. Each observation comprises one to three individual exposures to avoid possible CCD overflow in the reddest spectral orders.

The spectra were reduced with the 4A package. This involved standard procedures of bias subtraction, estimate of the variance of the flux, master flat field correction, scattered light subtraction with the aid of 2D-smoothing splines, spectral order definition, and weighted integration of the flux with cosmic spikes elimination. The wavelength calibration was done with the use of a ThAr comparison spectrum, each of them taken before and after each individual object exposure to eliminate any temporal changes in the spectrograph during an exposure. The wavelength solution incorporates Gaussian-centred positions, wavelength, and time of all detected spectral lines from the two images bracketing the stellar image. The wavelength for every pixel in the stellar spectrum is calculated for the time of its mid-exposure. The corrections of the spectra for the vignetting function and for the Earth's orbital motion constitute the final steps.

6.3 Radial velocity measurements

The Hg II 3984 \AA line shows variations of the line profile superimposed on the orbital motion of the primary stellar component due to the secondary. Hence, to remove the stellar radial velocity, we used relative measurements of the velocity with respect to the mean of the three neighbouring spectral orders 53 ($4264\text{--}4294 \text{ \AA}$), 54 ($4185\text{--}4214 \text{ \AA}$), and 55 ($4109\text{--}4138 \text{ \AA}$). The three orders show no conspicuous trace of the secondary stellar component. A cross-correlation technique was used to measure the velocity of each individual spectrum with respect to the mean with the velocity error determination involving variances of the pixel fluxes and the curvature of the cross-correlation peak. A polynomial of 4th degree was used to determine the centre and the curvature. Depending on the spectral order and the signal accumulated, the typical error is about $100\text{--}400 \text{ m s}^{-1}$.

The parameters of the orbit was previously published by Pan et al. (1992), Tomkin et al. (1995), and Ryabchikova et al. (1999). A Keplerian orbital fit (Ilyin 2000) to our measurements of the primary component is shown in Fig. 6.1 and the parameters obtained are given in Tab. 6.1. The limited time span of the observations

γ , m s^{-1}	5539 ± 96	T_{peri} ,	$2451\ 532.92 \pm 0.26$
K , m s^{-1}	32976 ± 118	T_{RVmax} ,	$2451\ 526.17 \pm 0.20$
P , days	96.884 ± 0.12	T_{conj} ,	$2451\ 533.79 \pm 0.23$
ω , degrees	77.5 ± 0.48		
e	0.5342 ± 0.0025	N_{free}	204
rms, m s^{-1}	651	χ^2_{ν}	10.5

Table 6.1: The set of the orbital parameters of the Keplerian fit. The moments of time are given as HJD.

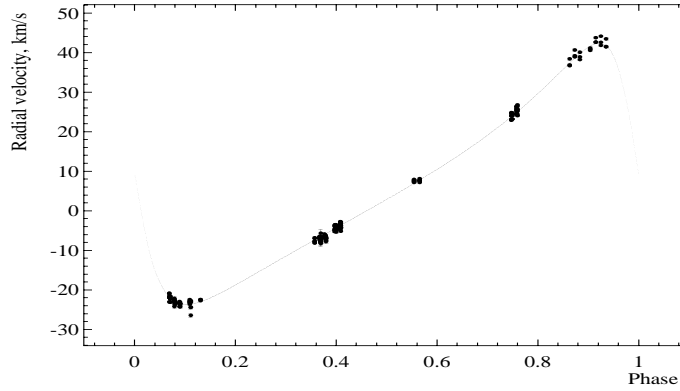


Figure 6.1: The orbital solution to the relative radial velocities of the primary component.

did not allow for an improvement of the period compared to that obtained by the other authors. The radial velocity of the order number 57 containing the line Hg II 3984 Å was removed by using the orbital fit.

6.4 The period of the line profile variations

The line of interest, Hg II 3984 Å, shows remarkable changes of its shape from night to night. In order to understand the behaviour of the process, we first investigated the periodogram of the line profile for each wavelength (pixel) of the profile. A Lomb-Scargle periodogram (Press et al. 1992) was calculated for an image of spectra resampled to the same stepsize in wavelengths, separately for

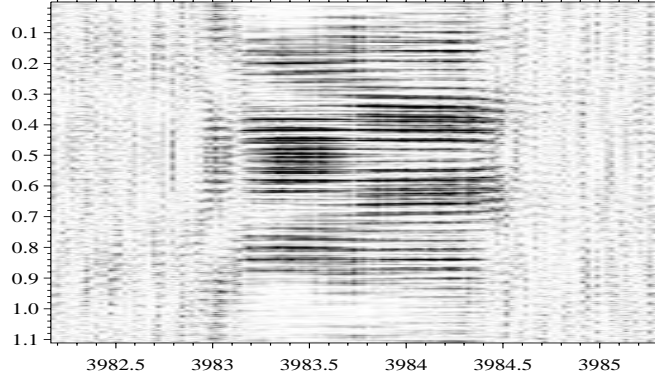


Figure 6.2: The gray-scale image of the periodogram of the Hg II 3984 Å line profile variations. The vertical axis units are frequencies in d^{-1} . The maximum corresponding to the rotational period $2^{\text{d}}38$ is at 0.42 d^{-1} .

each pixel. The periodogram image is shown in Fig. 6.2 and a sample of one column is given in Fig. 6.3. As we see from Fig. 6.3, the maximum is at 0.42 d^{-1} which corresponds to $2^{\text{d}}38$. This frequency is persistent over the whole line profile in Fig. 6.2, unlike the other peaks which are present only in parts of the profile. The associated window function of the observations is shown in Fig. 6.4, which peaks at the one day frequency.

The period can also be justified because it is very close to the rotational period of the main component of α And from the following considerations. Pan et al. (1992) derived the inclination of the orbit of $i = 105^{\circ}66 \pm 0^{\circ}22$; Ryabchikova et al. (1999) estimated $v \sin i = 52 \text{ km s}^{-1}$, and the stellar radius was estimated by Shallis et al. (1995) to $R = 2.7 R_{\odot}$. Given the parameters, the estimate for the rotational period is $P_{\text{rot}} = 2^{\text{d}}53 \pm 0^{\text{d}}05$ taking into account the error in the inclination and assuming that the error in the rotational velocity is 1 km s^{-1} .

To refine the period of the line profile variations estimated from the periodogram, we could use a cross-correlation of the individual profiles with respect to the mean spectrum and fit a model to the resulting changes (e.g. RVs). The disadvantage of this approach is that the cross-correlation technique assumes a similarity of the spectra being used which is not the case for this profile. Instead, we used a non-linear least-squares fit of a single period to all wavelength pixels of the profile versus time allowing to vary the offset, amplitude, and phase shifts along the line profile

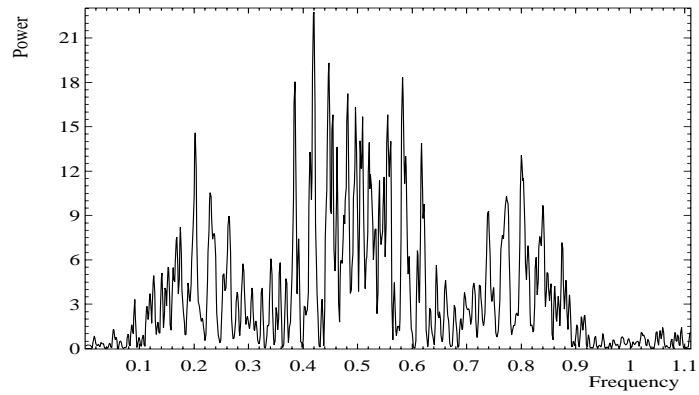


Figure 6.3: The periodogram of the line profile at $\lambda 3983.5 \text{ \AA}$. The frequencies are in d^{-1} .

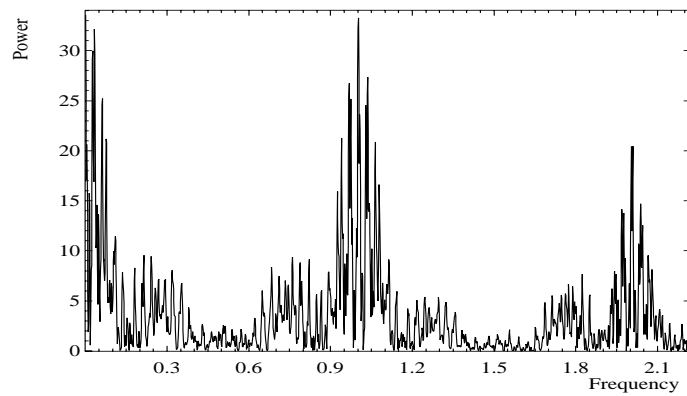


Figure 6.4: The window function of the observations calculated for an extended range of frequencies.

$$y_{ik} = b_i + a_i \cos 2\pi \left(\frac{t_k}{p} + \phi_i \right)$$

where y_{ik} is the image of spectra versus time t_k , $k = 1, 2, \dots, N$, and wavelength $i = 1, 2, \dots, M$. The free parameters along the profile are the offset (bias) b_i , the amplitude of variations a_i , and phase shifts ϕ_i , as well as the period of the variations p . The Levenberg-Marquardt method (Press et al. 1992) was used to find the parameters; the initial guesses for b_i , a_i , and ϕ_i were obtained from a linear least-squares solution for the period estimated from the periodogram

The period found by using this model is $P = 2^d 38257 \pm 0.00024$ with the goodness of fit values $\text{rms} = 0.0081$ and $\chi^2_{\nu} = 3.15$. The change of the bias, amplitude, and phase is shown in Fig. 6.5 together with their error bars. The image shows the profile phased with $t_k/p + \phi_i$. Clearly, two features separated by half a period at phases 0.3 and 0.8 are present. A more convenient image is shown in Fig. 6.6 where no phase shift was applied. The second, smaller feature is not so well shaped as compared to the other one, because the observations are not very dense at phases 0.6–0.8. The average within every 0.1 phase bin of the line profile is also shown in Fig. 6.7.

The time scale of the variability modulated by the stellar rotation and the different strengths of the two features rule out the hypothesis of non-radial pulsations for the star. The expected time scale of non-radial pulsations for this star could be about 10–20 hours as it is for the stars of similar type and spectral class. The most plausible interpretation, hence, is the presence of two HgII patches separated by 180° in longitude. According to the slope in the phase diagram, the latitudes of the two spots are almost the same.

The model could not completely describe the variability of the line profile, especially in the case of two spots. The spot configuration and their geometry should be included. The inconsistency of the model is indicated by the excess of χ^2_{ν} . Indeed, the model, aimed to find the period, is the simplest model one can apply without involving any stellar spot geometry configuration.

6.5 Variability of other spectral lines

To check whether spectral lines in other spectral regions of the échelle image show variability, we analyzed a variance spectrum for each spectral order with the orbital motion of the primary component removed. The result is shown in Fig. 6.8: the weighted average of the order is shown at the top of each panel and the spectrum of the standard deviation (magnified by a factor of 100) is at the bottom. No strong variations as much as in Hg II 3984 Å is seen. The excess variance at 4200, 4045, and 3849 Å was analyzed with the Lomb-Scargle periodogram as above. The most significant peaks at these regions are very close to the orbital period $96^d 8$

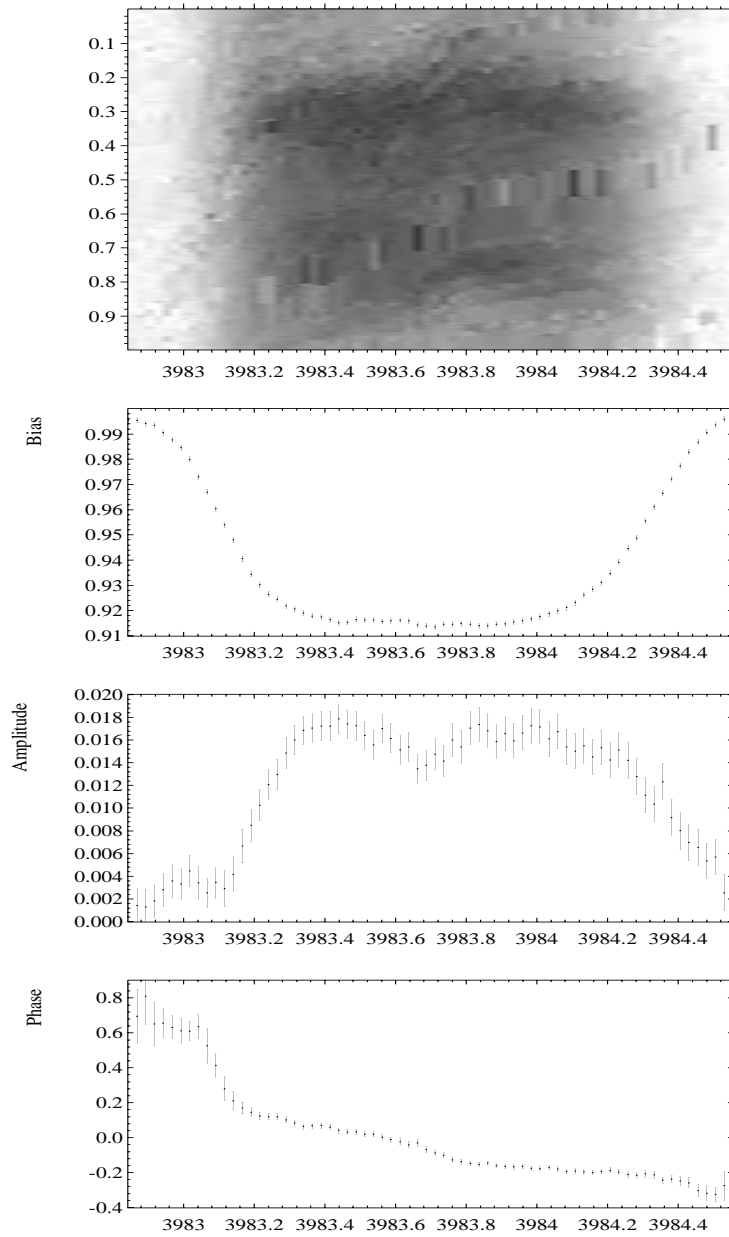


Figure 6.5: The image shows a phase diagram where the drift of the features in wavelength with phase is removed. The plots below are the intensity level, amplitude, and the phase shifts of the fit to the line profile.

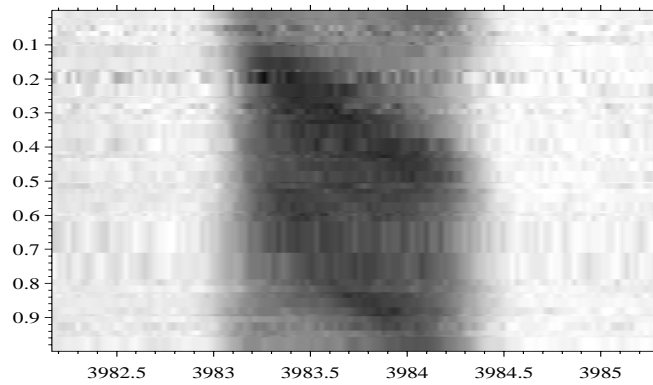


Figure 6.6: The line profile phased with the rotational period.

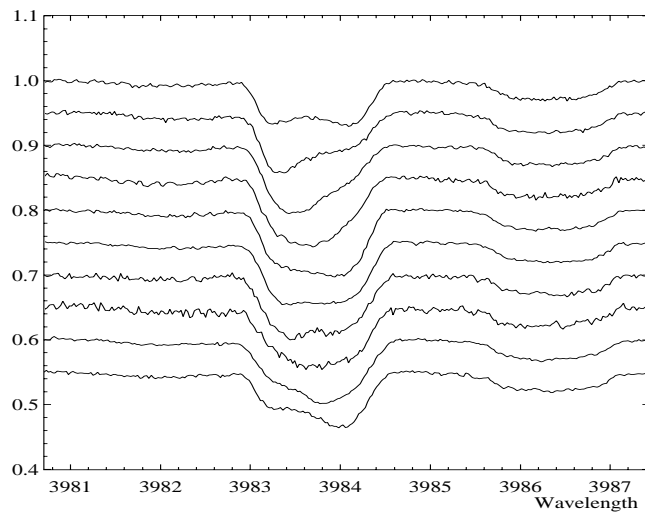


Figure 6.7: The individual spectra averaged in bins of the rotational phase $0.0 - 0.1, 0.1 - 0.2, \dots, 0.9 - 1.0$. The phase increases from top to bottom with the displacement 0.05 in intensities between spectra.

of the binary system, hence, these features, most likely, belong to the secondary component.

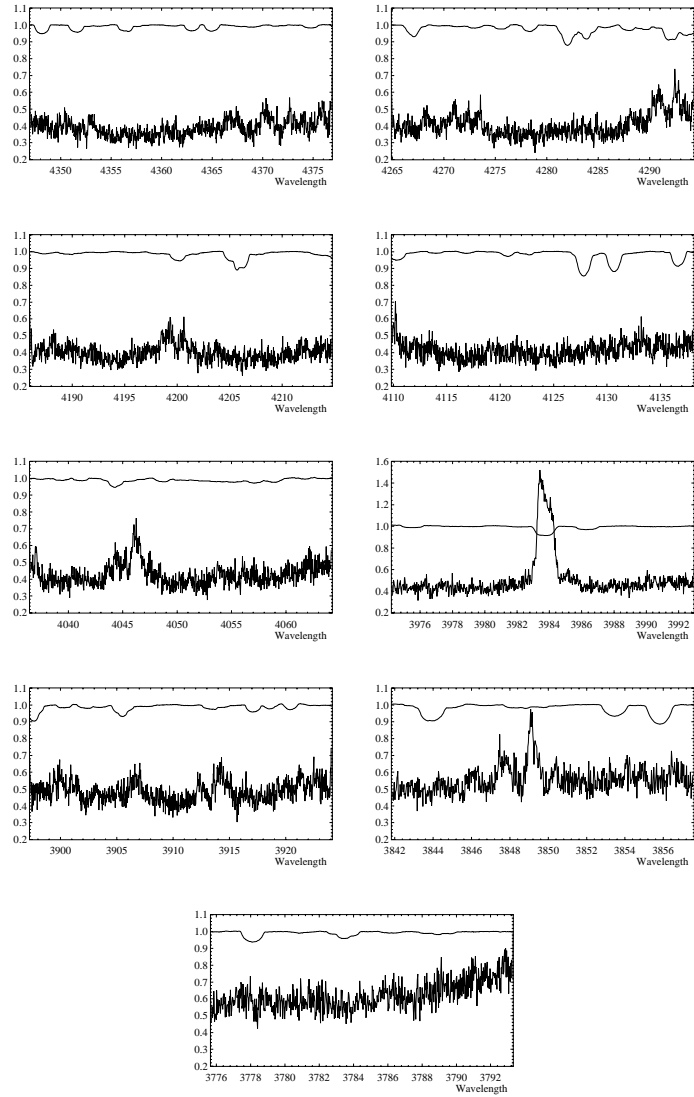


Figure 6.8: The averaged line profiles and the variance spectrum $\times 100$ for the échelle orders 52 – 60 left to right and top to bottom. The orders 57, 59, and 60 are truncated to avoid strong Hydrogen lines.

Appendix A

Reduction of SOFIN CCD échelle spectra: a user guide

A.1 Introduction

Unlike many other data reduction packages used in astronomy, where most of the procedures are built into a few integrated tasks, the 4A data reduction consists of a number of elementary steps. This approach is more flexible, it gives a better feeling for the data, but makes the whole procedure more complex.

In this chapter the description of the data reduction sequence is given from the point of view of a user, who is familiar to work with 4A. The detailed description of the 4A facilities is given in the "Reference Guide for 4A". The present user's guide gives the explicit commands in the normal sequence of échelle spectra reduction. The numerical parameters given in the guide are typical for SOFIN spectra but should be always adjusted for the particular set of data.

A.2 The essential steps of the data reduction

1. Removal of the electronic bias from the CCD images.
2. Variance estimation.
3. Correction for the master flat field.
4. Evaluation and removal of the scattered light surface from the images.
5. Definition of the spectral orders.

6. Weighted extraction of the spectral orders.
7. Correction of the object spectra for the vignetting function.
8. Background subtraction from the comparison spectrum images and spectral order extraction.
9. Wavelength calibration based on comparison and telluric lines.
10. Transformation of the object spectra into the wavelength scale.
11. The heliocentric and radial velocity transformations of the wavelength scale.
12. The continuum normalization of the object spectra.

A.3 Removal of the CCD bias

Overscan selection

For the object and flat field images use the overscan in columns at the bottom of the image, and for the saturated comparison spectra (especially in case of the 3rd camera images) use the overscan in rows on the right of the image. Display the image and position the marker box to the overscan area. Move the box to exclude the first 1–3 CCD edge pixels (they may create a problem later during filtration). Create a new record in the list of regions (**Process** menu): the extraction function should be `avrcols` for the overscan in columns, and `avrrows` for the overscan in rows. The template for the file name is `ccd00000.bss` or similar (Fig. A.1). Ensure that the record in the list is highlighted (and none of the others). Mark the images and extract the averaged biases (**FITS/Extract regions**). Repeat the region selection and the extraction for the images with the overscan in rows in necessary.

Bias smoothing

Smooth the averaged biases with a trimmed mean filter with the window parameters 33-5-5 (the window length is 33, and the highest/lowest 5 pixels are rejected). In case of apparent fringes in the bias (which is due to electrical interference on the CCD), use a filter with the smaller window size (11-3-3 for instance), or a Gaussian filter with the window length 3. Ensure that cosmic spikes do not affect the filtration.

Bias subtraction

Mark the smoothed biases and subtract them from the marked images (**Reduction/Bias removal**), where the option **column** applies to the overscan in columns. The resulting images will have the extensions **.col** and **.row**, respectively. Check that the averaged level in the overscan area of the subtracted images is around zero by inspecting the averaged cross-cut or making a histogram. Move the original images to the trash can (usually a **DUMP** subdirectory in the working directory).



Figure A.1: *Left*: An image with the selected overscan area in the CCD columns shown as the marker box. The position of the box is given in the highlighted record of the opened list of regions. *Right*: An averaged bias column containing a jump in it due to CCD electronics stabilization problem is shown. A trimmed mean filter is used to eliminate the readout noise and preserve the variations. The smoothed bias is subtracted from every column of the original image.

Trimming the images

Select an area with the marker box which is the same for all images: the region should exclude the two overscans and the first few edge pixels in columns and rows which are usually bad. Create a record in the list of regions with the template file name **ext00000.*** and the extraction function **SubImage**. Unmark the bias records. Mark the debiased images and extract the subimages. Move the original images **.col** and **.row** out of the working directory.

Estimation of the photon noise

Mark *all* debiased, trimmed images in the database and start the estimation of the photon noise command in **Process/Variances**. This operation will not change the image name but it changes its size. The number of dimensions of the images

is increased by one, and the third dimension is used to store the estimated variances. Check that the error bars appear in a cross-cut of the image when changing the plotting mode or by plotting the variances (**Scaling** menu). The procedure requires two FITS records to be present: **GAIN** is the CCD gain factor in e^-/ADU and **RON** is the readout noise in ADU. These records should be added to the FITS header, if not present.

A.4 Flat field correction

Master flat field normalization

The easiest way to calculate the trend in the master flat field is to use a trimmed mean filter with the window parameters 41-11-11. Unfortunately, for some dark pixels and dust particles the smoothed function may follow these features. Use a weighted spline with the smoothing factor ranging from 0.05 to 0.0001 and the rejection level ± 40 . In the particular case of camera 3 the parameters are $\pm 80/0.001$. Take the ratio between the original and smoothed images. If the normalized image is still disturbed in the areas around the dark pixels, then the pixels should to be masked out in the original image.

An alternative way to mask out the dark and sharp features is to use the clipping facility in **Process/Variances**: smooth the master flat with a median filter of 40–50 rows in length, sort the database, so that the original and smoothed records appear together, and clip the pixels which deviate from the median more than 40σ .

Division by the master flat

Mark the object and night flat field images and divide them by the master flat which creates `.dvd` files by default. Check the noise reduction: take a cross-cut of one column in the night flat field before and after the division. Calculate statistical parameters in a flat region of the spectrum: the **Stdev/Mean** ratio gives the measured signal/noise ratio. In case there is no such flat part in the spectrum, then smooth the spectrum by a spline, take the ratio, and measure the variance. The estimated signal/noise should be the same as the expected one, which is obtained by displaying the signal/noise spectrum (**Scaling/PlotSNR**). Move the original images `.col` and the master flats out of the working directory.

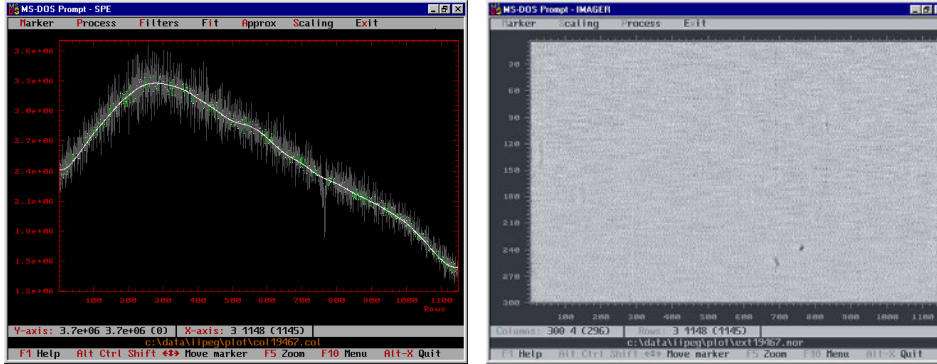


Figure A.2: *Left*: A column of the master flat field smoothed by a spline with the factor 0.01. In order to avoid sharp features, the sigma-clipping parameter is set to 40, hence the pixels deviating more than 40σ of the photon noise are rejected, which is, in this particular case, approximately the level of the CCD pixel-to-pixel noise. The clipped pixels are shown in gray. *Right*: The master flat field image after the normalization. The dark features are well preserved during the spline smoothing. The signal-to-noise ratio of the image is about 1100.

A.5 Scattered light removal

The scattered light surface is calculated in two steps: the surface of the interior of the spectral orders is approximated using a weighted spline in the clip-and-fit mode along rows, then the resulting surface is smoothed by a spline in columns.

1st camera. Smoothing in rows is done by a weighted spline with the smoothing factor 600 and the clipping parameters 2 (above) and 0 (below). The image extension could be set to `.pol`. Smoothing in columns is done with an unweighted spline of factor 600. The resulting image extension is `.bgn`.

2nd camera. Use a weighted spline in rows with the smoothing factor 10 and the clipping parameters 2 (above) and 0 (below). Use an unweighted spline in columns with the factor 1000.

3rd camera. Use a weighted spline in rows with the smoothing factor 1 and the clipping parameters 2 (above) and 0 (below) and an unweighted spline in columns with the factor 10.

A sometimes difficult problem for images of the 3rd camera is the undersampling effect in cross-dispersion which produces conspicuous ripples in the scattered light images in the dispersion direction. Subtraction of such a surface introduces the ripples into the stellar spectra. By using larger smoothing factors the ripples can be reduced, however, the scattered light level could still be overestimated.

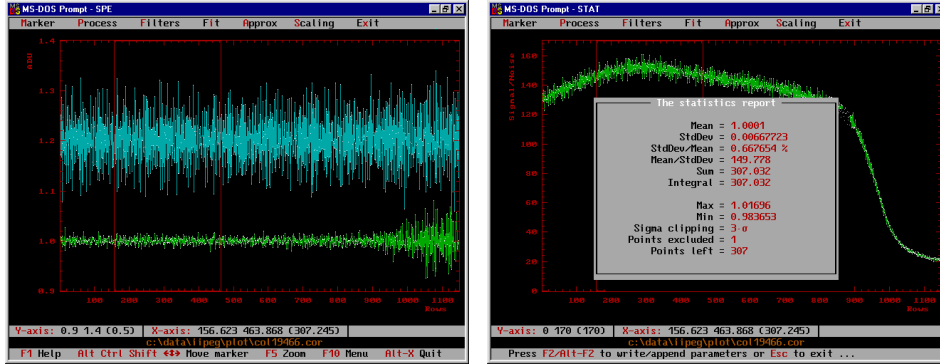


Figure A.3: *Left*: Decrease of the noise in the same column of the night flat field image before (upper, 6%) and after (lower, 0.6%) the master flat division. The columns are normalized to their trends. The amplitude of the high frequency spatial noise of the CCD used for the 2nd camera is about 6% rms and is constant for any illumination levels. The increase of the noise at the lower right is due to the lower light intensity level. *Right*: Check of the signal/noise ratio consistency by using the same single flat field column after the master flat correction. The plot shows the expected signal/noise ratio along the column (obtained with the Alt-N command in Scaling/Plot SNR). The opened statistical window gives a similar signal/noise (about 150) calculated for the selected region of the marker box. The shape of the signal/noise plot reflects the shape of the trend removed from the column and is due to order curvature.

In case the scattered light surface is disturbed by bad pixels in the original image, they can be masked out by clipping around a median image (filtered with window length 60 rows) with the clipping levels 100 (above) and 5 (below).

In the case when the ripples on the background are present due to electrical interference on the CCD, choose a small factor of the smoothing spline of the order of 1–5. This will allow to remove the wavy pattern from the image during the background subtraction.

Sort the database by file names and extensions and subtract the scattered light surfaces from the original images by using the pair operation command. The result should look like the left image in (Fig. A.4). The flat field corrected images .dvd and the background images can be moved out of the working directory.

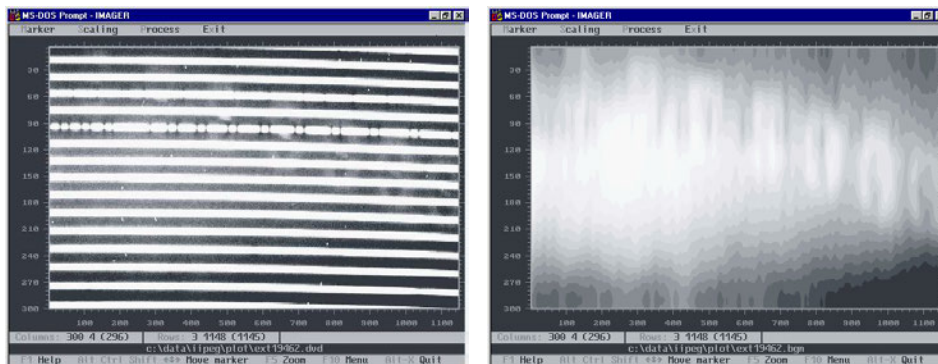


Figure A.4: *Left*: An image prior to the scattered light correction. A structure is seen between the spectral orders. *Right*: The scattered light surface of the image in the previous picture. The surface was obtained by approximation of the interorder gaps by a spline with the smoothing factor 10 and the rejection of pixels above 2σ along each row of the image in cross-dispersion. Then, the resulting image was smoothed along each column in the dispersion direction with an unweighted spline of the factor 100.

A.6 Definition of spectral orders

Order detection

Two parameters can be changed for the detection procedure: the median filter length and the detection probability. A filter length of 5 pixels is sufficient for most of the images; the more cosmic particles in the image the longer the filter. The detection probability should be 100% for the short 3rd camera and 1–10% for the others. The parameter can be as small as 10^{-20} in order to eliminate the detection of spurious spectral order-like features in the interorder gaps in the blue.

Mark the scattered light subtracted images and run the detection of orders program. The order definition polynomials are stored in separate binary (non-FITS) files with the extension `.spp`.

Order assignment

Displaying image by image, give the correct échelle order numbers to the spectral orders detected (Fig. A.6). For the 2nd camera the order numbers are increasing downwards (blue is at the bottom of the image) and the order number which is set in the program should be positive. For the 1st and 3rd cameras the order numbers are decreasing downwards (red is at the bottom of the image), therefore, the order number should be negative.

The order number can be identified from a known feature ($H\alpha$, for instance) and retrieved from the focal plane map program. If there is no such feature, the corresponding spectral order in the comparison spectrum can be identified (see wavelength identification, Sec. A.9.1) and the wavelength interval compared to the model of the focal plane.

If a number of images are very similar to each other (the same camera, the same spectral setting, and the spectral orders are approximately at the same positions during monitoring observations), the order assignment can be done with a single command. Firstly, give the order number to the first image, mark all images of the same kind, and secondly, run the `Reduction/Count orders` command from the database of images. The program will ask to point to the first reference image. Press `Enter` to start the procedure to enumerate the échelle order numbers for the marked images. Inspect the last images to ensure that the order numbers are correct (in case of a shift in the cross-dispersion).

A.7 Optimal extraction of spectra

Parameter adjustment

Check whether the default parameters are suitable for the images being processed. For a single object image run the weighted extraction with the spline smoothing parameter 0, which creates the unsmoothed version of the spatial profile image (`.sp`). Take a cross-cut of a column and check at what smoothing factor the spline fits the data. Use a weighted spline fit without clipping (both values are reset to zero). The higher the factor the less flexibility for the spline to fit small curvatures.

The default parameters for the smoothing factors are 10^9 for the 1st camera images, 10^8 for the 2nd, and 10^6 for the 3rd. The median filter length can be around 11 and the threshold is 3.

Inspection of the images

Mark the object and night flat field images and run the extraction procedure. It will create two new images for every original one. The first image contains the spatial profiles (`.sp`), which can be inspected and deleted. The extracted spectra and their variances are packed into one image with the column number equal to the order number (Fig. A.6). The cosmic spikes detected can be inspected in the original images: the hits are masked by changing the signs of their variances. The original images should all be inspected by displaying them with the `Marker/Masked pixels` switched on.

The scattered light subtracted images `.sub` can be moved out of the working directory.

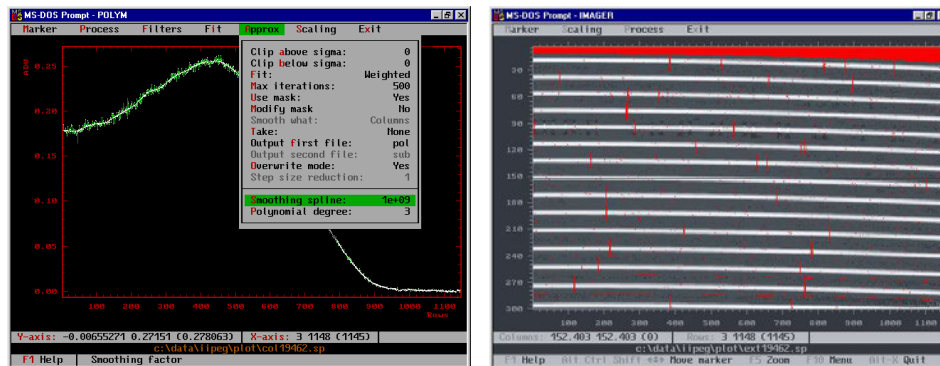


Figure A.5: *Left*: A column of the raw spatial profile of the image. A smoothing spline of factor 10^9 is used to obtain the filtered image of the spatial profile for the optimal extraction. *Right*: A smoothed spatial profile image with patches on it which are rejected from the spline approximation.

A.8 Correcting the shape of the spectra

Smoothing flat fields

Use a weighted spline with a smoothing factor 0.1 and possibly no clipping to smooth the images of the flat field packed spectra column by column (which are now the spectral orders). Any appearance of interference waves in the smoothed orders should be carefully inspected and compared with the corresponding spectra of the object. If the amplitude and phase of the waves are the same, then the interference can be removed from the object spectra. Otherwise, the effect can be enhanced several times. In this case, any interference appearance in the flat field spectra should be smoothed out by the spline approximation.

Normalize to the mean

In order to keep a similar number of ADUs in the object spectra, the smoothed flat fields can be approximated by a polynomial of zeroth degree in columns taking the ratio. The number of ADUs in the bluest orders of 3rd camera images is usually very low, which leads to singularities after the normalization. These orders can be patched by 1.

Reshaping the spectra

Mark the corresponding packed object images and divide them by the normalized flat fields. Check that the object spectra become flattened (Fig. A.7). This is often

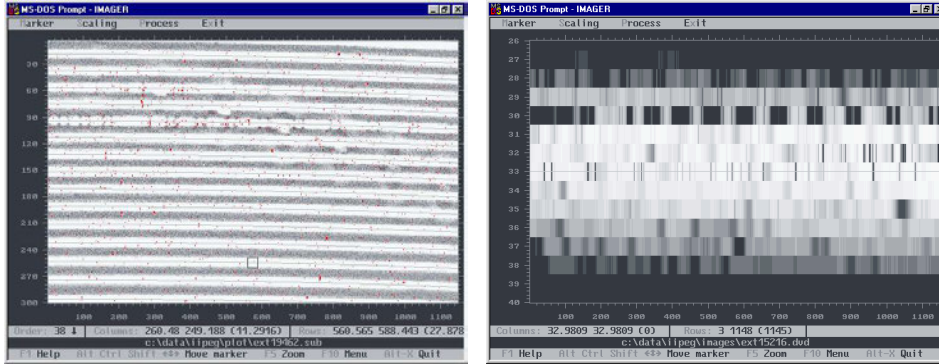


Figure A.6: *Left*: The image with the scattered light subtracted and used for the optimal extraction. After the extraction the detected cosmic spikes are marked on the image and seen as red patches after entering the mode `Alt-F6`. The amount of detected spikes is controlled by the sigma-clipping parameter of the optimal extraction algorithm. The curves of the located orders are shown. The bottom status bar indicates the échelle order numbers resulting after the orders assignment: the small marker box (in the third order from the bottom) indicates the position of the order number 38. *Right*: The image of the packed spectral orders after the optimal extraction.

not the case for 3rd camera spectra due to possible differences in the shapes of the object and flat field spectra. Remove all flat fields and the original object images from the working directory.

A.9 Wavelength calibration

Background removal

Mark all comparison spectrum images and apply a median filter with a window length of about 33 rows over one column and take the difference. This will create new images with the median background subtracted on a column by column basis. Delete the median images `.med` and move or delete the original images.

The other way to remove the background is to use a smoothing spline in the clip-and-fit weighted mode. One set of typical parameters are: the smoothing factor is 1, clip above is 2, and below is 10 (to avoid cold pixels due to overexposed comparison lines). Fit the images in columns and take the difference. This procedure works much slower than the median filtration, but gives a more smooth solution. The important advantage is that the median may slightly disturb the central position of a blend of lines which is wider than the filter length. On the other hand,

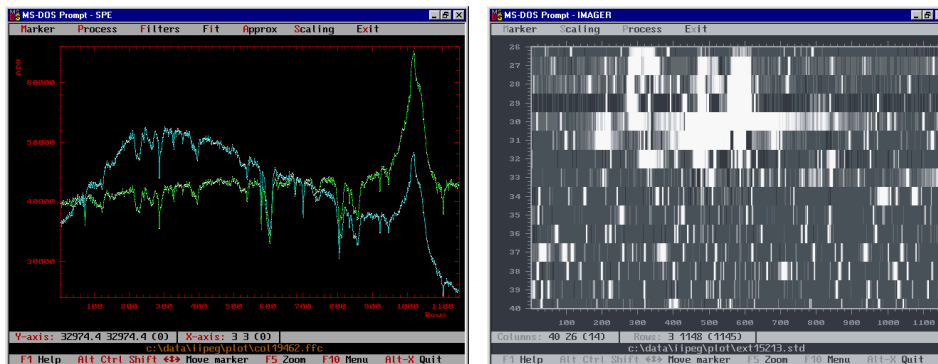


Figure A.7: *Left*: Two spectra are shown before and after the division by the night flat field which results in reshaping of the continuum. *Right*: An image of the packed spectral orders of the comparison spectrum image.

the smoothing spline may be sensitive to the clipping parameters in certain cases of line configuration, e.g. broad overexposed features, many cold pixels, etc. The remedy is to mask out these features by using a median filter and then to use the spline to fit and subtract the background. In the case of using the spline approximation, the images with the subtracted background should be unmasked (`Process/Variances/Absolute variances`) prior to any further operations.

Order tuning

The spectral orders for the comparison spectrum image should be taken from the nearest object or flat field images (`Reduction/Orders assignment`). The orders of these images may not be at the same positions as these of the comparison image. To align the orders to the actual position of the cross-profile, use the `Reduction/Orders tuning` command which works with marked images. For a single image the order tuning can be done from the imager program (`Process/Orders tuning`) with the input parameter which gives the initial offset of the orders in the cross-dispersion direction. For small offsets the parameter is zero. Run the procedure and check that the polynomial curves are adjusted to the centre of the spectral orders. The parameter equal to the distance between two adjacent orders in pixels will offset the polynomial curves down to the next spectral order. The actual offset of the curves is displayed in the bottom status bar.

In many cases, the strong overexposed spectral lines may disturb the order tuning procedure. The areas around strong lines can be masked out to be excluded from the fit: use the `Scaling/Mask region` command for individual images, or for a number of images it can be done from the list of regions: select the areas and use the function `MaskRegion`. Run the command `FITS/Extract regions` from the

database of images to mask out the selected areas of the marked images.

After the run, add two FITS records created by the program to the database: `CROFFS` is the offset of the spectral orders in cross-dispersion direction and `ECROFFS` is its error. Check that the orders in those images with large offsets are aligned correctly and their order numbering remains the same as in other images.

A.9.1 The wavelength solution of the comparison spectrum

Wavelength identification

For the first comparison spectrum in a series, do the standard extraction which creates an image of the packed spectral orders (Fig. A.7). Unpack the image to create a separate spectrum for each spectral order. Select an order with a known wavelength range and run the spectral line parameters program (`Reduction/Spectral lines/Line parameters`).

Locate the positions of spectral lines given so that at this stage the strongest lines should be selected for identification purposes. The location is simply done by putting the horizontal line of the graphical marker at the top of the background noise level and pressing `Enter`. All lines above the level will be detected and Gaussian profiles fitted to their profiles. The parameter given in `Graph/Gaussian zero` specifies the continuum level of the Gaussians. If the spectrum is used for the first time, the parameter is calculated as the median of the spectrum.

Select the catalogue of ThAr spectral lines named `tharkpno.cat`. Run the wavelength identification (`Table/Search in catalog`) by specifying the possible range of wavelengths for the blue end of the spectrum and the range of possible lengths of the order. The program gives a number of different identification choices: select the one with the maximal number of lines included. Select the `PosWav` function and make a fit. Exclude the most deviating points: use the `Ins` command to exclude a single line from the table, `Ctrl-Ins` to exclude a group of lines whose deviates are within the marker box positioned in the plot of residuals from the fit, or `Alt-E` to exclude a group of lines whose deviates are outside the marker box.

If the identification is wrong for all choices, i.e. the rms is too large everywhere, repeat the whole procedure with a reduced amount of lines included (delete all lines in the table, repeat the line locating with a raised level, so that only the strongest lines are selected).

A larger number of identified lines may result if the catalogue is changed to `tharpen.cat`. The wavelengths in the table are updated from the previous search by the command `pickup from catalogue`.

Make the fit and remove deviating points. The rms should be around 1–10 mÅ. Run the `Adjacent orders` command to calculate approximate dispersion curves for all adjacent orders of the image.

Run the line parameters program for every order in that image to locate the positions of spectral lines, and to pick up the wavelengths from the catalogue. Make the fit and exclude the most deviating points (this can be also done later during the global fit). The parameters of the spectral lines including their wavelengths are stored in separate binary (non-FITS) files for each spectral order with the extension `.slp`.

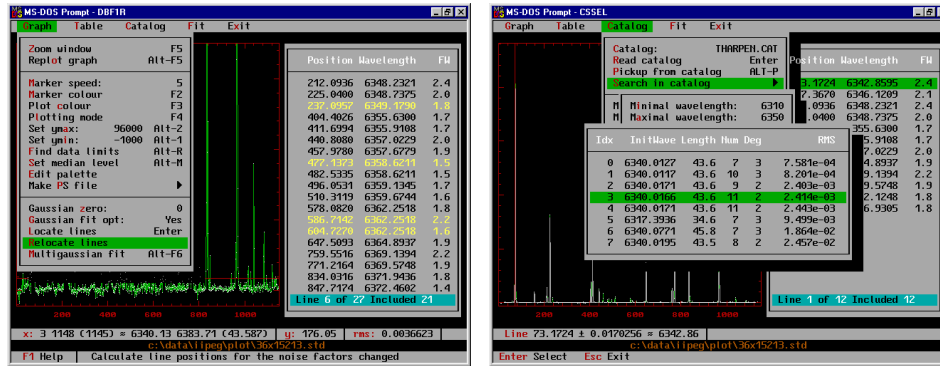


Figure A.8: *Left*: The comparison lines location window commands. The background level is set to zero, the horizontal marker box is positioned above the noise and used to locate all the lines above it. The wavelengths of the lines located are picked up from the catalogue of ThAr lines according to the dispersion polynomials obtained from another order. *Right*: The initial step to find the wavelength of the lines located. Give the approximate wavelength range of the blue (left) end of the spectrum and its length, obtained from the focal plane model of the spectrograph. A number of solutions is shown. The two solutions which have the same initial wavelength and most of the lines included (field Num) are the correct solutions.

Wavelength solution

Run the `ArcLamp solution` command on the packed comparison spectrum image with the wavelengths identified. It displays the global fit in two projections: along the central row and along the dispersion direction in wavelengths scaled to some reference order number. The default value for this order number is 40. Remove the most deviating points with the marker box. For a single comparison image, typical degrees (along time \times columns \times wavelengths), rms, and the fit error for the image centre are (the units are m s^{-1}):

Camera	Degrees	rms	FitErr
1st	$0 \times 1 \times 3$	70	10
2nd	$0 \times 2 \times 4$	120	15
3rd	$0 \times 1 \times 4$	600	35

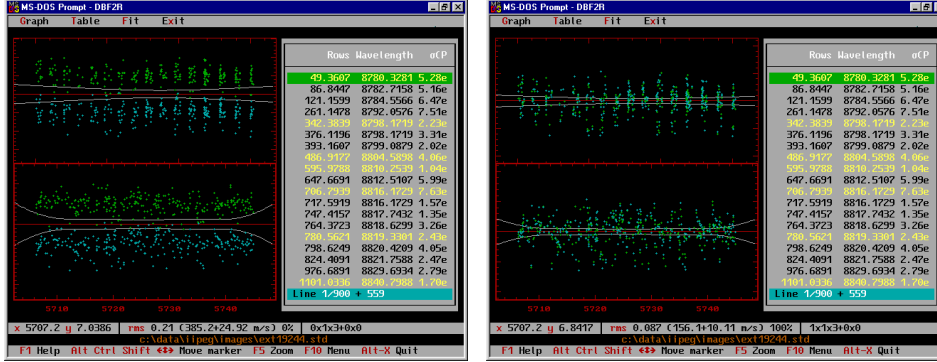


Figure A.9: *Left*: Two comparison spectra images, taken before and after the stellar exposure, are merged into the global fit. The effect of the drift of the line positions is seen. *Right*: The same as in the previous picture after the fit versus time is performed. The polynomial dispersion degree across the rows is 3, the divergence degree across the columns is 1, and in time it is 1 since only two images are involved.

Multiple wavelength identification

After the wavelength scale is established for a single reference comparison image, the wavelength scale can be established for all other images of the same spectral region and camera. Mark the images, run the `Coalign spectra` command, and point to the reference comparison spectrum. The parameter p specified in the menu command is the search interval ($\pm p$) of the cross-correlation range which is used to define the shift between the spectra.

When the procedure has succeeded, unmark all records selected, and run the comparison spectrum wavelength solution for each image to inspect the fit and to remove the most deviating points. The procedure creates a binary (non-FITS) file of the dispersion coefficients with the extension `.was`.

Multiple wavelength solutions

In order to exclude any effects related to the instability of the spectrograph, two or more comparison spectrum images which were taken before and after the object

exposure can be combined into one wavelength solution. Mark the images and run the program. Increase the time degree in the fit. Combination of two images should improve the rms of the fit by a factor $\sqrt{2}$. The dispersion coefficients for multiple comparison spectra are stored with the name of the first image.

Transformation into wavelength scale

At this stage the object spectra can be transformed into the wavelength scale if the telluric correction will not be applied. The wavelength scale command asks for the comparison image and the object image. The object spectra (orders) are transformed into the wavelength scale and stored as separate files.

A.9.2 The telluric wavelength solution

Creation of the telluric image

Mark the object images and apply a weighted spline with the smoothing factor 0.001 or so and the clipping factors 2 (below) and 0 (above) with taking the difference. The file extension for the difference could be `.atm`. The image with the difference should contain mostly the sharp telluric lines while the broader stellar lines are filtered out (see Fig. A.10).

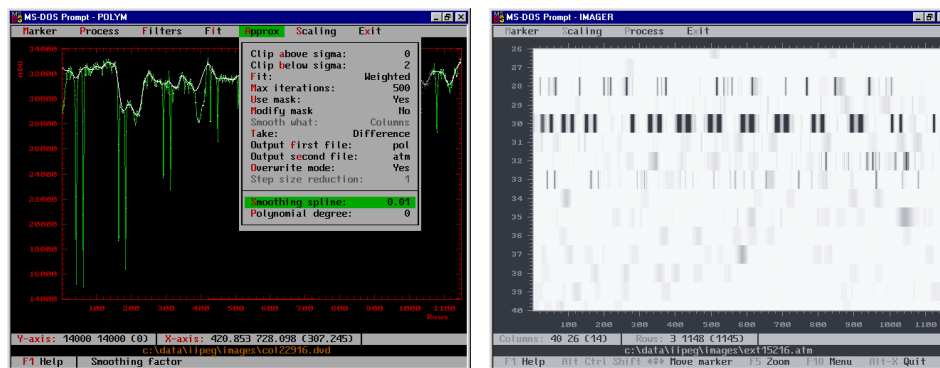


Figure A.10: *Left*: A spectral order with the telluric lines. The smoothness of the spline is adjusted to filter the stellar lines out and leave the sharp telluric features. The difference of the two constitutes the telluric image. *Right*: The telluric image of the packed spectral orders after most of the stellar lines were filtered out.

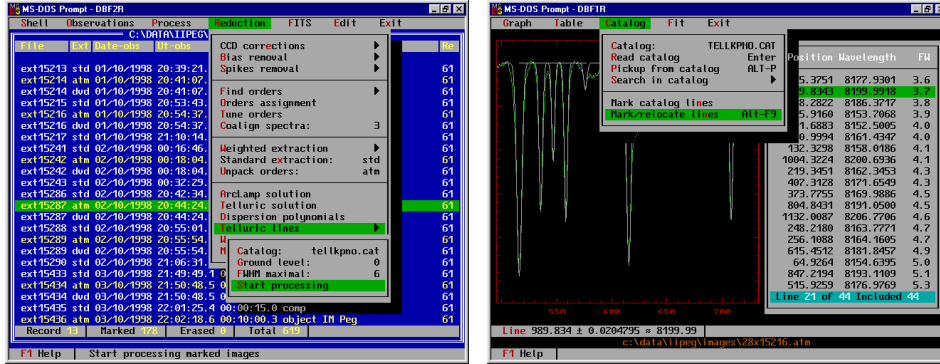


Figure A.11: *Left*: The telluric line identification menu. The selected images `.atm`, the catalogue specified, the continuum level, and the maximal FWHM of the lines to be selected are shown. *Right*: A fragment of the unpacked spectral order containing the identified telluric lines for the image. The same result can be obtained in order-by-order basis with use of the `Mark/Relocate lines` command as shown in the open menu.

Dispersion polynomials

In order to make the identification of the telluric lines possible, one should know the wavelength scale of the telluric images. Then, the program can guess the wavelength of the detected feature and find its exact wavelength from the catalogue of the telluric lines. The dispersion polynomials for each order and every telluric image have to be generated. Resort the database of images, so that they are in order of time. The comparison spectrum images should have the wavelength solution at the time. Run the `Reduction/Dispersion polynomials` command. In the bottom prompt line it will be indicated what to enter: first, it asks to point to the comparison spectrum, then to the telluric image. Once it is done, the program calculates the polynomials for every order of the image (binary non-FITF files with the extension `.fps`). Then enter the next pair of images. To exit from the cycle, press `Esc`. In case there are many telluric images and a single comparison spectrum, the procedure can be done faster by marking these images and entering only the comparison image.

Identification of the telluric lines

Open the menu of `Reduction/Telluric lines` and specify the catalog which should be `tellkpmo.cat`: a catalog of the telluric lines derived from the Solar Photographical Atlas. Specify the background level: the intensity of the continuum. In case the difference was taken, the continuum level is zero, in case of

normalization, it is one. Specify the maximal width of the telluric lines: the program will reject all choices where the identified line is broader than the specified limit. The value depends on the resolving power and a good choice is 2–6 pixels FWHM. Run the procedure for the selected packed images (see Fig. A.11).

In case of having some problems, the identification can be inspected for individual orders step-by-step (Fig. A.11). To do that, unpack the image of the telluric lines and run the spectral line parameters program for an order where telluric lines are expected (5000–9000 Å). The dispersion polynomials are assumed to be prepared. The presence of the dispersion polynomial is indicated in the status bar: as the graphical marker is moved it displays the approximate wavelength for the marker position. Change the catalog name to `tellkpno.cat`. Run the `Mark/Relocate` command, which makes an initial guess about the line positions based on the dispersion polynomials and the wavelength from the catalog, and relocates the lines to the observed spectrum (it means that it tries to fit a Gaussian to the spectrum at the position where the telluric line is expected). The lines wider than 3 pixels FWHM are deleted. Inspect the Gaussian fit for every line, make a dispersion curve fit, and remove the most deviating lines. A potential pitfall of the procedure is that the telluric lines can be confused with narrow stellar lines which is then difficult to recognize because of the small number of lines.

Make a global fit of the telluric image by using the comparison spectrum wavelength solution and remove deviates.

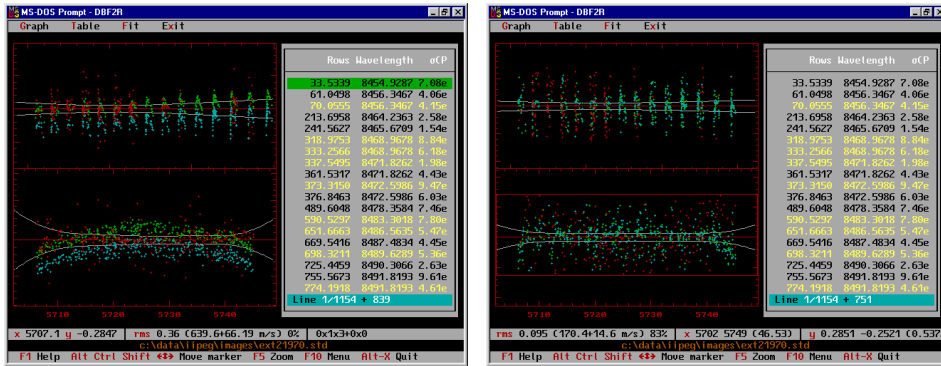


Figure A.12: *Left:* The combined fit of two comparison spectrum images and telluric lines prior to the exclusion of the deviating lines. In spite of the large scatter of the telluric lines, they tend to cluster around a curve. *Right:* The combined fit after the deviating points are excluded (with help of the exclusion out of the box command `Alt-E`).

Wavelength solution

The telluric solution allows to combine one or two comparison spectra and the telluric spectrum into one global fit. The final wavelength solution for the object images is made by obtaining the telluric solution for every observation. Mark the two (or the first, if the second does not exist) comparison images, run the `telluric solution` command, and select the record with the telluric image. Make the fit by F7. If there are many telluric lines, they should cluster around a curve. Many deviating lines can be excluded by using the `Alt-E` command, which excludes all lines outside of the marker box.

Change the degree in rows from 0 to 1 or higher and check the significance of the fit. In most cases, the zeroth degree in rows is enough. Use the `Partial` option to display the behavior of the telluric lines curve with respect to the comparison spectrum lines. This may help to estimate the degree of the telluric polynomial according to its curvature.

Typical values based on the telluric solution with two comparison images are (the degrees are along time \times columns \times wavelengths for the comparison image + columns \times rows for the telluric image; the units are m s^{-1}):

Camera	Degrees	rms	FitErr
1st	$1 \times 1 \times 3 + 0 \times 1$	80	12
2nd	$1 \times 2 \times 4 + 0 \times 1$	120	20
3rd	$1 \times 1 \times 4 + 0 \times 1$	800	75

The dispersion coefficients are written to a non-FITS file with the extension `.was` and the name of the telluric image.

Transformation into the wavelength scale

The transformation into the wavelength scale is done as described before in Sec. A.9.1, except that the “comparison spectrum image” is now the telluric image.

A.10 The wavelength transformations

Heliocentric correction

The correction for the Earth's motion is done by removing its projected radial velocity from the wavelength table of the marked spectra by running the `Remove Radvel` command in the `Reduction/Wavelength transformation` menu. Specify the output files extension, the usual choice is `.hw1`. The `Add error` option is

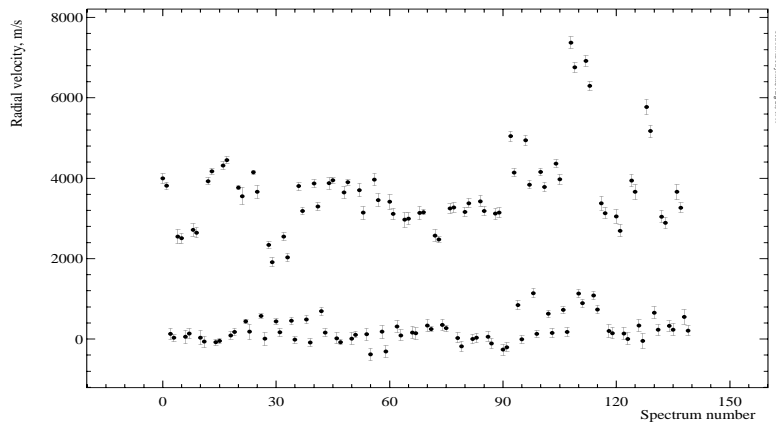


Figure A.13: The plot shows the effect of the slit error correction made for 35 different observations of Ap stars with the short 3rd camera. The vertical axis is the radial velocity in m s^{-1} and the horizontal is the spectrum number. Two water-line rich orders (#27 and #31) were used for the comparison. The upper part shows the comparison of telluric line positions with respect to an artificial spectrum prior to the correction. A significant offset of all spectra by about 0.7 pixels (the pixel size is 5400 m s^{-1}) is evident. The lower part shows the same comparison after the combined telluric solution was applied. The average level is 260 m s^{-1} . The most deviating points around spectrum number 110 are from a bright star which was difficult to centre accurately onto the slit. The larger the centring error, the larger the difference between the dispersion polynomials of the comparison spectrum and the telluric lines, which results in an incomplete correction of the slit effect.

irrelevant for this procedure. The velocity in m s^{-1} is given in the FITS header by `EARTHVEL` and used by the command as an argument.

If the record is not present, run the `Target` command on the marked spectra to update the header records. Spectra co-added prior to the heliocentric correction have no `EARTHVEL` parameter since the midpoint of the sum has changed. These spectra have to be updated with the `Target` procedure.

Stellar radial velocity rest frame

Similarly, the correction for the stellar radial velocity is done by removing the radial velocity given in a specified FITS keyword; again, a new copy of each spectrum with the specified extension, `.sw1` for instance, is created. The stellar velocity FITS record should be created with the `FITS/Modify record` command: enter

a name, select the floating-point format, and the value in m s^{-1} . The velocity will be removed from the spectrum, which means that the red-shifted spectrum should have the positive velocity. The procedure assumes that the spectra are in the wavelength scale. The wavelengths of the resulting spectra are modified for each pixel according to the velocity given: $\lambda_i \cdot (1 - v/c)$.

The **Add error** option requires also an error of the radial velocity to be given in the FITS record with the prefix **E** in the name of the velocity keyword name. The option affects the variance of the pixel intensities.

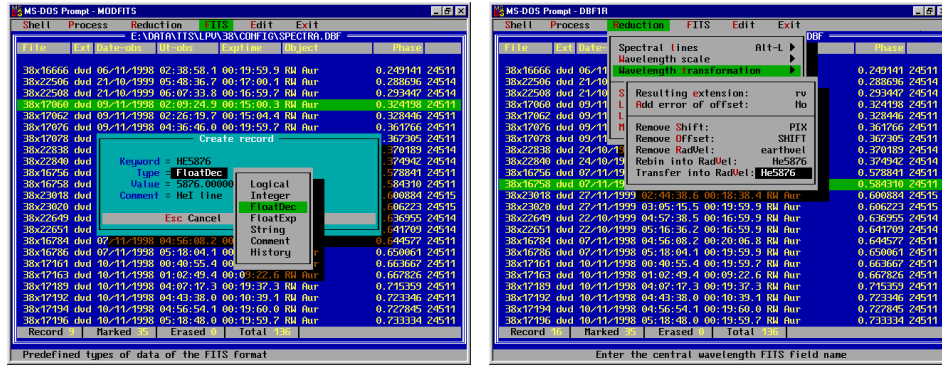


Figure A.14: *Left*: The picture shows how the FITS keyword is created to specify the wavelength of a line. The dialog window is opened from the **Fits/Modify record** menu. The new FITS record will be appended to the headers of the spectra marked in the database. *Right*: The transfer to radial velocity scale dialogue window: the resulting file extension **.rv** and the FITS keyword having the central wavelength as its value are shown.

Rebinning into radial velocity

The procedure rebins the selected spectra into the radial velocity scale with respect to the wavelength which is given in the specified FITS record. It creates a new set of spectra with the file extension as specified in the menu window. The spectra are rebinned into the same step size in the velocity scale ($\Delta\lambda \cdot c/\lambda = \text{const}$ for any part of each spectrum). The zero velocity corresponds to the reference wavelength chosen. The rebinning procedure involves modification of the spectrum intensities and their variances.

If the **Add error** option is set to **Yes**, then the error of the wavelength calibration is involved into the calculation of variances of rebinned pixels.

The rebinned spectra can be used for radial velocity measurements, although the

cross-correlation procedure itself does the rebinning from wavelength into radial velocities in case the `Radvel` option is selected.

Transformation into radial velocity

The procedure is similar to the previous one, but no rebinning of the intensities is performed. The wavelengths are transformed into radial velocity scale with respect to the central wavelength specified in the FITS record: $v_i = c \cdot \ln(\lambda_i/\lambda_c)$. This creates a table of unequally spaced radial velocities for each pixel of the spectrum. The spectra can be used for the cross-correlation in `Wavelength` rebinning mode.

The `Add error` option has no effect for this procedure.

Remove offset in pixels

The procedure removes an offset in pixel scale and the value is given in the specified FITS record. The type of the spectrum argument units is irrelevant. A shift by one pixel moves the pixel position (wavelength number, radial velocity, etc.) from the original pixel to the new one which results in the shift of the spectrum leftwards with respect to the original one. A shift by half a pixel results in a spectrum where the pixel position is calculated as the mean of the positions of two adjacent pixels.

The `Add error` option requires also an error of the offset given in the FITS record with the prefix `E` in the name of the pixel shift keyword name. The option affects the variance of the pixel intensities.

Remove offset in wavelength

The procedure removes the offset given in axis units which can be wavelength, radial velocity, pixels, etc. and results in modification of pixel positions.

The `Add error` option requires also an error of the offset given in the FITS record with the prefix `E` in the name of the wavelength offset keyword name. The variance of the pixel intensities are modified according to the error of the wavelength scale (if the spectra are in wavelength scale) and the error of the specified offset.

A.11 Continuum normalization

The continuum normalization involves fitting of a smoothing spline or a polynomial to the area of the spectrum free of spectral lines. The procedure requires the presence of the variances in the spectrum (to check it, display the spectrum and run the `plot variance` command in `Scaling` menu `Alt-V`). If for some reason no

variances are present, make an estimation of the photon noise or set the variances to a constant in the **Process/variances** menu of the database of spectra.

The fitting of the curve is done from the **Approximation** menu after the spectrum is displayed. Use the **Gray-** key to mask pixels out or **Gray+** key to unmask them (the masked pixels are displayed in a gray colour). The pixels around spectral lines being masked out are not used for the approximation. Open the **Approximation** window, select **Weighted** fit, set clipping levels to 0, and use a spline of the specified smoothing factor or a polynomial of a certain degree. Normally it generates a curve which overplots the spectrum. The curve is automatically saved as a FITS file with the same name as the spectrum and the extension **.pol**. The file is added to the last records of the database and can be retrieved later. In order to generate and display the normalized spectrum on the same screen, choose the option **Take as Ratio** by pressing **Enter** on the command (the other choices are **Difference** and **None**). Set up the output normalized spectrum extension in the **Second output** command, **.nor**, for instance. Run the fit again to generate the normalized spectrum which is automatically saved as a FITS file and added to the database. The option **Overwrite mode** prevents overwriting the existing file. For the trial-and-error fit, the option should be set to **Yes**. To display the normalized spectrum in the same scale as the original, change the scaling factor in **Scaling/Scale Alt-F7** to the value, for instance, of 1.5 times of the original spectrum intensity. The normalized spectrum will be enlarged on the screen by this amount (the spectrum intensities are not modified). Change the mask, if necessary, by (un-)masking pixels and tune the fit parameters to satisfy a good continuum.

To facilitate the continuum fitting, the procedure can be used in a clip-and-fit mode to exclude from the fit narrow absorption lines. Set the **Clip below** parameter to 2 and make a fit. The features below 2σ of the standard deviation are masked out and the remaining pixels are used for the fit. In fact, the procedure does a number of iterative fits subsequently masking the deviating pixels before it converges to the some curve. Broad spectral features or emission lines can be excluded from the fit by hand with the **Gray-** command. The resulting normalized spectrum inherits the position of the masked pixels (they are seen in gray): in order to restore them to the normal mode use unmask pixels commands **Gray +**, or it can be done at once for many spectra by running the **Process/Variances/Absolute variances** command from the database of spectra (the spectra should be marked).

The described normalization can also be done for many spectra at the same time if the spectra are similar to each other and cover the same wavelength range. The original marked spectra are displayed on the same screen with the **Alt-Enter** command and the above masking and normalization will be performed for every spectrum at the same time. A useful command for this purpose is **Fit/Transfer intervals**, which masks the same pixels of all displayed spectra as in the first spectrum. A non-interactive fit and continuum normalization can be also done for a number of marked spectra from the **Process/Polynomial approximation**

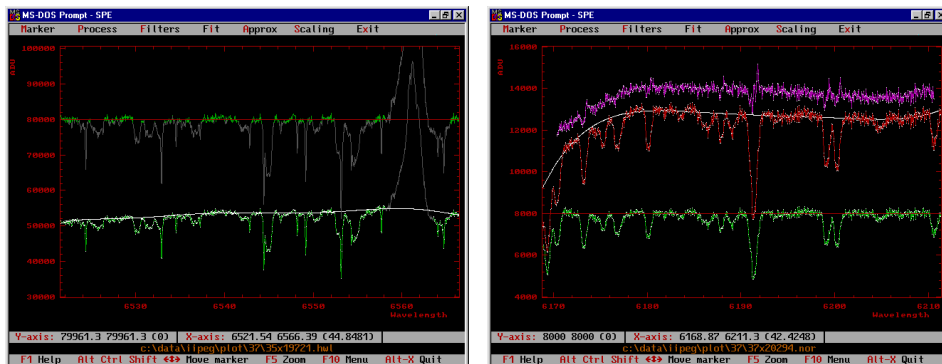


Figure A.15: *Left*: A spectrum normalized to a polynomial continuum of 7th degree in the fit-and-clip mode, where a 2σ clipping of features below the continuum was used. The normalized spectrum was scaled by 80000 to be seen in the same scale as the original spectrum. The broad emission $H\alpha$ line was excluded from the fit by masking its pixels out with the `Gray-` command, as it is seen on the original spectrum by its gray colour. *Right*: A spectrum normalized to the continuum of the mean spectrum. Shown are the original spectrum, the ratio to the mean spectrum (shifted upwards for clarity), and its polynomial curve which is the continuum. The resulting normalized spectrum is scaled to 8000. In the ratio, a number of small but sharp features are due to line profile variability.

menu of the database of spectra. This can be useful for a large amount of spectra when there are no features to mask out, or the masking has been done with the `Transfer intervals` command.

The other way to normalize to a continuum is to use a mean spectrum. Mark the spectra and make the sum. Fit a continuum to the summed spectrum and normalize to it. Divide every original spectrum by the normalized mean spectrum. In the ratio, non-variable spectral lines are canceled and the shape of the continuum remains. Fit a curve to these divided spectra: the `Take` option should be set to `None`, and all variable line features should possibly be masked out. Divide the original spectra by the smooth curves which constitutes the continuum normalization. To do that, sort the database of spectra by file name and extension, and use pair operations in the `Process` menu to divide the spectra. A synthetic spectrum can be used as well instead of the mean normalized spectrum.

A.12 Cross-correlation of spectra

Select the spectra being used for the cross-correlation and display them simultaneously on the screen with the `Alt-Enter` command. The first spectrum in the

sequence is used as the reference or template spectrum. To change the order of the sequence, use the **Alt-D** or **Alt-Q** commands from the **Marker** menu. The name of the first spectrum in the sequence is displayed in the bottom status bar. Exclude parts of the spectrum which should not be used for the cross-correlation, if necessary, by masking pixels out with the **Gray-** command. From the **Fit** menu run the cross-correlation **Alt-F10**. Three modes for the lag calculations are incorporated: pixels, wavelengths, and radial velocities. Change the calculation mode in the **Marker** menu, the range of the lags, and the number of points of the cross-correlation function within this range. The change of the number of points starts the calculations and displays the function. To interrupt the process press **Esc**.

The cross-correlation function in the pixel scale is calculated regardless of the axis units: the offsets are applied in index units. In the wavelength mode it is calculated in axis units, so that the spectra are rebinned with the same step size in axis units. In the radial velocity mode the spectra are rebinned with the same step size in velocity scale assuming that the axis unit is wavelength. The option **Marker/Position error** is used to take into account the error of the wavelength calibration when calculating the error of the cross-correlation offset determination and is used when the axis unit of the spectra is wavelength.

To find the position of the maximum use the commands from the **Search** menu: the **Parabolic search** command estimates the centroid position based on the curvature of the uppermost points, the **Polynomial fit** command estimates the position of the maximum from a polynomial fit of specified degree, and the **Gaussian fit** command is used to fit a Gaussian to the cross-correlation peak. The centroid positions can be determined individually by going through the table of the offsets, or it can be done at once for all of them. The table includes the following items: the spectrum file name, the position of the function maximum **Offset**, the error of the centroid determination **StdDev** (based on the variances of the spectra and the curvature of the peak), the amplitude of the peak **Rmax**, χ^2_ν of the regression fit **Rchi2**, and the two coefficients of the linear regression **c0** and **c1**. These parameters can be saved into the FITS header of the spectra from the **Exit** menu. Select a FITS keyword to be used to identify these parameters and save the changes. The keyword can be used later to shift the spectra, i.e. to remove the stellar orbital motion, from the **Wavelength transformation** menu as described above.

A.13 Decomposition of line profiles

Line profiles which consist of several components can be decomposed into a number of Gaussian profiles with the use of the **Reduction/Line parameters** procedure (**Alt-F7**). The decomposition function assumes that the variances of the spectrum are present. Enter the function and fit a number of Gaussians to the line profile: to fit an emission profile put the horizontal marker line above the continuum level and to fit an absorption line put the marker below. Press **Enter** to do the fit: firstly,

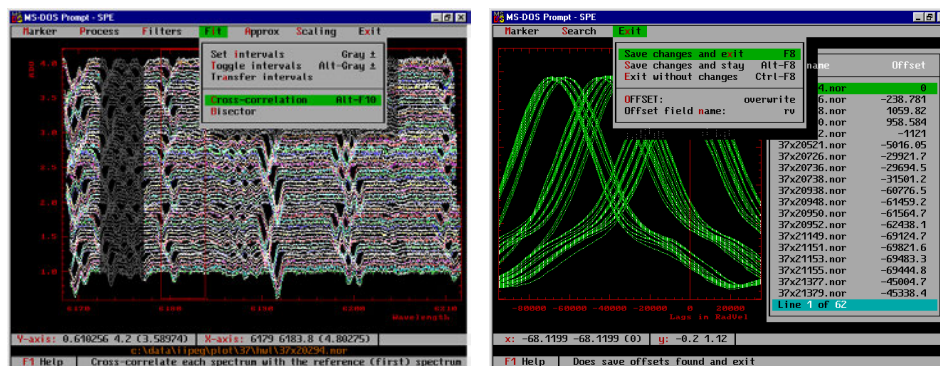


Figure A.16: *Left*: A number of spectra are displayed in order to run the cross-correlation facility. The spectra are offset in intensities and the reference spectrum is at the bottom of the plot. A number of pixels on the left are masked out to be excluded from the regression fit. *Right*: The cross-correlation function for every spectrum and the maximum positions displayed in the table. The lag unit is radial velocity. The opened **Exit** window shows the name of the FITS record used to save the offsets in the header of each spectrum.

it recognizes all the features above or below the marker level, and secondly, makes the fit of a Gaussian to each feature. To fit a Gaussian without minimization of the profile width, change the option in **Marker/Gaussian fit opt** to **No**. This creates a table of the initial guess for the multi-Gaussian fit. The table of the line parameters can also be edited using **Alt-F4**. To display the Gaussian profiles, press **F8** (**Table/Plot Gaussians**).

The next step is to tell the program which of these initial profiles will be used in the multi-Gaussian fit: being in the table of lines press **Alt-I** (**Table/Select line**). A line with the table record in pink indicates that it is included into the fit. In the same way a line can be excluded from the fit. Press **Alt-F6** (**Marker/Multi Gaussian fit**) to start the fit: it opens a window where the current parameters of the Gaussian profiles and the convergence of the fit are displayed. One of the parameters is **DeltaMax** which is the tolerance interval. The fit has converged when the tolerance is less than 10^{-11} . If the fit has converged, as indicated with a message at the bottom status bar, press **Enter** to accept the newly fitted parameters. By pressing **Esc**, the newly found parameters of the fit are discarded. If the fit has not converged, it indicates that the initial guess is too bad: try to fit new Gaussian profiles which describe the components in a more close way.

To display the sum of the decomposed Gaussians, use **Alt-F8** (**Table/Plot sum**). The individual Gaussians can be subtracted from the line profile with **Alt-S** (**Table/Subtract Gaussians**), the line record in the table is displayed in red.

It is useful in some cases, to subtract some of the components and do the fit to the remainders. In this case the subtracted profiles have to be excluded from the fit. The resulting composition of the Gaussians can be written into a separate file by the `Table/Write Gaussians` command. The variances of the function are the errors of the multi-Gaussian fit. It is also possible to modify the original line profile by subtracting one or several components: on exit (`Alt-X`), the program asks whether to save the changes (press `Enter`) or not (press `Esc`). Subtraction of a component changes the variances of the initial line profile.

The resulting parameters in the table from the multi-Gaussian fit are the line position and its error (`Position` and $\sigma(\text{Pos})$), the amplitude and FWHM of the Gaussian (`Intensity` and `FWHM`), and the equivalent width with its error (`EWG` and $\sigma(\text{EWG})$). The table of the parameters can be exported into a text file by using the `Table/Print table` command.

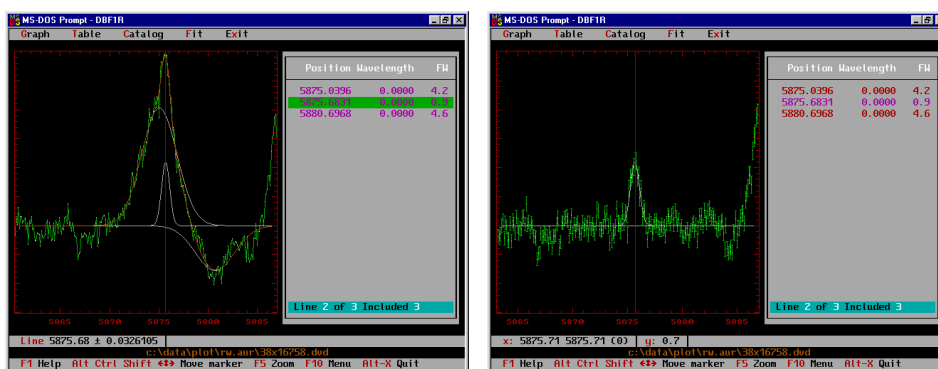


Figure A.17: *Left:* A line profile decomposed onto three Gaussians. The line profile, the individual components, and their sum are shown. *Right:* After the fit, the two broad components are subtracted leaving the narrow component. The plotting mode is changed to show the error bars of the pixels.

References

- Allen, C.W. 1976, *Astrophysical Quantities*, 3rd ed. (University of London, Athlone: London)
- Barlow, M.J., Crawford, I.A., Diego, F., Dryburgh, M., Fish, A.C., Howarth, I.D., Spyromilio, J., Walker, D.D. 1995, *MNRAS* 272, 333
- Berdyugina, S.V. 1998, *A&A* 338, 97
- Berdyugina, S.V., Berdyugin, A.V., Ilyin, I., Tuominen, I. 1998, *A&A* 340, 437
- Blades, J.C., Wynne-Jones, I., Wayte, R.C. 1980, *MNRAS* 193, 849
- Bloom, A.L. 1966, *Appl. Opt.* 5, 1500
- Brown, T.M. 1990, in: *CCDs in Astronomy* (ed. G.H.Jacoby), *PASPC* 8, p. 335
- Bukach, A.B., Zlotnikov, L.F. 1995, *Bull. Crimean Astrophys. Obs.* 89, 138
- Collier Cameron, A. 1992, in: *Surface Inhomogeneities on Late-type Stars* (eds. P.B.Byrne & D.J.Mullan), (Springer-Verlag: Berlin) p. 33
- Collier Cameron, A. 1999, in: *Precise stellar radial velocities*, *IAU Coll.* 170 (eds. J.B.Hearnshaw & C.D.Scarfe), *PASPC* 185, p. 233
- Constable, S.C., Parker, R.L., Constable, C.G. 1987, *Geophysics* 52, No. 3, 289
- Craig, I.J.D., Brown, J.C. 1986, *Inverse Problems in Astronomy* (Hilger: Bristol)
- Diego, F., Fish, A.C., Barlow, M.J., Crawford, I.A., Spyromilio, J., Dryburgh, M., Brooks, D., Howarth, I.D., Walker, D.D. 1995, *MNRAS* 272, 323
- Donati, J.-F., Semel, M., Carter, B., Rees, D.E., Collier Cameron, A. 1997, *MNRAS* 291, 1
- Donati, J.-F., Semel, M. 1990, *Sol. Phys.* 128, 227
- Dravins, D. 1993, "The Impact of Long-Term Monitoring on Variable Star Research", *NATO workshop* (eds. C.Sterken & M.de Groot)

- Dunteman, G.H. 1989, *Principal components analysis* (SAGE: Newbury Park, California)
- Fierro, R.D., Golub, G.H., Hansen, P.C., O'Leary, D.P. 1997, *SIAM J. Sci. Comput.* 18, No. 4, 1223
- Golub, G.H., van Loan, C.F. 1980, *SIAM J. Numer. Anal.* 17, 883
- Golub, G.H., van Loan, C.F. 1989, *Matrix computations* (Johns Hopkins University Press: Baltimore)
- Gosset, E., Magain, P. 1993, *ESO Messenger* 73, 13
- Gray, D.F. 1986, in: *Instrumentation and Research Programmes for Small Telescopes*, IAU Symp. 118 (eds. J.B.Hearnshaw & P.L.Cottrel), (Reidel: Dordrecht), p. 401
- Gray, D.F. 1988, *Lectures on spectral-line analysis: F, G, and K stars* (Arva: Ontario)
- Gray, D.F. 1992, *The observation and analysis of stellar photospheres*, 2nd ed. (Cambridge University Press: Cambridge)
- Griffin, R.F. 1969, *MNRAS* 143, 319
- Hamuy, M., Walker, A.R., Suntzeff, N.B., Gigoux, P., Heathcote, S.R., Phillips, M.M. 1992, *PASP* 104, 533
- Hansen, P.C. 1997, *Rank-Deficient and Discrete Ill-Posed Problems: Numerical Aspects of Linear Inversion* (SIAM: Philadelphia)
- Hocking, R.R. 1976, *Biometrics* 32, 1
- Ilyin, I.V. 1995, *Bull. Crimean Astrophys. Obs.* 89, 127
- Ilyin, I.V. 1996, *Remote control observations with the SOFIN spectrograph and reduction of CCD échelle spectra*. Licentiate Dissertation, University of Oulu
- Ilyin, I.V. 2000, *Numerical methods of data analysis – A collection of notes to 4A algorithms*. (Unpublished)
- Jackson, E. 1991, *A User's Guide to Principal Components* (Wiley: New York)
- Janesick, J. 1997, *SPIE* 3019, 70
- Jorden, P., Deltorn, J.-M., Oates, P. 1993, *RGO Gemini* 41, 1
- Kendall, M. 1975, *Multivariate analysis* (Griffin: London)
- Kurucz, R.L., Furenlid, I., Brault, J., Testerman, L. 1984, *National Solar Observatory Atlas No. 1* (Tucson, NSO)

- Lagutin, A.F. 1995, *Bull. Crimean Astrophys. Obs.* 89, 127
- Lang, K.R. 1974, *Astrophysical Formulae* (Springer-Verlag: Berlin)
- Lauer, T.R. 1999, *PASP* 111, 227
- Melles Griot Co. 1988, *Optics Guide* 4
- Neumaier, A. 1998, *SIAM Rev.* 40, 636
- Pan, X., Shao, M., Colavita, M.M., Armstrong, J.T., Mozurkewich, D., Vivekanand, M., Denison, C.S., Simon, R.S., Johnston, K.J., 1992, *ApJ* 384, 624
- Petrov, P.P., Zajtseva, G.V., Efimov, Yu.S., Duemmler, R., Ilyin, I.V., Tuominen, I., Shcherbakov, V.A. 1999, *A&A* 341, 553
- Piskunov, N.E., Tuominen, I., Vilhu, O. 1990, *A&A* 230, 363
- Plachinda, S.I., Tarasova, T.N. 1999, *ApJ* 514, 402
- Press, W.H., Teukolsky, S.A., Vetterling, W.T., Flannery, B.P. 1992, *Numerical Recipes*, 2nd ed. (Cambridge University Press: Cambridge)
- Pronik, V.I. 1995, *Bull. Crimean Astrophys. Obs.* 89, 111
- Rakos, K.D., Jenkner, H., Wood, J. 1981, *A&AS* 43, 209
- Rucinski, S. 1999, in: *Precise stellar radial velocities*, IAU Coll. 170 (eds. J.B.Hearnshaw & C.D.Scarfe), *PASPC* 185, p. 82
- Ryabchikova, T.A., Malanushenko, V.P., Adelman, S.J. 1999, *A&A* 351, 963
- Schroeder, D.J., Hilliard, R.L. 1980, *Appl. Opt.* 19, 2833
- Shallis, M.J., Baruch, J.E.F., Booth, A.J., Selby, M.J. 1995, *MNRAS* 213, 307
- Shcherbakov, A.G., Shcherbakova, Z.A., Ilyin, I., Tuominen, I. 1995, in: *New developments in array technology and applications* (eds. D.Philip, K.A.Janes, A.R.Upgren), *IAU Symp.* 167
- Siegman, A.E. 1971, *An introduction to lasers and masers* (McGraw-Hill: New York)
- Stoer, J. 1993, *Introduction to numerical analysis* (Springer: New York)
- Svelto, O., Hanna, D.C. 1989, *Principles of Lasers*, 3rd ed. (Plenum Press: New York)
- Taylor, B.J. 1984, *ApJS* 54, 259

- Thorne, F.J., Jorden, P.R., Waltham, N.R. 1987, Proceedings of ESO-OHP workshop "The Optimization of the Use of CCD Detectors in Astronomy", ESO Conf. Proc. No. 25
- Tomkin, J., Pan, X., McCarthy, J.K., 1995, AJ 109, 780
- Tull, R.G. 1972, in: ESO/CERN Conference on Auxiliary Instrumentation for Large Telescopes (eds. S.Laustsen & A.Reiz), p. 269
- Tull, R.G., MacQueen, P.J., Sneden, C., Lambert, D.L. 1995, PASP 107, 251
- Tuominen, I. 1992, NOT News, No. 5, p. 15
- Valenti, J.A., Butler, R.P., Marcy, G.W. 1995, PASP 107, 966
- Vogt, S.S., Penrod, G.D., Hatzes, A.P. 1987, ApJ 321, 496
- Wahlgren, M., Dolk, L., Kalus, G., Johansson, S. 1999, submitted to ApJ
- Watkins, D.S. 1991, Fundamentals of matrix computations (Wiley: New York)
- Wayte, R.C., Wynne-Jones, I., Blades, J.C. 1978, MNRAS 182, 5P
- Woolard, E.W., Clemence, G.M. 1966, Spherical Astronomy (Academic Press: New York)

Part II

Publications

Appendix B

Publications based on SOFIN observations

In this chapter a list of publications is given where the observing and reduction methods presented in the thesis were used.

The publications are divided into three groups, the first two (T Tau and RS CVn stars) contain results of the research project “Late type stars and interstellar matter: activity, magnetism, and turbulence” at the University of Oulu. The third group gives the papers of other works to which the author has contributed. Selected publications, marked with a bullet in the list, are presented in the subsequent part of this thesis.

The author’s contributions in most of the papers are observations and data reduction. This has given the possibility to develop the observing technique and data analysis, and to obtain a unique set of scientific observations. Frequent observations, analysis of various instrumental effects, the CCD optimization, development of the specific observing approach to the spectrograph resulted in high quality spectra as compared to the earliest observations with SOFIN or with other spectrographs we have used. The data reduction facility, as it is described in this thesis, was not created at once but was continuously developed during the past years with the raw material in hands. The most essential procedures which determine the quality of spectra reduction were recreated in some cases several times to achieve the maximum efficiency and stability. All this has resulted in excellent scientific output.

A demand to observe and analyze small effects of the line profile position and shape, which we see in the spectra of e.g. extra-solar planetary systems and stars which undergo non-radial pulsations, was a next step in the development of the data analysis facility including the error propagation in the data reduction, ad-

vanced cross-correlation, multi-period analysis, and the spectrum/PSF deconvolution facilities. The work is still going on and many new results are not included in the present thesis.

B.1 T Tau stars

Refereed journals:

- Petrov, P.P., Gullbring, E., Ilyin, I., Gahm, G.F., Tuominen, I., Hackman, T., Lodén, K. 1996, “The gas flows of SU Aurigae”, A&A 314, 821
- Gullbring, E., Petrov, P.P., Ilyin, I., Tuominen, I., Gahm, G.F., Lodén, K. 1996, “Line profile variations of the classical T Tauri star BP Tauri”, A&A 314, 835
- Zajtseva, G., Petrov, P.P., Ilyin, I., Duemmler, R., Tuominen, I. 1996, “RY Tauri at high brightness”, IBVS 4408
- Petrov, P., Duemmler, R., Ilyin, I., Tuominen, I. 1998, “Increase of emission and shell features in the spectrum of the FUor V1057 Cyg”, A&A 331, L53
 - Petrov, P.P., Zajtseva, G.V., Efimov, Yu.S., Duemmler, R., Ilyin, I.V., Tuominen, I., Shcherbakov, V.A. 1999, “Brightening of the T Tauri star RY Tauri in 1996. Photometry, polarimetry and high-resolution spectroscopy”, A&A 341, 553

Conference proceedings:

- Gahm, G.F., Petrov, P., Tuominen, I., Gullbring, E., Ilyin, I. 1995, “High-resolution spectroscopy of T Tauri stars”, 4th MUSICOS workshop (eds. L.Huang, D.S.Zhai, C.Catala, B.H.Foing), p. 237
- Petrov, P.P., Gullbring, E., Gahm, G.F., Lodén, K., Ilyin, I., Tuominen, I., Hackman, T. 1995, “Wind, accretion and spots of the T Tau star SU Aurigae”, Stellar surface structure (ed. K.Strassmeier), IAU Symp. 176, Poster Proceedings, p. 217
- Zajtseva, G., Efimov, Yu., Petrov, P., Ilyin, I., Duemmler, R., Tuominen, I. 1998, “Brightening of the T Tauri star RY Tau in 1996”, Cool Stars, Stellar Systems, and the Sun, 10th Cambridge Workshop, (eds. J.A.Bookbinder & R.A.Donahue), PASPC 154, p. 1808

B.2 RS CVn stars

Refereed journals:

- Duemmler, R., Ilyin, I., Tuominen, I. 1997, "A new radial velocity curve for the RS CVn star σ Gem. Constraints on its physical parameters.", A&AS 123, 209
- Berdyugina, S.V., Jankov, S., Ilyin, I., Tuominen, I., Fekel, F.C. 1998, "The active RS Canum Venaticorum binary II Pegasi. I. Stellar and orbital parameters", A&A 334, 863
- Berdyugina, S.V., Berdyugin, A.V., Ilyin, I., Tuominen, I. 1998, "The active RS Canum Venaticorum binary II Pegasi. II. Surface images for 1992-1996", A&A 340, 437
- Korhonen, H., Berdyugina, S.V., Hackman, T., Duemmler, R., Ilyin, I.V., Tuominen, I. 1999, "Study of FK Comae Berenices. I. Surface images for 1994 and 1995", A&A 346, 101
- Berdyugina, S.V., Ilyin, I., Tuominen, I. 1999, "The long-period RS Canum Venaticorum binary IM Pegasi. I. Orbital and stellar parameters", A&A 347, 932
- Berdyugina, S.V., Ilyin, I., Tuominen, I. 1999, "The active RS Canum Venaticorum binary II Pegasi. III. Chromospheric emission and flares in 1994-1996", A&A 349, 863
- Berdyugina, S.V., Berdyugin, A.V., Ilyin, I., Tuominen, I. 1999, "The active RS Canum Venaticorum binary II Pegasi. IV. The spot activity cycle", A&A 350, 626
- Berdyugina, S.V., Berdyugin, A.V., Ilyin, I., Tuominen, I. 2000, "The long-period RS Canum Venaticorum binary IM Pegasi. II. First surface images", accepted by A&A

Conference proceedings:

- Shcherbakov, A.G., Fernandez-Figueroa, M.J., Martin-Parra, F., De Castro, E., Cornide, M., Montes, D., Ilyin, I., Tuominen, I. 1995, "The He I 10830 Å and Ca II H observations of the RS CVn system ζ And", Stellar surface structure (ed. K.Strassmeier), IAU Symp. 176, Poster Proceedings, p. 181
- Berdyugina, S., Ilyin, I., Tuominen, I. 1998, "II Peg: Stellar and Orbital Parameters", Cool Stars, Stellar Systems, and the Sun, 10th Cambridge Workshop, (eds. J.A.Bookbinder & R.A.Donahue), PASPC 154, p. 1384

- Berdyugina, S., Ilyin, I., Tuominen, I. 1998, “II Peg: New Surface Images for 1992-1996”, *Cool Stars, Stellar Systems, and the Sun*, 10th Cambridge Workshop, (eds. J.A.Bookbinder & R.A.Donahue), PASPC 154, p. 1952
- Berdyugina, S., Ilyin, I., Tuominen, I. 1998, “II Peg: Quiescent Chromospheric Emission and Flares in 1994-1996”, *Cool Stars, Stellar Systems, and the Sun*, 10th Cambridge Workshop, (eds. J.A.Bookbinder & R.A.Donahue), PASPC 154, p. 1477
- Aarum, V., Berdyugina, S.V., Ilyin, I.V. 1999, “Doppler imaging of UX Ari”, *Proceedings of Astrophysics with the NOT* (eds. H.Karttunen & V.Pirola), University of Turku, p. 222
- Korhonen, H., Berdyugina, S.V., Duemmler, R., Hackman, T., Ilyin, I.V., Tuominen, I. 1999, “Surface imaging of FK Comae Berenices”, *Proceedings of Astrophysics with the NOT* (eds. H.Karttunen and V.Pirola), University of Turku, p. 234
- Berdyugina, S., Ilyin, I., Tuominen, I. 2000, “II Peg: the spot activity cycle”, *Cool Stars, Stellar Systems, and the Sun*, 11th Cambridge Workshop, (eds. M.R.Zapatero Osorio, R.García López & R.Rebolo), PASPC (in press)
- Berdyugina, S., Berdyugin, A.V., Ilyin, I., Tuominen, I. 2000, “IM Peg: first surface images”, *Cool Stars, Stellar Systems, and the Sun*, 11th Cambridge Workshop, (eds. M.R.Zapatero Osorio, R.García López & R.Rebolo), PASPC (in press)
- Berdyugina, S., Ilyin, I., Tuominen, I. 2000, “LQ Hya: surface images for 1993-1999”, *Cool Stars, Stellar Systems, and the Sun*, 11th Cambridge Workshop, (eds. M.R.Zapatero Osorio, R.García López & R.Rebolo), PASPC (in press)
- Piskunov, N., Vincent, A., Duemmler, R., Ilyin, I., Tuominen, I. 2000, “Doppler imaging of the eclipsing binaries ER Vul and TY Pyx”, *Cool Stars, Stellar Systems, and the Sun*, 11th Cambridge Workshop, (eds. M.R.Zapatero Osorio, R.García López & R.Rebolo), PASPC (in press)

B.3 Other stars and topics

Refereed journals:

- Polosukhina, N., Kurtz, D., Hack, M., North, P., Ilyin, I., Zverko, J., Shakhovskoy, D. 1999, “Lithium on the surface of cool magnetic CP stars I. Summary of spectroscopic observations with three telescopes”, *A&A* 351, 283
- Tautvaisiene, G., Tuominen, I., Ilyin, I. 1999, “M 67: an Exhibitor of Metal Abundant Core Helium-Burning Stars”, *Ap&SS* 265, 285

Tautvaišienė, G., Edvardsson, B., Tuominen, I., Ilyin, I. 2000, “Chemical composition of evolved stars in the open cluster M 67”, accepted by A&A

Conference proceedings:

Shcherbakov, A.G., Shcherbakova, Z.A., Ilyin, I., Tuominen, I. 1995, “Performance and astrophysical applications of EEV and Electron Corp. virtual phase CCDs in the near infrared He I 10830Å region”, New developments in array technology and applications (eds. D.Philip, K.A.Janes, A.R.Upgren), IAU Symp. 167

Schulz, R., Arpigny, C., Manfroid, J., Ilyin, I., Rickman, H., Stüwe, J.A. 1997, “On the $^{13}\text{CN}/^{12}\text{CN}$ isotopic ratio in comet Hale-Bopp”, Bull. AAS, 29th DPS meeting, No. 3, 37.09, p. 1048

- Ilyin, I.V., Duemmler, R. 1999, “Precise radial velocity measurements with a Cassegrain spectrograph. I. Wavelength calibration.”, in: Precise stellar radial velocities, IAU Coll. 170 (eds. J.B.Hearnshaw & C.D.Scarfe), PASPC 185, 63

- Ilyin, I.V., Duemmler, R. 1999, “Precise radial velocity measurements with a Cassegrain spectrograph. II. Radial velocity determination and applications”, in: Precise stellar radial velocities, IAU Coll. 170 (eds. J.B.Hearnshaw & C.D.Scarfe), PASPC 185, 68

Ilyin, I.V., Duemmler, R. 1999, “Precise radial velocities from the SOFIN Cassegrain échelle spectrograph”, Proceedings of Astrophysics with the NOT (eds. H.Karttunen & V.Piirola), University of Turku, 242

Tuominen, I., Ilyin, I.V., Petrov, P.P. 1999, “High resolution spectroscopy with SOFIN”, Proceedings of Astrophysics with the NOT (eds. H.Karttunen & V.Piirola), University of Turku, p. 47

Nielsen, K., Wahlgren, G.M., Ilyin, I.V. 1999, “Observations in the near-UV with the SOFIN”, Proceedings of Astrophysics with the NOT (eds. H.Karttunen & V.Piirola), University of Turku, p. 248

Wahlgren, G.M., Plez, B., Ilyin, I. 2000, “Abundance analysis of luminous M-type stars using near-UV spectroscopy”, Cool Stars, Stellar Systems, and the Sun, 11th Cambridge Workshop, (eds. M.R.Zapatero Osorio, R.García López & R.Rebolo), PASPC (in press)

Grinin, V.P., Kozlova, O., Rostopchina, A.N., Natta, A., Ilyin, I.V., Tuominen, I., Thé, P.S. 1999, “Spectral variability of the UX Ori type stars”, Proceedings of Astrophysics with the NOT (eds. H.Karttunen & V.Piirola), University of Turku, p. 226

Tautvaisiene, G., Tuominen, I., Ilyin, I. 1998, "M67: an Exhibitor of Metal Abundant He-Core Burning Stars", Proceedings of Galaxy Evolution: Connecting the Distant Universe with the Local Fossil Record, Paris-Meudon Observatory

Tautvaisiene, G., Tuominen, I., Ilyin, I.V. 1999, "Evolutionary effects in atmospheres of metal abundant red horizontal branch stars", Proceedings of Astrophysics with the NOT (eds. H.Karttunen & V.Pirola), University of Turku, p. 214

Paper I & II

Ilyin, I.V., Duemmler, R. 1999, "Precise radial velocity measurements with a Cassegrain spectrograph. I. Wavelength calibration", in: Precise Stellar Radial velocities, IAU Coll. 170 (eds. J.B.Hearnshaw & C.D.Scarfe), PASPC 185, p. 63

Ilyin, I.V., Duemmler, R. 1999, "Precise radial velocity measurements with a Cassegrain spectrograph. II. Radial velocity determination and applications", in: Precise Stellar Radial velocities, IAU Coll. 170 (eds. J.B.Hearnshaw & C.D.Scarfe), PASPC 185, p. 68

Paper III

Duemmler, R., Ilyin, I., Tuominen, I. 1997, "A new radial velocity curve for the RSCVn star σ Gem. Constraints on its physical parameters.", A&AS 123, 209

Paper IV

Petrov, P.P., Zajtseva, G.V., Efimov, Yu.S., Duemmler, R., Ilyin, I.V., Tuominen, I., Shcherbakov, V.A. 1999, "Brightening of the T Tauri star RY Tauri in 1996. Photometry, polarimetry and high-resolution spectroscopy", A&A 341, 553

Paper V

Petrov, P., Duemmler, R., Ilyin, I., Tuominen, I. 1998, "Increase of emission and shell features in the spectrum of the FUor V1057 Cyg", A&A 331, L53

Paper VI

Berdyugina, S.V., Jankov, S., Ilyin, I., Tuominen, I., Fekel, F.C. 1998, "The active RS Canum Venaticorum binary II Pegasi. I. Stellar and orbital parameters", A&A 334, 863

Paper VII

Berdyugina, S.V., Berdyugin, A.V., Ilyin, I., Tuominen, I. 1998, "The active RS Canum Venaticorum binary II Pegasi. II. Surface images for 1992-1996", A&A 340, 437

Paper VIII

Berdyugina, S. V., Ilyin, I., Tuominen, I. 1999, "The active RS Canum Venaticorum binary II Pegasi. III. Chromospheric emission and flares in 1994-1996", A&A 349, 863

Paper IX

Berdyugina, S. V., Berdyugin, A. V., Ilyin, I., Tuominen, I. 1999, "The active RS Canum Venaticorum binary II Pegasi. IV. The spot activity cycle", A&A 350, 626

Paper X

Berdyugina, S. V., Ilyin, I., Tuominen, I. 1999, "The long-period RS Canum Venaticorum binary IM Pegasi. I. Orbital and stellar parameters", A&A 347, 932

Paper XI

Berdyugina, S. V., Berdyugin, A. V., Ilyin, I., Tuominen, I. 2000, "The long-period RS Canum Venaticorum binary IM Pegasi. II. First surface images", accepted by A&A